Strategies and Methods for Investigating Performance and Degradation in Solid-State Batteries Using Thiophosphate Solid Electrolytes

Dem Fachbereich Biologie und Chemie
der Justus-Liebig-Universität Gießen
vorgelegte Dissertation zur Erlangung
des akademischen Grades
Doktor der Naturwissenschaften
— Dr. rer. nat. —

Jonas Hertle

November 2024

Dekan/Dean	Prof. Dr. Holger Zorn
1. Gutachter / 1st Reviewer	Prof. Dr. Dr. h.c. Jürgen Janek
2. Gutachter / 2nd Reviewer	Prof. Dr. Anja Henß

Eigenständigkeitserklärung / Declaration of Originality

Die vorliegende Arbeit wurde im Zeitraum vom 01.07.2018 bis 31.12.2023 am Physikalisch-Chemischen Institut der Justus-Liebig Universität Gießen unter Betreuung von Prof. Dr. Dr. h. c. Jürgen Janek angefertigt.
Ich erkläre:
Ich habe die vorgelegte Dissertation selbstständig und ohne unerlaubte fremde Hilfe und nur mit den Hilfen angefertigt, die ich in der Dissertation angegeben habe. Alle Textstellen, die wörtlich oder sinngemäß aus veröffentlichten Schriften entnommen sind, und alle Angaben, die auf mündlichen Auskünften beruhen, sind als solche kenntlich gemacht. Ich stimme einer evtl. Überprüfung meiner Dissertation durch eine Antiplagiat-Software zu. Bei den von mir durchgeführten und in der Dissertation erwähnten Untersuchungen habe ich die Grundsätze guter wissenschaftlicher Praxis, wie sie in der „Satzung der Justus-Liebig-Universität Gießen zur Sicherung guter wissenschaftlicher Praxis“ niedergelegt sind, eingehalten.

This thesis was prepared in the period from 01.07.2018 to 31.12.2023 at the Physical-Chemical Institute of the Justus Liebig University Giessen under the supervision of Prof. Dr. Dr. h. c. Jürgen Janek.
I declare that I have completed this dissertation single-handedly without the unauthorized help of a second party and only with the assistance acknowledged therein. I have appropriately acknowledged and cited all text passages that are derived verbatim from or are based on the content of published work of others, and all information relating to verbal communications. I consent to the use of an anti-plagiarism software to check mythesis. I have abided by the principles of good scientific conduct laid down in the charter of the Justus Liebig University Giessen „Satzung der Justus-Liebig-Universität Gießen zur Sicherung guter wissenschaftlicher Praxis“ in carrying out the investigations described in the dissertation.

Gießen, 05.12.2024

Jonas Hertle

Abstract

The demand for high-performance energy storage solutions is ever-growing, driven by the increasing need for portable electronics and electric vehicles. While conventional lithium-ion batteries (LIBs) are well established, they are approaching their limits in terms of energy and power density. Solid-state batteries (SSBs) offer a promising alternative with the potential for significantly higher energy densities when using lithium metal anodes. However, a major challenge remains in the reactivity of thiophosphate solid electrolytes (SEs) with cathode active materials (CAMs), leading to degradation and performance limitations.

Current approaches used for the analysis of SSBs are limited. The influence of the anode in electrochemical experiments, specifically the overpotential, leads to unreliable results because these overpotentials are usually unknown and not accounted for. Degradation analysis in combination with standard cell setups using widely utilized post mortem techniques like X-ray photoelectron spectroscopy (XPS) and time-of-flight secondary ion mass spectrometry (ToF-SIMS) lack sensitivity and show overlap of different degradation pathways.

To address these shortcomings, this thesis introduces two key contributions in the form of two publications:

Publication I introduces a three-electrode (3E) setup for SSBs. A thin gold-plated tungsten wire is lithiated in-situ to provide a stable potential. This enables the independent measurement of cathode and anode, providing accurate information on the true rate-performance of CAMs without limitations from anode overpotential. Furthermore, single-electrode impedance analysis is rendered possible. This facilitates impedance analysis of the electrodes and removes ambiguity when fitting impedance data to equivalent circuits.

Publication II introduces a reliable benchmarking method for CAM coatings. This method combines the 3E setup from publication I with ToF-SIMS analysis. A specially developed current collector is used. With the help of this current collector and ToF-SIMS analysis, a semi-quantitative analysis of the various degradation pathways is made possible. Principal component analysis (PCA) is used to cope with the large data volumes of the ToF-SIMS analysis. This approach allows the complete evaluation of CAMs regarding their electrochemical performance as well as their susceptibility to degradation.

By extending the knowledge of electrochemical and post mortem analysis in SSBs, this thesis paves the way for accelerated research and development. The presented concepts are transferable to other battery systems, offering broader research possibilities. Ultimately, this work contributes to the development of competitive and commercially viable SSBs.

Zusammenfassung

Durch den wachsenden Bedarf an Batterien in Elektrofahrzeugen und mobiler Elektronik steigt die Nachfrage nach leistungsstarken Energiespeichern stetig an. Herkömmliche Lithium-Ionen-Batterien (LIBs) stoßen jedoch hinsichtlich Energie- und Leistungsdichte an ihre Grenzen. Festkörperbatterien (Solid-state batteries, SSB) bieten eine vielversprechende Alternative mit dem Potenzial zu deutlich höheren Energiedichten, wenn Lithiummetall-Anoden verwendet werden.

Die Degradation von Thiophosphat-Festelektrolyten (SE) und Kathodenaktivmaterialien (CAM), führt jedoch zu Leistungseinschränkungen und bleibt eine bisher ungelöste Herausforderung. Die derzeit verwendeten Ansätze zur Analyse von SSB sind unzureichend. So verzerrt der Einfluss der Anode in elektrochemischen Experimenten die Ergebnisse aufgrund von Überspannungen an der Anode. Desweiteren ist die Analyse der Degradation mittels Röntgenphotoelektronenspektroskopie (XPS) zu unempfindlich, um geringe Konzentrationen von Degradationsprodukten nachzuweisen. Die Flugzeit-Sekundärionen-Massenspektrometrie (ToF-SIMS) und Standardzellaufbauten können nicht zwischen verschiedenen Degradationswegen unterscheiden. Um diese Unzulänglichkeiten zu beheben, werden in dieser Arbeit zwei Beiträge in Form zweier Publikationen vorgestellt.

In Publikation I wird ein Drei-Elektroden-Aufbau (3E) für SSBs vorgestellt. Ein dünner goldbeschichteter Wolframdraht wird in situ lithiiert, um ein stabiles Referenzpotential zu erhalten. Dies ermöglicht die unabhängige Messung von Kathode und Anode und liefert genaue Informationen über die tatsächliche Ratenleistung von CAMs ohne Einschränkungen durch die Anodenüberspannung. Darüber hinaus wird die Impedanzanalyse an einer einzelnen Elektrode ermöglicht. Dies erleichtert die Impedanzanalyse der Elektroden und beseitigt Mehrdeutigkeiten beim Fitten von Impedanzdaten an Ersatzschaltbildern.

In Publikation II wird eine zuverlässige Benchmarking-Methode für CAM-Beschichtungen vorgestellt. Diese Methode kombiniert den 3E-Aufbau aus Publikation I mit ToF-SIMS Analyse. Hierbei wird ein eigens entwickelter Stromableiter verwendet. Mithilfe dieses Stromableiters und der ToF-SIMS Analyse wird eine semi-quantitative Analyse der verschiedenen Degradationspfade ermöglicht. Um die großen Datenmengen der ToF-SIMS Analyse zu bewältigen, wird auf Hauptkomponentenanalyse (PCA) zurückgegriffen. Dieser Ansatz erlaubt die vollständige Evaluierung von CAMs bezüglich ihrer elektrochemischen Leistungsfähigkeit sowie ihrer Anfälligkeit gegenüber Degradation.

Diese Arbeit ebnet durch fortgeschrittene elekrochemische und post mortem Analysen für SSB den Weg für eine beschleunigte Forschung und Entwicklung. Die vorgestellten Konzepte sind auf andere Batteriesysteme übertragbar und bieten somit breitere Forschungsmöglichkeiten. Letztendlich, trägt diese Arbeit zur Entwicklung wettbewerbsfähiger und kommerziell nutzbarer SSBs bei.

Abbrevations and Symbols

Abbrevation	Full form
2E	2-electrode
3E	3-electrode
ALD	Atomic layer deposition
ASSB	All solid-state lithium ion battery
BSE	Back-scattered electrons
CAM	Cathode active material
CEI	Cathode electrolyte interphase
CVD	Chemical vapour deposition
DSC	Differential scanning calorimetry
E	(Electrochemical) potential
EV	Electric vehicle
FIB	Focused ion beam
i	current density $\left[\mathrm{A\,cm^{-2}}\right]$
IEA	International Energy Agency
j	imaginary unit, $j^2 = -1$
$\mathrm{K_L}$	Solubility constant
K-SSB	Potassium solid-state battery
LE	Liquid Electrolyte
LGPS	$\mathrm{Li_{10}GeP_2S_{12}}$
LNO	lithium nickel oxide, $\mathrm{LiNiO_2}$
LTO	$\mathrm{Li_4Ti_5O_{12}/Li_7Ti_5O_{12}}$
M	Metal
MVD	Molecular vapor deposition
Na-SSB	Sodium solid-state battery
NCM111	$\mathrm{LiNi_{0.33}Co_{0.33}Mn_{0.33}O_2}$
NCM523	$\mathrm{LiNi_{0.5}Co_{0.2}Mn_{0.3}O_2}$
NCM622	$\mathrm{LiNi_{0.6}Co_{0.2}Mn_{0.2}O_2}$
NCM701515	$\mathrm{LiNi_{0.70}Co_{0.15}Mn_{0.15}O_2}$
NCM811	$\mathrm{LiNi_{0.8}Co_{0.1}Mn_{0.1}O_2}$
NCM821206	$\mathrm{LiNi_{0.82}Co_{0.12}Mn_{0.06}O_2}$
NCM851005	$\mathrm{LiNi_{0.85}Co_{0.10}Mn_{0.05}O_2}$
OCP	Open circuit potential
OCV	Open circuit voltage
PAN	Polyacrylonitrile
PCA	Principal component analysis
PEDOT	Poly(3,4-ethylenedioxythiophene)

Abbrevation	Full form
PLD	Pulsed laser deposition
PVBTA-TFSI	Poly((4-vinyl benzyl)trimethylammonium bis(trifluoromethanesulfonylimide))
PVBTA-TFSI	Poly((4-vinyl benzyl)trimethylammonium bis(trifluoromethanesulfonylimide))
SE	Solid electrolyte
SEI	Solid electrolyte interphase
SEM	Scanning electron microscopy
SHE	Standard hydrogen electrode
SLI	Starter, light, ignition
SOC	State-of-charge
t_i	Transference number of species i
ToF-SIMS	Time-of-flight secondary ion mass spectrometry
U	Voltage
XPS	X-ray photoelectron spectroscopy
XRD	X-ray diffraction
y	year
ν	frequency, $\omega = 2\pi\nu$
ω	angular frequency $[s^{-1}]$

Preliminary remarks

The negative electrode is the anode during discharge and the positive electrode is the cathode during discharge as an oxidation is happening on the anode and a reduction is happening at the cathode. During charge this is reversed, i. e. the negative electrode is then the cathode and the positive electrode is then the anode. However, in literature the terms anode for the negative electrode and cathode for the positive electrode are widely used. In order to avoid confusion, in this thesis this standard is used as well despite being unprecise.

Contents

1 Introduction

Lithium-ion batteries (LIBs) are the most popular type of rechargeable battery used today, powering a wide range of devices from smartphones and laptops to electric vehicles (EVs). Since their introduction in 1991 by Sony, they have become the most important battery technology both in market size and produced capacity.[1–6] Their widespread use stems from their high energy density, long lifespan, and low self-discharge rate.[7–9]

The global demand for LIBs is projected to increase heavily in the coming years. According to a report by the government of the USA, the total lithium-ion battery capacity produced in 2022 was approximately 1.57 TW h, which is expected to reach 3.97 TW h in 2025 and 6.79 TW h in 2030 as shown in fig. 1.[7,10]

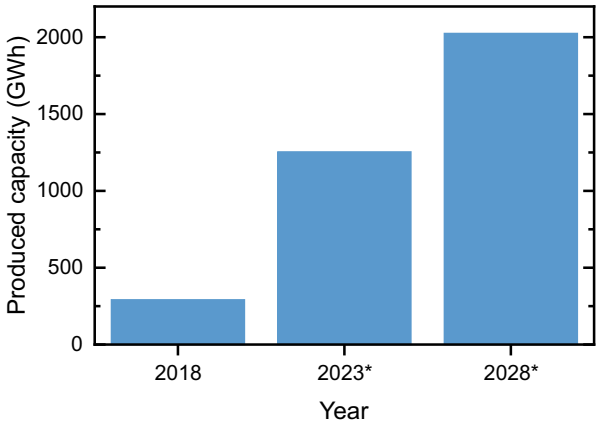

Figure 1: Produced capacity of LIBs worldwide. In comparison, the annual produced capacity lead-acid batteries is about 350 GW h. Years marked with an asterisk are estimates.

The increasing use of LIBs in EVs is particularly driving the demand for high-energy density cells and batteries. EVs require batteries with a high energy density to power their motors and provide sufficient range for daily driving. Research and development efforts are focused on developing new materials and technologies to enhance the energy density and performance of LIBs, paving the way for more efficient and sustainable transportation solutions. Their high energy and power density in combination with good cycle life makes them the technology of choice for a large number of applications including portable consumer electronics and electric vehicles (EV).[11,12] These advantages made LIB the most produced battery type in the world with the production increasing strongly.[3,13] Under these circumstances it comes as no surprise that the Nobel prize for chemistry in 2019 was awarded to Goodenough, Whittingham and Yoshino for developing this technology.[14–17]

The operation of LIBs involves the reversible intercalation of Li^+-ions between the anode and cathode during charging and discharging. During charging, Li^+-ions migrate from the cathode to the anode, while electrons flow through an external circuit to power the device. Conversely, during discharging, Li^+ ions migrate from the anode back to the cathode, and

electrons flow from the external circuit to recharge the battery. In conventional LIBs the two electrodes are separated by a porous membrane soaked in liquid electrolyte (LE).

However, despite continuous improvements the limit in energy density is approaching and no major breakthroughs are expected using existing technologies.[18] Therefore, new technologies need to be developed to satisfy the demand for even higher energy and power densities. Theoretically, the energy density of LIBs can be improved by using new anode materials such as silicon or lithium metal. Both materials have high specific capacities of $4200\,\mathrm{mA\,h\,g^{-1}}$ and $3861\,\mathrm{mA\,h\,g^{-1}}$ and low potentials of $-2.6\,\mathrm{V}$ and $-3.04\,\mathrm{V}$ vs. standard hydrogen electrode (SHE), respectively.[19–22] These materials are, however, challenging to use in LIBs. Silicon suffers from large volume expansion during lithiation which leads to cracking of the electrode.[23–25] Lithium metal tends to form dendrites, small tree-like branches of lithium metal, that can penetrate the separator leading to unwanted side reactions and ultimately short circuits of the cell.[26,27]

Solid-state batteries (SSBs) are investigated as an alternative concept with potentially higher energy and power densities compared to LIBs. SSBs offer a new approach with solid electrolytes replacing the liquid electrolyte in traditional batteries. This change might bring a safety benefit due to the usually low flammability of solid electrolytes. Furthermore, careful manufacturing can allow high current densities without the formation of dendrites.

Thiophosphate, or sulfide electrolytes are among the most promising candidates for SSBs. They have very high ionic conductivites of up to $32\,\mathrm{mS\,cm^{-1}}$ exceeding even the conductivites of state of the art liquid electrolytes.[28] However, several challenges remain. Dendrite formation is still an issue despite the solid electrolyte acting as a barrier. Additionally, solid electrolytes themselves can decompose over time leading to worse performance over time. Thiophosphate, or sulfide electrolytes are prone to reduction at low electrochemical potentials present at the anode and suffer from oxidation at high electrochemical potentials found at the cathode. Because of that, protective coatings are investigated to prevent degradation at the CAM | SE interface.[29]

Despite significant efforts to identify suitable coatings for thiophosphate-based solid-state batteries (SSBs) and the fundamental degradation mechanism – which have already been investigated –the field is lacking in systematic studies. These studies often fail to differentiate between different degradation mechanisms, making it challenging to draw meaningful conclusions. Furthermore, the studies often present only one coating, and comparisons of different coatings are not found in the literature. This is, in part, due to the lack of sensitivity of the applied analytical techniques. Furthermore, the electrochemical analysis of CAMs for SSBs is hindered by the detrimental influence of the anode. 3E setups, which are well established for liquid electrolytes, prevent this, but they have not been utilised in SSBs.

This thesis closes these shortcomings in the form of two publications. The first publication introduces a 3E setup for SSB with minimal impact on the cells geometry, enabling independent measurement of cathode and anode. Rate-tests without overpotentials from the anode can be carried out allowing precise measurement of the rate performance of a CAM. Furthermore, single-electrode impedance measurements can be carried out facilitating the analysis of impedance data significantly.

The second publication introduces a benchmarking approach for coatings on CAMs for SSBs. Analytical techniques are compared and ToF-SIMS is found to be best analytical technique to investigate degradation of the SE | CAM interface. A statistical approach is used to assign the correct weight to each analysed signal. To investigate the electrochemical performance the 3E setup previously developed and published is used.

2 State-of-Knowledge

While LIBs are a well-established technology, research into SSBs is still ongoing. Before they can be commercialised, several problems still have to be solved. The following sections aim to provide a brief overview of the materials used in SSBs, in order to help readers to better understand the challenges that need to be overcome in order to enable the widespread application of SSBs.

While LIBs offer the highest energy and power density of any battery type at a low price, the need for even higher energy densities initiates further research into new technologies meeting these demands. SSBs can potentially offer higher energy densities by enabling the use of Li-metal anodes.

2.1 Lithium-ion batteries

LIBs are a widespread battery technology and are the almost exclusive technology used for portable electronics and EVs. Despite ongoing efforts to increase the energy density of these cells, the limit is approaching for this technology.[30] While the theoretical value for energy density is only limited by the active material in use and values as high as $860\,\mathrm{Wh\,kg^{-1}}$, these values are limited in practice by the inclusion of electrolyte, separator, anode and casing.[31–33]

LIBs work by moving lithium ions from the anode (i. e. the negative electrode) to the cathode (i. e. the positive electrode) during discharge and vice versa. The lithium ions are then (de)intercalated into graphite on the anode and (de)intercalated into a lithium metal oxide on the cathode according to equations (1a) and (1b). The two electrodes are separated by an organic electrolyte such as ethylene carbonate or diethyl carbonate with a dissolved lithium salt, usually $LiPF_6$. This mechanism, which involves the transport of lithium ions from one electrode to the other, has given rise to the term 'rocking chair' Li-ion batteries.

$$\mathrm{LiC_6} \leftrightharpoons \mathrm{Li^+ + e^- + C_6} \tag{1a}$$

$$\mathrm{Li_{1-x}MO_2} + x\mathrm{e^-} + x\mathrm{Li^+} \leftrightharpoons \mathrm{Li_1MO_2} \tag{1b}$$

Graphite is used an electrode material because of it's low potential of $\sim 100\,\mathrm{mV}$ vs. Li^+/Li and acceptable capacity of $372\,\mathrm{mA\,h\,g^{-1}}$.[34] Historically, $LiCoO_2$ was used as cathode material.[14,35] However, substituting manganese and nickel for cobalt yields isostructural materials with higher reversible capacities and thus allowing higher energy densities.[36–38]

The anode exhibits a relatively high chemical potential of lithium $\mu_{\mathrm{Li}}(\mathrm{A})$ while the cathode

exhibits a relatively low chemical potential of lithium $\mu_{\mathrm{Li}}(\mathrm{C})$. This results in a voltage between the two electrodes. Because the cell is ionically short-circuited the electrochemical potential of lithium-ions $\mu_{\mathrm{Li^+}}$ is constant throughout the cell and the difference in chemical potential of lithium is entirely defined by the electrochemical potential of the electrons.

$$\mu_{\mathrm{Li}} = \tilde{\mu}_{\mathrm{Li^+}} + \tilde{\mu}_{\mathrm{e^-}} \tag{2a}$$

$$\Delta\mu_{\mathrm{Li}} = \mu_{\mathrm{Li}}(\mathrm{C}) - \mu_{\mathrm{Li}}(\mathrm{A}) \tag{2b}$$

$$\Delta\mu_{\mathrm{Li}} = \{\tilde{\mu}_{\mathrm{Li^+}}(\mathrm{C}) + \tilde{\mu}_{\mathrm{e^-}}(\mathrm{C})\} - \{\tilde{\mu}_{\mathrm{Li^+}}(\mathrm{A}) + \tilde{\mu}_{\mathrm{e^-}}(\mathrm{A})\} \qquad \text{where } \tilde{\mu}_{\mathrm{Li^+}} = \text{const.} \tag{2c}$$

$$\Delta\mu_{\mathrm{Li}} = \tilde{\mu}_{\mathrm{e^-}}(\mathrm{C}) - \tilde{\mu}_{\mathrm{e^-}}(\mathrm{A}) \tag{2d}$$

$$\Delta\mu_{\mathrm{Li}} = \Delta\tilde{\mu}_{\mathrm{e^-}} \tag{2e}$$

$$\Delta\tilde{\mu}_{\mathrm{e^-}} = \mathrm{UF} \tag{2f}$$

2.2 Solid-state batteries

In contrast to classical LIBs SSBs replace the LE with a solid electrolyte. SEs are, apart from polymer SEs, single ion conductors with a transference number $t_{\mathrm{Li^+}} \approx 1$, therefore no concentration gradient is build up during cycling in the electrolyte. One major potential advantage of SE over LEs is their low flammability and hence increased safety of the cell.[39–42] This aspect is to this day still largely unproven and their is currently no study explicity showing the low flammbility of SEs, especially thiophosphate SEs. Contrarily, more recent studies show highly exothermic reactions between NCM type CAMs and thiophosphate SEs.[43–46] Another recent study claims that SSB using Li-metal anodes and LLZO as SEs are getting significantly hotter when short-circuited compared to LIBs. This is due to the higher energy density of the cell with the Li-metal anode. This study suggests, that the increased safety of the SE is negated by the higher energy density of the resulting cell.[47] Generally, there are no conclusive results to back up the claims of better flammability properties of SSB.[48] The safety aspect in terms of the release of toxic gases such as HF in case of LIBs and H_2S in case of SSB remains unclear as well until dedicated studies are published.[45]

2.2.1 Anode materials

Choosing an anode material for SSB is highly dependent on the focus of the research and the performance that the cell should deliver. For academic research with focus on the cathode side, such as in this thesis, an anode is only needed to run and cycle the cell. Other than that, a perfect anode does not interfere with electrochemical measurements of the cathode. This is however not possible and realistically the anode should exhibit the following properties.

Firstly, the anode should be stable against the SE separator to avoid degradation. This is important, to ensure a constant performance of the anode. If the anode material is not stable against the SE, it should at least form a stable SEI. Secondly, the impedance should be low so that no large overpotential is introduced. This is especially important when using high currents. Lastly, the electrochemical potential should be constant, i. e. independent from SOC of the cell. This makes interpretation of the potential and SOC of the cathode much easier.

In the following the most important anode materials are introduced showing their respective advantages and disadvantages as well as their commercial viability.

Lithium metal has the lowest potential of $-3.04\,\mathrm{V}$ vs. SHE. Combined with the high specific capacity of $3861\,\mathrm{mA\,h\,g^{-1}}$ it enables the highest energy density of all known anode materials making it desirable for use in full cells.[49,50] However, the kinetic properties of lithium metal, namely dendrite formation during plating, have prevented widespread commercial use so far.[51–53] Dendrites are small tree-like structures that can grow on lithium metal electrodes due to heterogeneous lithium deposition. These dendrites can penetrate the whole separator and consequently lead to internal short-circuiting of the cell. These dendrites can even form through SEs and lithium metal electrodes have to be carefully engineered to hinder dendrite formation.[54–56]

Lithium Titanate or more precisely $Li_4Ti_5O_{12}/Li_7Ti_5O_{12}$ (LTO) is a well-established anode material for high-power LIBs. Besides the practical use of LTO, it is also an interesting electrode material for academic research. LTO exhibits a stable potential of $1.55\,\mathrm{V}$ vs. Li^+/Li as long as both phases $Li_4Ti_5O_{12}$ and $Li_7Ti_5O_{12}$ are present in the electrode.[57] This property is often considered particularly useful when investigating cathode materials as the SOC of the CAM can be easily determined without the need of a reference electrode.

However, in SSB this assumption does not hold true at the end of delithation of the LTO electrode as shown in Publication I leading to potentially large errors in the determination of SOC.[58] Furthermore, the high-power properties of LTO in LIBs do not translate to SSBs and large overpotentials are introduced in LTO SSB.[58,59] This is mainly due to the fact, that LTO electrodes in SSB need electronically conductive additives like carbon to function which is lowering the volume ratio of LTO and SE leading to tortuous conduction pathways. This ultimately increases the impedance and decreases the rate capability of the electrode.[60] However, the high potential of LTO leads to little or no degradation in contact with thiophosphate SEs and thus enables stable cycling.

Another big advantage is the very low volume difference between $Li_4Ti_5O_{12}$ and $Li_7Ti_5O_{12}$

of $\sim 0.14\,\%$ which is close to the experimental error of the respective XRD experiments.[57,61] This allows precise pressure monitoring of CAMs while other anode materials would disturb these pressure measurements.[62–66]

Indium/Indium-Lithium is almost exclusively used in academic research due to the high cost, low availability of indium and the high potential of 0.62 V vs. Li^+/Li lowering the energy density of the full cells. For academic research these disadvantages are not an issue. In/InLi is a two-phase material with a stable voltage plateau enabling easy determination of the SOC of the cathode.[67] Furthermore, In/InLi is easy to manufacture by simply stacking In and Li in an appropriate stochiometric ratio on top of an electrolyte. In addition, the high potential of In/InLi reduces detrimental reactions of the electrode with the separator electrolyte. Also, dendrite formation is not an issue even at very high currents enabling high-current long-term cycling. However, high-current operation of In/InLi electrodes requires careful tuning of the electrode as otherwise a high overpotential can be encountered.[68] Because of these properties In/InLi can be used for long-term cycling, although there are studies encountering stability issues after more than 1 000 cycles.[69]

2.2.2 Solid Electrolytes

The appropriate choice of SEs is essential for the function of SSBs. Ideally, they need to fulfill the following properties. They need to be stable against reduction at the anode and stable against oxidation on the cathode. Or, if they are unstable, they need to form a passivation layer that prevents continuous degradation. Their ionic conductivity needs to be high enough in order to enable practical current densities.[70] Furthermore, they need to be processable on a large scale. To date, no SE fulfilling all these requirements has been reported. However, several promising candidates have been published.

Usually, SEs are divided into four classes. Of those, oxide, thiophosphate and halide electrolytes are all single-ion conductors, i. e. they exhibit an ionic transference number $t_{Li^+} \approx 1$.

Thiophosphate Solid Electrolytes or sulfide SEs have first been described in the 1980s by Mercier and Tachez in the form of the glasses Li_2S-P_2S_5-LiI and Li_3PS_4.[71–73] Despite this early discovery they have only been used in Li-SSB in 2002 by Murayama et al.,[74] and gained significantly more attention after the discovery of the highly conductive Li_6PS_5Cl argyrodite and $Li_{10}GeP_2S_{12}$ LGPS-type phases.[75,76]

These SEs are among the most promising candidates for electrolytes in SSB due to their high Li-ion conductivities of up to $32\,mS\,cm^{-1}$,[28,76] and their good mechanical properties

allowing for good contact between thioposphate SEs and CAMs by simple cold pressing.[77] These properties allow potentially easy large-scale manufacturing.

However, the small electrochemical stability window of approximately $\sim$1.7–2.5 V vs. Li^+/Li,[78] leads to reduction on the anode side and oxidation of the SE on the cathode side as also described in section 2.3 on page 12.[43,44,79–86]

Oxide Solid Electrolytes Oxide SEs show excellent stability against the active materials used in lithium batteries.[78] $Li_{6.25}Al_{0.25}La_3Zr_2O_{12}$ for example is stable against lithium metal and therefore well suited for use as an anolyte.[55,56,87–89] LAGP on the other hand has an oxidation stability of > 4.5 V vs. Li^+/Li making it suitable as catholyte.[90]

However, their conductivity is lower compared to sulfide SEs reaching up to only about $1\,mS\,cm^{-1}$.[91] Futhermore, to establish good contact between active materials and oxide SEs sintering at high temperatures is usually needed, making large scale production difficult.

Polymer Solid Electrolytes Polymer SEs show excellent mechanical properties.[92,93] Their low melting point allows potentially easy manufacturing on large scales. However, in contrast to the other classes of SEs the transference number of Li ions t_{Li^+} is not close to unity, but rather quite low around $t_{Li^+} \approx 0.2$.[92,94] This can lead to concentration gradients during cycling similar to liquid electrolytes. In addition, their ionic conductivity is low at room temperature, requiring elevated temperatures for cycling.[92] They are also prone to oxidation above 3.6 V vs. Li^+/Li due to oxidation of the polymer backbone and reduction in contact with the Li metal anode.[95,96]

Despite these drawbacks, polymer SEs offer potential due to their increased safety and temperature tolerance.[94]

Halide Solid Electrolytes Halide SEs were only quite recently re-discovered. While first reports of Li_3InCl_6 date back to 1992, the ionic conductivity was too low to be practical.[97] Only after higher conductivities of up to $1.1\,mS\,cm^{-1}$ for $Li_3Er_{0.9}Zr_{0.1}Cl_6$ were achieved this class of materials attracted more attention.[98–100]

Halide SE show excellent oxidation stability making them suitable candidates for use in SSB cathodes.[100–102] They are, however, highly unstable vs. Li-metal and potentially other anode materials, as well.[80] Due to their lower conductivity compared to thiophosphate SEs and use of expensive resources such as indium, erbium or yttrium their use is probably limited to small scale applications or use as interlayers and coatings.

2.2.3 Cathode Active Materials

CAMs for LIBs and SSBs can be separated in two classes. Firstly, layered oxide of the general formula $Li_{1-x}Ni_{1-k-l}Co_kMn_lO_2$, where $k+l \leq 1$ (NCM) or $Li_{1-x}Ni_{1-k-l}Co_kAl_lO_2$, where $k+l \leq 1$ (NCA). These materials crystallize in the same space group $R\bar{3}m$ (D^5_{3d}).[103] Due to the broad substitution range of these materials, hundreds of different materials have been investigated. Depending on the specific material delithiation of up to $x = 0.8$ can be reached (see eq. 3a)

Secondly, $LiFePO_4$ (LFP), a two phase material, which serves mainly as a low cost alternative to layered oxides due to the lower capacity of $170\,mA\,h\,g^{-1}$ and operating voltage of 3.5 V vs. Li^+/Li in LIBs.[104,105] In contrast to layered oxides the delithiation is is a heterogeneous two-phase reaction (eq. 3b). Research with LFP in SSB is however still limited. Current studies suggest, that the particle size of the LFP active material and the SE has to be finely tuned.[106] Other studies show incompatiblity of LFP with thiophosphate SEs.[43]

$$Li_1Ni_{1-k-l}Co_kMn_lO_2 \leftrightharpoons xLi^+ + xe^- + Li_{1-x}Ni_{1-k-l}Co_kMn_lO_2 \tag{3a}$$

$$LiFePO_4 \leftrightharpoons Li^+ + e^- + FePO_4 \tag{3b}$$

2.2.4 Electronic structure of LCO and LNO

Both the electronic structures of LCO and LNO have been studied extensively, both theoretically and experimentally.[107–112] $LiCoO_2$ is a wide gap semiconductor (band gap between 2.1 eV[113] and 2.7 eV[108]). The electronic conductivity is therefore comparably low and conductive additives are needed to ensure working electrodes. $LiNiO_2$ is a small band gap semiconductor with a band gap of around 0.4 eV.[114] The electronic conductivity is therefore considerably higher than that of $LiCoO_2$.

$LiCoO_2$ and $LiNiO_2$ share a rhombohedral crystal structure $R\bar{3}m$ (D_{3d^5}), with each unit cell containing three formula units.[115,116] Despite this structural similarity, these cathode materials exhibit distinct electronic properties and band structures due to varying electronic configurations of the transition metals. In $LiCoO_2$, cobalt adopts a $3d^6$ $(t_{2g})^6$ configuration with minimal hybridization with other orbitals. This electronic structure aligns well with a Co^{III} oxidation state assignment. Conversely, nickel in $LiNiO_2$ possesses a low-spin $d^7(t_{2g})^6\,(e_g)^1$ configuration. This electronic arrangement exhibits significant hybridization, suggesting a more complex electronic structure compared to $LiCoO_2$. Consequently, assigning a formal oxidation state of Ni^{III} to Ni in $LiNiO_2$ is not fully representative of its true electronic character.[107]

2.2.5 Thermal and Structural Stability of Layered Oxides

In order to achieve higher energy densities in LIBs the main strategy is to increase the Ni content in the layered oxide CAMs. Although the theoretical capacity of layered oxides only varies slightly between $274\,\mathrm{mAh\,g^{-1}}$ and $278\,\mathrm{mAh\,g^{-1}}$, LCO has a reversible capacity of $\sim 140\,\mathrm{mA\,h\,g^{-1}_{CAM}}$, NCM622 has already a reversible capacity of $\sim 180\,\mathrm{mA\,h\,g^{-1}_{CAM}}$ and LNO shows reversible capacities of up to $\sim 230\,\mathrm{mA\,h\,g^{-1}_{CAM}}$.[117] However, the capacity retention of CAMs with higher nickel content also decreases.[117,118]

Additionally, the thermal stability of these materials decreases with increasing Ni content as well. This can be seen in DSC measurements where a mixture of liquid electrolyte and CAM is heated up. CAMs with higher Ni content consistently show lower onsets of exothermic reactions with LNO showing the lowest onset.[43,118,119] Because of this, high Ni and LNO CAMs are often seen as an inferior option due to lower cycle life and higher risk of thermal runaway.

However, these studies are usually carried out using the same upper cut-off potential. Because of the higher reversible capacities for high-Ni CAMs the degree of delithiation x in $\mathrm{Li_{1-x}MO_2}$ is much higher compared to low-Ni CAMs. For example, the degree of delithiation at 4.3 V vs. $\mathrm{Li^+/Li}$ is $x = 0.51$ for LCO and $x = 0.84$ for LNO.

A better comparison for the stability of these materials would therefore be a comparison at the same degree of delithiation or even better, at the same energy density of the electrode. To date, only the former has been published.[36] When charged to the same degree of delithiation NCM811 exhibits a steeper raise in cutoff potential compared to LNO combined with a slower rise of overpotential on the cathode.[36] These results suggest, that LNO is more stable than NCM811 during cycling when the cutoff parameter is the degree of delithiation (and therefore, approximately also the energy density of the cell). This is true, despite the fact, that LNO shows more structural degradation in the form of particle cracking.

Unfortunately, similar studies using SEs are lacking and it is not clear how these results transform to SSB. While it can be expected that the cycling stability is behaving similarly, the cracking would likely have a detrimental effect on the electrochemical performance in SSB.[120]

2.2.6 Composite Cathodes

Layered oxide CAMs are intercalation type materials, i. e. $\mathrm{Li^+}$ and $\mathrm{e^-}$ have to diffuse both through the material during charge and discharge. Because the ionic conductivity and electronic conductivity of NCM materials is too low for reasonable current densities cathodes for SSBs are manufactured as composites with CAM, SE and often carbon as

electronically conductive additive.[121] Especially the Li^+-ion conductivity is low, in the range of $\sim 10^{-8}\,S\,cm^{-1}$ to $\sim 10^{-9}\,S\,cm^{-1}$ for NCM523 and NCM111.[121] The electronic conductivity of NCM materials is increasing with higher Ni content. It is also highly dependent on the SOC. The electronic conductivity for NCM111 differs by 6 orders of magnitude from Li_1MO_2 to $Li_{0.2}MO_2$.[121] Due to these properties the microstructure of cathode composites has to be actively considered to ensure good performance.[122,123] A sufficient amount of SE is needed to ensure ionic transport through the composite. More precisely, the SE particles must be connected to one another and form a percolating network. The CAM and carbon additives need to form a percolating network as well to ensure electronic transport throughout the electrode. Depending on the particle size of the CAM between 45 vol% for a particle size of 3 µm and 60 vol% for a particle size of 15 µm are needed to ensure CAM utilization of over 80 %.[70] Practical electrodes will most likely use around 70 vol% of CAM.[123] Furthermore, small particle sizes decrease the length of the diffusion pathways and increase the rate performance.[124] This is especially important due to the fact that pores in SSB are not filled with SE as opposed to systems using liquid electrolytes where the electrolyte can penetrate the pores of the CAM and effectively decrease the length of the diffusion pathways in the CAM.[120]

The size of the SE particles has to be chosen and tailored to the CAM in use according to a study by Minnmann et al.[123] Pores are an important factor as well as high porosity can lead to both electronic and ionic limitation in the electrode.[70] In order to eliminate the detrimental effect of pores, they could be filled with LEs.[70,123]

2.3 Degradation Mechanism in Composite Cathodes

Cathodes in SSB usually suffer from multiple pathways of degradation due to the instability of the thiophosphate SE. However, the CAMs themselves, especially layered oxides, are prone to degradation as well. At high voltages oxygen evolution leads to further degradation of the electrolyte and rock-salt formation on the active material.[125,126] The SE is unstable as well both in contact with the CAM and at high electrochemical potentials leading to degradation of the SE. Lastly, due to the volume expansion and contraction of the CAM during cycling morphological degradation can occur.

2.3.1 Electrochemical Degradation

Thiophosphate SEs are unstable against NCM materials.[82,127–130] When these SEs are subjected to high electrochemical potentials oxidation occurs. This effect is independent on the materials the SE is contacted to, i. e. it occurs upon contact to a current collector, upon contact to conductive additives and also upon contact to the CAM as long as the electrochemical potential at this interface is sufficiently high.

In thiophosphate SEs the S^{2-} building blocks are oxidized at around 2.6 V vs. Li^+/Li and the PS_4/PGe_4 building blocks are oxidized around 4.1 V vs. Li^+/Li.[130] This degradation is partially reversible. The formation of S^0 can be reversed if the potential is sufficiently low, however, when using NCM as CAM the potential is too high for this to happen even in the fully discharged state of the cell. The oxidation of PS_4/PGe_4 is not reversible. While the exact mechanism of the oxidation and the involved species remain elusive, the pathways can be depicted in a simplified manner according to eqs. (4).

$$S_x^{2-} \rightleftharpoons S_x^0 + 2e^- \tag{4a}$$

$$2PS_4^{3-} \rightleftharpoons P_2S_7^{4-} + S^0 + 2e^- \tag{4b}$$

2.3.2 Chemical Degradation

When CAMs are delithiated, i. e. oxidized, they become increasingly more unstable (see sec. 2.2.4 on page 10 and eq. (3a) on page 10). At high electrochemical potentials E of the cathode the oxygen in the CAM is released and can react with the SE. This effect has been measured with DEMS in liquid cells directly.[131,132] In SSB oxygen release is not measured directly but rather the formation of singlet oxygen $^1O_2$ leads to formation of SO_2.[133] This leads to degradation both on the SE and the CAM and is therefore detrimental to the performance and long-term stability of the cell. However, this effect is most pronounced at high electrochemical potential E or high SOC. Therefore it can be combated with low voltage cycling.[5,134] The actual threshold for oxygen release, rock-salt formation and chemical degradation depends on the specific CAM in use. For CAMs with low Ni content this threshold is higher compared to CAMs with high Ni content.[5,135] This effect is usually not taken into account when degradation and long-term stability is investigated. However, especially when SSBs are tested for long-term stability at high current densities, the overpotential at the cathode can be so high that the SOC above which rock salt formation occurs is never reached. This leads to lower degradation and a false positive result about the cycling stability of the material in question.

2.3.3 Chemomechanical Degradation

Chemomechanial degradation occurs due to volume expansion and contraction of CAM particles during cycling. On one hand this leads to contact loss between the SE and the CAM.[63] On the other, the CAM particles themselves can crack also leading to worse performance.[136]

Particle cracking in CAM in SSB worsens the performance because the diffusion pathways inside the particles are effectively increased and the electrochemically active mass is low-

ered.[136] The electrochemically active mass is the mass of CAM particles in the electrode that is actually utilized for cycling, as opposed to the total mass of the CAM in the electrode. The difference between the two arises from the fact, that not all CAM particles are electronically connected and thus some are not cycled but rather stay inactive. During cycling the electrochemically active mass is constantly reduced leading to capacity fading of the cell. This effect is more pronounced in polycrystalline materials compared to single crystalline materials. In polycrystalline materials the strain caused by the shrinking and expansion of the CAM particles during cycling leads to crack propagation. Prolonged cycling can lead to particle disintegration and loss in electrochemically active mass. In LIBs the same cracking doesn't lead to the same capacity fading because the resulting cracks are filled with LE. SEs are not able to flow in the cracks and therefore the detrimental effect on the cell's performance is more pronounced. This highlights the importance of choosing CAMs with good structural integrity to avoid capacity loss during cycling.

2.4 Coatings on Cathode Active Materials

The need for coatings on CAMs using thiophosphate SEs was realized already by Ohta et al. as early as 2007.[137] The $LiNbO_3$ coating investigated in that study is still used as a standard coating for CAMs today. The inherent instability of thiophosphate SEs must be addressed with coatings that prevent both electrochemical degradation of the SE and reaction of oxygen with the SE at high SOC. Despite high efforts a coating that fully suppresses degradation has not been reported yet.

2.4.1 Working Principles of Coatings

The working principle of coatings on CAMs for SSB is so far only partially understood. It is generally agreed, that coatings need to exhibit low electronic and sufficiently high ionic conductivities to ensure protection against electrochemical oxidation of the SE and functioning electrodes.[29,138] The mechanism of protection against chemical oxidation, however, remains elusive.

Table 2: Overview over coatings used in SSB with thiophosphate SEs. Adapted and complemented from Morchhale et al.[139]

Coating	Process	Material	Electrolyte	Ref
$LiNbO_3$	Sol-gel	various NCMs	Li_6PS_5Cl	[140]
$LiNbO_3$	Dry coated	NCM622	LGPS	[141]
$LiNbO_3$	ALD	LCO	$Li_7P_2S_8I$	[142]
$LiTaO_3$	Sol-gel	NCM821206	Li_6PS_5Cl	[140]

Table 2: Overview over coatings used in SSB with thiophosphate SEs. Adapted and complemented from Morchhale et al.[139]

Coating	Process	Material	Electrolyte	Ref
Li_2ZrO_3	Dry coating	NCM622	Li_6PS_5Cl	[143]
$LiWO_3$	Sol-gel	NCM622	$Li7P_2S_8I$	[144]
Li_2WO_4	Sol-gel	LCO	Li_6PS_5Cl	[145]
Li_2MoO_4	Sol-gel	NCA801505	doped Li_3PS_4	[146]
Li_3BO_3	Sol-gel	LCO	Li_6PS_5Cl	[147]
$Li_3B_{11}O_{18}$	Sol-gel	NCM523	Li_3PS_4	[148]
$LiB(C_2O_4)_2$	Sol-gel	NCM821206	Li_6PS_5Cl	[149]
Li_2TiO_3	Sol-gel	LCO	$Li_{9.54}Si_{1.74}P_{1.44}S_{11.7}Cl_{0.3}$	[150]
$Li_4Ti_5O_{12}$	Sol-gel	LCO	$Li_{9.54}Si_{1.74}P_{1.44}S_{11.7}Cl_{0.3}$	[150]
$Li_{0.5}La_{0.5}TiO_3$	Sol-gel	NCM523	Li_6PS_5Cl	[151]
$Li_{0.35}La_{0.5}TiO_3$	Sol-gel	NCM622	Li_6PS_5Cl	[152]
$Li_{0.35}La_{0.5}Sr_{0.05}TiO_3$	Sol-gel	NCM111	Li_6PS_5Cl	[153]
$Li_6ZnNb_4O_{14}$	Sol-gel	NCM851005	Li_6PS_5Cl	[154]
$LiAlO_2$	Sol-gel	NCM111	Li_3PS_4	[155]
Al_2O_3	Dry coating and annealing	NCM701515	Li_6PS_5Cl	[156]
HfO_2	ALD	NCM851005	Li_6PS_5Cl	[157]
TiO_2	Sol-gel	LCO	$Li_{9.54}Si_{1.74}P_{1.44}S_{11.7}Cl_{0.3}$	[150]
$TiNb_2O_7$	Sol-gel	NCM622	LGPS	[158]
ZrO_2	Sol-gel	NCM111	Li_3PS_4	[159]
Li_2CO_3	Sol-gel	NCM622	Li_3PS_4	[133]
Li_3PO_4	ALD	NCM811	LGPS	[160]
$Li_{1.4}Al_{1.4}Ti_{1.6}(PO_4)_3$	Sol-gel	NCM622	$Li_{10}SnP_2S_{12}$	[161]
$Li_{3.5}Si_{0.5}P_{0.5}O_4$	PLD	LCO	Li_2S/P_2S_5	[162]
$Li_2CO_3/LiNbO_3$	Sol-gel	NCM622	Li_3PS_4	[133]
$Li_2B_4O_7/LiNbO_3$	Dry coating	NCM811	Li_6PS_5Cl	[163]
Li_3BO_3/Li_2CO_3	Sol-gel	LCO	Li_6PS_5Cl	[147]
Li_2CO_3/Li_2ZrO_3	Sol-gel	NCM622	Li_6PS_5Cl	[164]
$LiNbO_3/Li_3PS_4$	Dry coating	NCM111	Li_3PS_4	[165]
$LiInO_2$-LiI	Sol gel	NCA801505	Li_2S/P_2S_5	[166]
PEDOT	MVD	NCM811	LGPS	[167]
$LiInO_2$-LiI	Sol gel	NCA801505	Li_2S/P_2S_5	[166]

Table 2: Overview over coatings used in SSB with thiophosphate SEs. Adapted and complemented from Morchhale et al.[139]

Coating	Process	Material	Electrolyte	Ref
PVBTA-TFSI	Spray-drying	NCM851005	Li_6PS_5Cl	[168]
PAN	Sol-gel	NCM811	Li_6PS_5Cl	[169]
$Li_{1.4}Al_{1.4}Ti_{1.6}(PO_4)_3$/PAN	Sol-gel	NCM622	LGPS	[170]
$LiNbO_3$/C65	Sol-gel and dry mixing	NCM622	Li_6PS_5Cl	[171]
diamond-like carbon	CVD	NCA801505	Li_2S/P_2S_5	[160]
Li_3PS_4/O_2	Dry coating	NCM851005	Li_6PS_5Cl	[172]
Li_6PS_5Cl/O_2	Dry coating	NCM851005	Li_6PS_5Cl	[172]

2.4.2 Classes of Coatings

Over the past years a multitude of different coatings have been reported in literature. However, most of these can be classified into one of the following types.

Transition Metal Oxide coatings are the most common type of coatings for NCM type CAMs. The most common ones are $LiNbO_3$, Li_2ZrO_2 and $LiTaO_3$.[140,143] These coatings contain highly oxidized transition metals such as Nb^V, Zr^{IV} and W^{VI} that are unsusceptible to further oxidation. The low susceptibility to oxidation should protect the SE from chemical degradation, i. e. oxygenation, when high SOCs of the CAM are reached and oxygen from the CAM is released. Electrochemical protection is only achieved if the electronic conductivity of the coating is low enough. However, measuring electronic conductivity is very difficult, if not impossible, and therefore reliable data is not available. It is sometimes assumed that the electronic conductivity values of the bulk crystalline material will have the same electronic conductivity as the coating. This assumption is incorrect because the coating is not a pure material and is very thin and therefore dominated by surface effects.

Natural Coatings are coatings on the surface of CAMs that form more or less intentionally during synthesis. In the case of layered oxides these mainly consist of LiOH, Li_2O and Li_2CO_3. Studies have shown, that this natural coating layer helps with the electrochemical performance of SSB.[173] As a consequence many artificial coatings are actually hybrid coatings consisting of the intentional coating species and the natural coating species.[133]

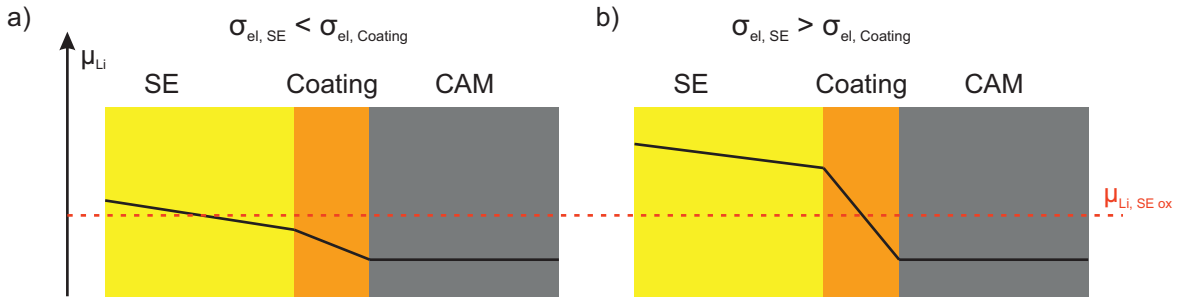

Figure 2: The electronic conductivity of a coating is an important property to ensure electrochemical protection of the SE. a) The electronic conductivity of the coating is higher than that of the SE, $\sigma_{\text{el, coating}} > \sigma_{\text{el, SE}}$. The chemical potential of Li μ_{Li} at the interface of the SE and the coating is still lower than the threshold of oxidation $\mu_{\text{SE, ox}}$ and the SE will be oxidized. b) The electronic conductivity of the coating is lower than that of the SE, $\sigma_{\text{el, coating}} < \sigma_{\text{el, SE}}$. In this case the chemical potential at the interface of SE and coating is already above the oxidation threshold and the SE remains stable. Adapted from Nakamura et al.[138]

Halide Solid Electrolytes could serve as protective layer between CAM and thiophosphate SE. They exhibit high oxidation stability and good ionic conductivity σ_{ion} (see chapter 2.2.2). When used in combination with thiophosphate electrolytes strong degradation at the three-phase contact points of thiophosphate SE, halide SE and CAM occurs leading to strong degradation and detrimental cell performance.[174] In order to avoid that, this three-phase contact point has to be avoided making the use of halide SE as coatings for thiophosphate based SSB challenging.

Polymer Solid Electrolytes are currently rarely used in SSB with only two publications to date.[167,168] Due to the ductile nature of polymers they could help mitigating chemo-mechanical degradation by acting as a protective layer between SE | CAM reducing the mechanical stress induced to volume expansion and shrinking of the CAM during cycling. This is however still hypothetical and needs further research.

Thiophosphate Solid Electrolytes can serve as coatings themselves if they are intentionally oxidized prior to their use in cathode composites. The SE is coated on the CAM in a simple dry mixing process. Afterwards the SE is deliberately oxidized using air or O_2 at around 300 °C.[172] This leads to the formation of an artificial SEI layer. Therefore, the CAM is in contact to oxidized SE already preventing further degradation.

2.5 Impedance Spectroscopy

Electrochemical impedance spectroscopy (EIS) is one of the most widely used analytical techniques in battery research. This is mainly due to the fact, that EIS is a non-destructive

technique that can be applied at any stage of a cell's life. It uses a periodic input (voltage U or current i) and measures a resulting periodic output of the same frequency (current i or voltage U). Typical frequency ranges for electrochemical measurements are between 10^7 Hz and 10^{-3} Hz. The ratio between the two is called the impedance $Z(\omega)$ usually expressed as complex variable consisting of the magnitude $|Z|$ and the phase Θ (or alternatively as $\mathrm{Re}(Z)$ and $\mathrm{Im}(Z)$).

The impedance response of any system can in principle be modeled with only three basic circuit elements; a resistor R, a capacitor C and inductance L.

$$Z_R = R \tag{5a}$$

$$Z_C = \frac{1}{j\omega C} \tag{5b}$$

$$Z_L = j\omega L \tag{5c}$$

In principle these three elements can be used to describe any impedance response and any system. However, in practice, more complex circuit elements, such as constant-phase elements (Q), Warburg impedance (W) or Gerischer impedance (G) are not directly based on these elements.

2.5.1 Requirements and Validation

Reliable EIS measurements need to fulfill three conditions in order to qualify as reliable measurement that models can be applied to.

Stability The system under investigation needs to be stable and not change significantly over the course of the measurement time of a single measurement. It is however possible to record repeated EIS measurements and follow the impedance evolution over time. In this case the system changes over time and is not stable, it is however sufficient when this change is slow enough to not disturb single measurements.

Causality The output signal of a system must be entirely caused by the input signal. Any other contribution to the output signal will lead to erroneous impedance data. The most commonly observed disturbance is at a frequency of $\nu = 50$ Hz. Detecting these disturbances is challenging but can be achieved with Kramers-Kronig tests.

Linearity describes the property of the system, that the impedance is independent of the input signal's amplitude. Electrochemical systems are generally not linear, however,

if the input amplitude is chosen to be sufficiently small, electrochemical systems often behave quasi-linear.

Kramers-Kronig Test In order to extract physically meaningful parameters out of impedance spectra all of the above criteria have to be fulfilled. Ensuring that these criteria are actually met is challenging and a method to test for this is needed that only relies on the impedance data itself.[175,176] The Kramers-Kronig relations can serve as such a test for impedance data. If all of the criteria stability, linearity and causality are fulfilled the Kramers-Kronig relations describe a mathematical correlation between real and imaginary part of the impedance data. In other words, the real part $\mathrm{Re}\,(Z_{\mathrm{meas}})$ can be calculated using the imaginary part $\mathrm{Im}\,(Z_{\mathrm{calc}})$ and the imaginary part $\mathrm{Im}\,(Z_{\mathrm{meas}})$ can be calculated using the real part $\mathrm{Re}\,(Z_{\mathrm{calc}})$. This new dataset can then be used to calculate residuals e.

$$e(\mathrm{Re}) = \mathrm{Re}\,(Z_{\mathrm{meas}}) - \mathrm{Re}\,(Z_{\mathrm{calc}}) \tag{6a}$$

$$e(\mathrm{Im}) = \mathrm{Im}\,(Z_{\mathrm{meas}}) - \mathrm{Im}\,(Z_{\mathrm{calc}}) \tag{6b}$$

In literature there is no threshold or other metric agreed upon up to where residuals are acceptable or not. However, two sources for the residuals should be distinguished. First, the noise of the measurement. This will show up in the residuals of the Kramers-Kronig test as noise as well. However, in this case the residuals will not show any characteristics when plotting the residuals e vs. the frequency ν. The Kramers-Kronig test can still be used to estimate the amplitude of the noise. Depending on the complexity of the model used to describe or fit the impedance data suitable levels for the noise can be assigned. Second, residuals resulting from actual shortcomings of the criteria for impedance measurements described above. These will show up in the residuals e as characteristic attributes when plotting e vs. ν. An example using simulated data is shown below for both cases in fig. 3.

Characteristic frequencies of physical processes In commonly used Nyquist plots where $\mathrm{Re}(Z)$ is plotted vs. $-\mathrm{Im}(Z)$ different physical processes appear at different frequencies. The specific frequency ν_{spec} of a process is $\max\left[-\mathrm{Im}(Z)\right]$. This term is most commonly used in conjunction with RC elements. The impedance and the specific frequency of an RC elements are described as follows:

$$Z = \frac{R}{1 + j\omega RC} \tag{7a}$$

$$\nu_{\mathrm{spec}} = (2\pi RC)^{-1} \tag{7b}$$

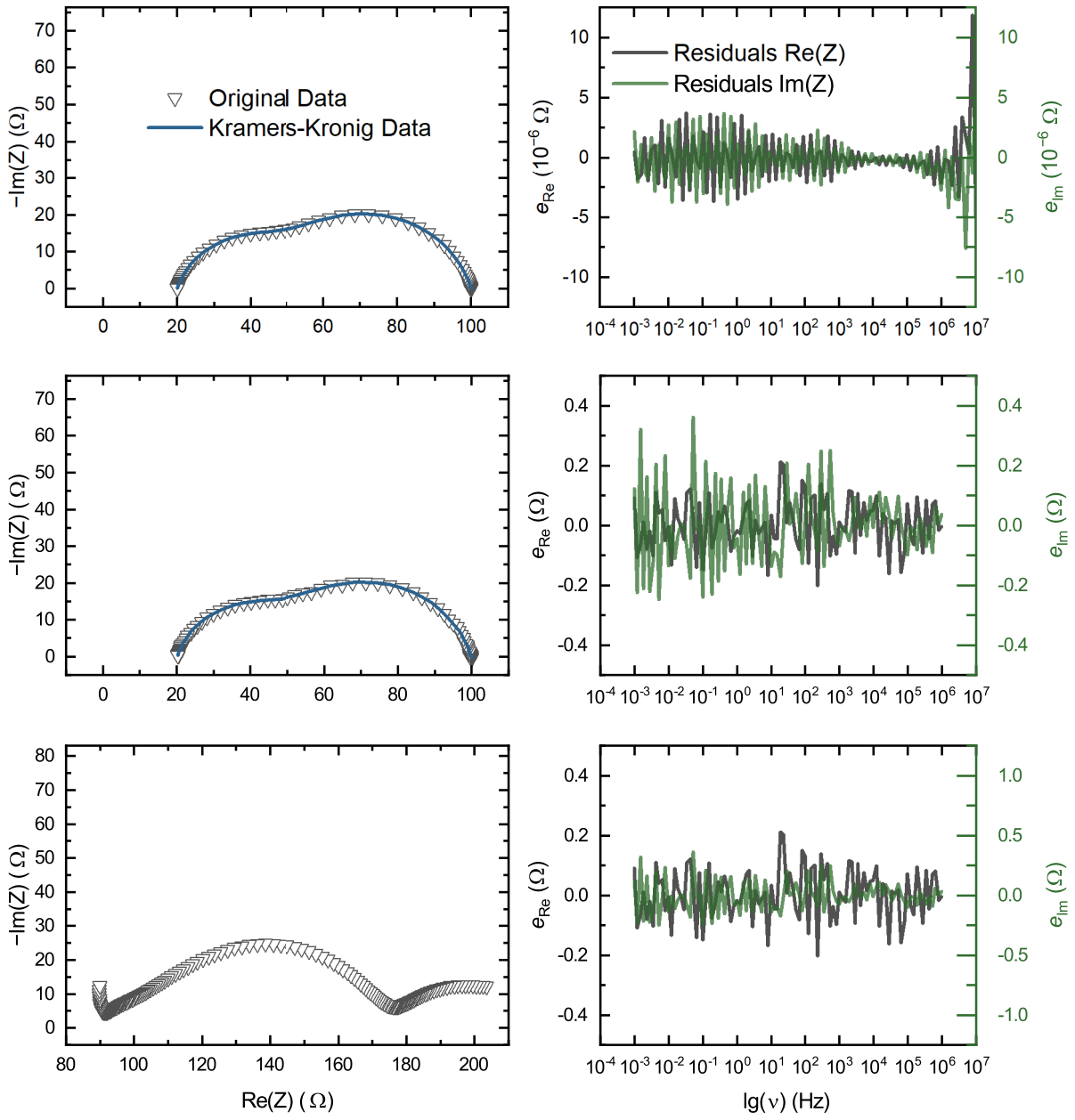

Figure 3: Commonly observed types of residuals in Kramers-Kronig tests. a) Residuals stemming from noise of the measurement. No characteristics are observed. b) Residuals stemming from a lack in stability, causality and linearity. Characteristics can be observed such as periodic behavior or peaks at certain frequencies.

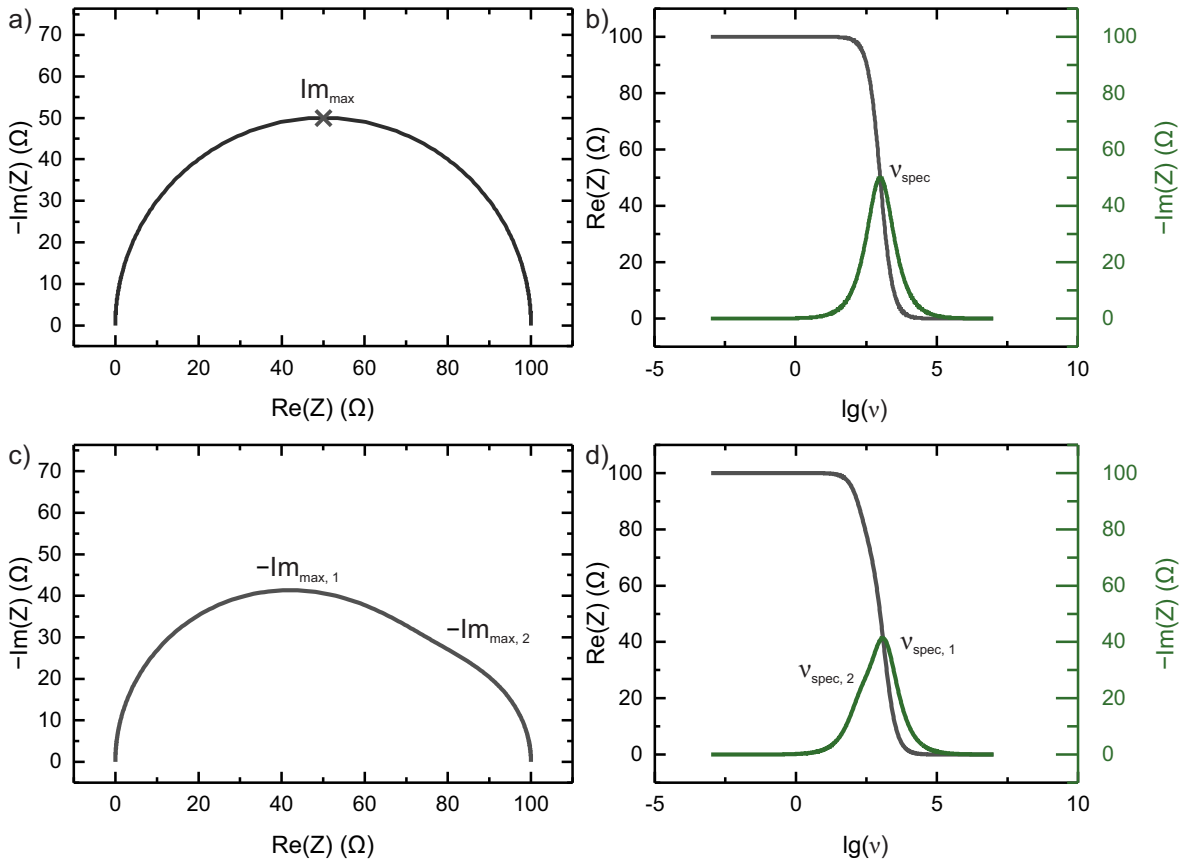

Figure 4: The specific frequency of a process is the frequency where $-\mathrm{Im}(Z)$ is at it's maximum as can be seen in the Nyquist plot in a) and the Bode plot in b). For a single process this frequency is easy to identify. Several processes however can quickly overlap as shown in c) and d).

These specific frequencies can be used to identify different processes in an electrochemical system.[177]

2.6 Equivalent Circuits and Models for SSB

Analyzing impedance data of SSBs is highly challenging due to the complexity of the systems. A full cell consists of many individual parts which often overlap in the resulting impedance spectra. The main contributions to impedance spectra are the ionic resistance of the SE separator, the charge-transfer between anode and SE, the charge-transfer between SE and CAM and the ionic resistance in the cathode composite. When CAMs with low Ni content and no conductive additives such as carbon are used the electronic resistance in the cathode composite becomes significant contribution to the impedance as well.

To date, there is no universally accepted model for SSB cathode composites, yet alone SSB full cells. The two most commonly used are described in more detail below in chapters 2.6.1 and 2.6.2. Generally, there is always a trade-off between physical accuracy and

simplicity of the model. Equivalent circuits based on RC or RQ elements are easy to fit and interpret as they are based on relatively few parameters. However, the parameters extracted from such models can not be converted to actual physical quantities such as charge-transfer resistance, ionic or electronic conductivity.

Physically more accurate models such as transmission-line models are usually more difficult to fit to measured data and they often require a priori knowledge of the system such as ionic conductivity of a composite.[120,122]

2.6.1 RC-based Equivalent Circuits

The most commonly type of model/equivalent-circuit for SSB found in literature consists of a series of parallel RC-elements as shown in fig. 5. Often, the capacitor C is replaced with a constant phase element Q. Individual RC- or RQ-elements show up as semicircles (RC) or depressed semicircles (RQ) in Nyquist plots. Usually, one physical process is attributed to one of these RC- or RQ-elements. For example, one RC- or RQ-element is used for the ionic conductivity of the SE, or for the charge-transfer of the between SE and the anode, for the charge-transfer between the SE and the CAM.[127,178]

While these models are very simple, they are not well suited for determining actual physical parameters. However, in cases where it is sufficient to find trends in the impedance evolution of a cell these types of equivalent circuits offer an easy way to identify degradation mechanism in the cell.

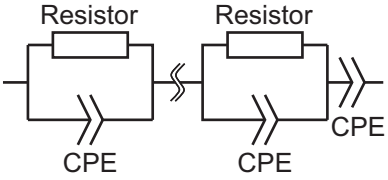

Figure 5: Serial connection of parallel RC-circuits commonly used to fit and describe impedance data of SSBs. The constant-phase element is used to describe Li^+-diffusion in the CAM.

2.6.2 Transmission Line Models

Transmission line models (TLM) are found more recently in literature.[122,123,179] In these types of models, composites are described with two pathways of conduction, ionic and electronic. A general equivalent circuit of a TLM is shown in eqs. (8a) and (8b).

$$Z_{\mathrm{TLM}} = \frac{Z_{\mathrm{ion}} Z_{\mathrm{el}}}{Z_{\mathrm{ion}} + Z_{\mathrm{el}}} \left(l_{\mathrm{elec}} + \frac{2\kappa}{\sinh\left(\frac{l_{\mathrm{elec}}}{\kappa}\right)} \right) + \kappa \frac{Z_{\mathrm{ion}}^2 + Z_{\mathrm{el}}^2}{Z_{\mathrm{ion}} + Z_{\mathrm{el}}} \coth\left(\frac{l_{\mathrm{elec}}}{\kappa}\right) \tag{8a}$$

$$\text{where } \kappa = \left(\frac{Z_{\mathrm{CT}}}{Z_{\mathrm{ion}} + Z_{\mathrm{el}}} \right)^{\frac{1}{2}} \tag{8b}$$

Usually, the ionic and electronic pathways are described with a simple resistor, so $Z_{\mathrm{el}} = R_{\mathrm{el}}$ and $Z_{\mathrm{ion}} = R_{\mathrm{ion}}$. The connection between ionic and electronic conduction pathways is more complicated. It needs to take the charge-transfer between SE and CAM into account as well as the diffusion of Li^+ and e^- in the CAM. Furthermore, formation of degradation layers on the CAM and the SE might be taken into account. The charge-transfer is usually described with a RC or RQ element and the diffusion in the CAM is often described with a constant phase element. A more physically correct model would be a Warburg short element W_{S} which accurately describes a limited diffusion in one direction.

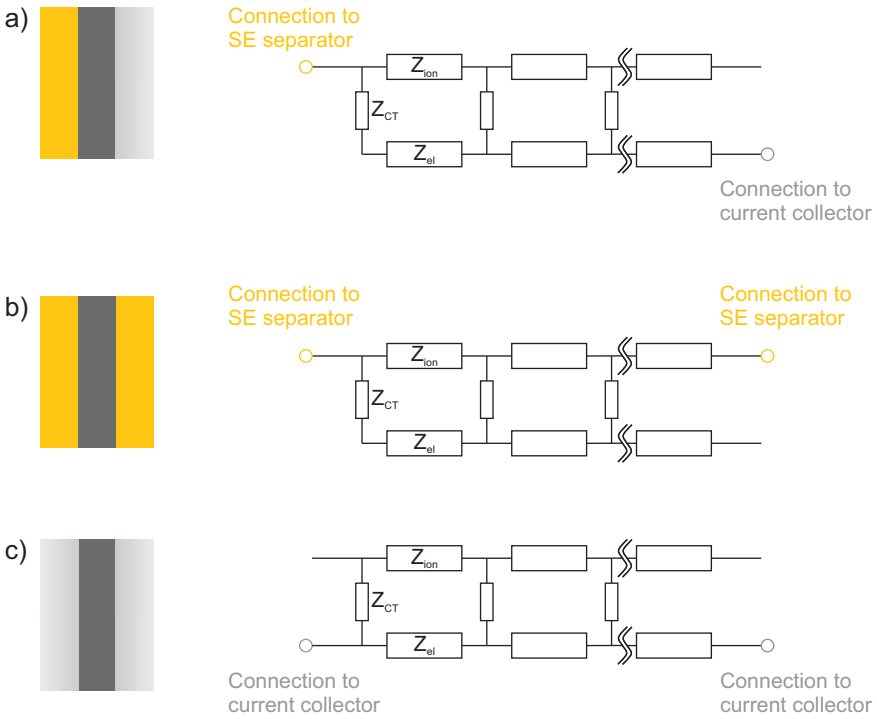

Figure 6: General transmission line model circuit as used in full cells. a) TLM for a cathode composite in a full cell. b) TLM for a cathode composite in an electronically blocking setup. c) TLM of a cathode composite in an electronically setup

2.7 Three-Electrode Measurements

When measuring a setup with two electrodes only one voltage can be obtained from that system. This value therefore always contains information of the full cell. However, often only one of the electrode is of particular interest. Introducing a reference electrode (i. e. an

electrode with an a priori known potential) allows measuring two independent voltages. This enables a separation of the two electrodes and simplifies the analysis and evaluation of the performance of the cell.

2.7.1 Potentials of Quasi Reference Electrodes

Electrochemical cells can be constructed with a third electrode in addition to cathode and anode. These electrodes are usually made out of another material than the other electrodes and therefore, the electrochemical system is rather undefined. To get a better understanding of these systems, the following model system will be used to explain the voltages and potentials obtained.

$$\mathrm{Li}\,|\,\mathrm{LE}\,|\,\mathrm{Ref(X)}\,|\,\mathrm{LE}\,|\,\mathrm{Li}$$

where Li is lithium metal, LE is a liquid electrolyte able to conduct Li^+ ions, Ref(X) is a third electrode embedded in the electrolyte and is made out of another metal. The following reaction occurs when a current is applied to the cell.

$$\mathrm{Li} \rightleftharpoons \mathrm{Li}^+ + e^- \tag{9}$$

The open circuit potential (OCP) of these electrodes is:

$$E(\mathrm{Li}) = E^0(\mathrm{Li}) + \frac{RT}{zF} \ln\left(\frac{a(\mathrm{Li}^+)}{a(\mathrm{Li})}\right) = \text{const.} \tag{10}$$

Note that, the OCP of both electrodes is well defined.
Additionally, on the third electrode Ref(X) the following reaction can occur in contact with the liquid electrolyte:

$$\mathrm{X} \rightleftharpoons \mathrm{X}^{k+} + ke^- \tag{11a}$$

$$\mathrm{Li}^+ + e^- \rightleftharpoons \mathrm{Li} \tag{11b}$$

During this reaction the metal from the third electrode X is dissolved into the electrolyte and the metal M is plated/alloyed into the third electrode. The OCP of these reactions is:

$$E(\mathrm{Li}) = E^0(\mathrm{Li}) + \frac{RT}{zF} \ln\left(\frac{a(\mathrm{Li}^+)}{a(\mathrm{Li})}\right) \tag{12a}$$

$$E(\mathrm{X}) = E^0(\mathrm{X}) + \frac{RT}{zF} \ln\left(\frac{a(\mathrm{X}^{k+})}{a(\mathrm{X})}\right) \tag{12b}$$

Note that, these potentials are neither known nor well defined. The activity of metal M $a(\mathrm{M})$ on the third electrode is not known and very low and arises from impurities on

the electrodes. It can also change from sample to sample due to little variations of these impurities. The same is true for the activity $a(\mathrm{X}^{k+})$. It only arises from impurities in the electrolyte and is very low. Combining these potentials in the reaction $n\mathrm{X} + k\mathrm{M}^{n+} \rightleftharpoons n\mathrm{X}^{k+} + k\mathrm{M}$ leads to the following voltage.

$$\Delta E = \Delta E^0 + \frac{RT}{zF} \ln \left(\frac{a(\mathrm{Li}^+)\, a(\mathrm{X})}{a(\mathrm{Li})\, a(\mathrm{X}^{k+})} \right) \tag{13}$$

This voltage is very high and therefore it is expected that a small amount of metal M is alloyed into the third electrode Ref(X). After the reaction between electrolyte and the third electrode Ref(X) is finished it is therefore expected that Ref(X) will show a stable, albeit a prioriunknown, potential vs. the metal electrodes. Generally, high voltages vs. metal electrodes are expected. In the case of gold electrodes in $\mathrm{Li_6PS_5Cl}$ this voltage turns out to be about 2.5 V vs. $\mathrm{Li^+/Li}$.

Solid electrolytes For solid electrolytes the same considerations apply. However, formulas (11a) and (11b) have to be altered. In the case of SEs precise compositions are probably difficult to formulate. In any case, the activities of oxidized metal X of the third electrode in the solid electrolyte will still be very low and the activity of metal M in the third electrode Ref(X) will also be very low. Therefore, one arrives at the same conclusion as for an liquid electrolyte.

2.7.2 Potentials on Reference Electrodes

An electrochemical cell with a third electrode exhibiting a stable and well-known potential is called a reference electrode. The most widely referenced electrode is the standard hydrogen electrode (SHE) with a defined potential of 0 V at an $\mathrm{H^+}$ activity of 1 as shown in eqs. (14a) and (14b). Due to the difficult usability this system is rarely used in practice. More commonly, silver chloride (AgCl/Ag) electrodes shown in eqs. (14c) and (14d) with defined chloride ion activities are used. When reference electrodes are used in systems with liquid electrolytes the concentrations/activities of the species involved in the redox reaction have to be strictly controlled in order to ensure stable and well-known potentials. In case of the SHE this means controlling both the $\mathrm{H^+}$ activity in the electrolyte and the $\mathrm{H_2}$ pressure. In case of the AgCl/Ag electrode this means controlling the $\mathrm{Cl^-}$ activity in the electrolyte.

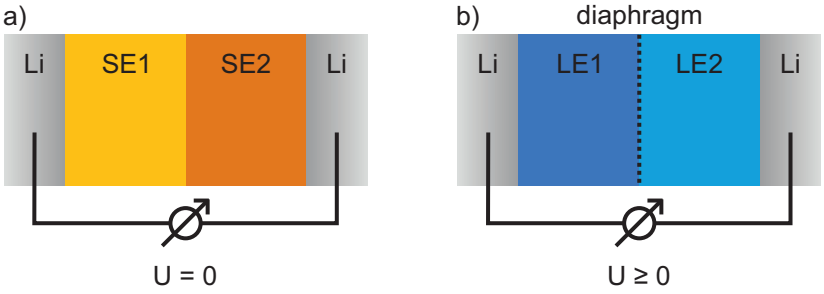

Figure 7: a) The voltage measured in a system with two identical electrodes, e. g. lithium metal, is zero even if the electrodes are contacted by different solid electrolytes SE1 and SE2. The potential drop across the junction of the two electrolytes cancels out the potential caused by the two electrodes in contact with different electrolytes. b) In a similar system with liquid electrolytes a voltage can generally be measured.

$$\mathrm{H^+ + e^- \rightleftharpoons \frac{1}{2} H_2} \tag{14a}$$

$$E(\mathrm{SHE}) = E^0(\mathrm{SHE}) + \frac{RT}{zF} \ln\left(\frac{a\,(\mathrm{H^+})}{a\,(\mathrm{H_2})}\right) \tag{14b}$$

$$\mathrm{AgCl + e^- \rightleftharpoons Ag + Cl^-} \tag{14c}$$

$$E(\mathrm{AgCl/Ag}) = E^0(\mathrm{SHE}) + \frac{RT}{zF} \ln\left(\frac{\mathrm{K_L(AgCl)}}{a\,(\mathrm{Cl^-})}\right) \tag{14d}$$

In systems using SEs it is not necessary to control the concentration/activity of ions in the electrolyte. The voltage between two lithium electrodes is always 0 in contrast to a liquid-liquid junction where a voltage can usually be measured as shown in fig. 7. The voltage that arises from different electrolytes in a concentration cell is described by the Nernst equation (15a) and the voltage that arises at the junction of two electrolytes is described by (15b). In the case of SEs there is only mobile ion species and therefore the transference number is 1, so $t_{\mathrm{Li^+}} = 1$. If the transference number is 1, then the voltage across a SE | SE junction is equal to the voltage caused by different electrolytes. Therefore, the resulting voltage of such a cell is always 0.

$$\Delta E = \frac{RT}{zF} \ln\left(\frac{a_1\,(\mathrm{Li^+})}{a_2\,(\mathrm{Li^+})}\right) \qquad \text{concentration cell} \tag{15a}$$

$$\Delta E = -\frac{RT}{zF} \sum_i t_i \ln\left(\frac{a_{1,\,i}}{a_{2,\,i}}\right) \qquad \text{diffusion potential} \tag{15b}$$

$$\Delta E = -\frac{RT}{zF} \ln\left(\frac{a_1\,(\mathrm{Li^+})}{a_2\,(\mathrm{Li^+})}\right) \qquad \text{lithium SEs} \tag{15c}$$

2.8 Post Mortem Analytical Techniques

2.8.1 Time-of-Flight Secondary Ion Mass Spectrometry

Time-of-flight secondary ion mass spectrometry is an analytical technique with high surface-sensitivity and low information depth. Primary ions, such as Bi_3^{2+} are used to ionize species on the surface of a sample. The resulting secondary ions are then measured in a time-of-flight detector. Due to the indirect ionization, species in the sample are not measured directly. Instead, ions resulting from a ionization cascade are measured. This ionization cascade is not only dependent on the chemical species itself but also the matrix surrounding these species, i. e. the resulting ions from a specific chemical species can vary depending on the surrounding species. This is called the matrix effect. Because of that, the analysis of these ions has to be taken out carefully to not arrive at wrong conclusions.

In principle, ToF analyzers work quantitatively, however, due to the fact, that the species in the sample are measured indirectly in the form of secondary ions means that ToF-SIMS is only a semi-quantitative technique.

A big advantage of ToF-SIMS is it's very high sensitivity in the ppm to ppb range and in specific cases down to $10^{12}\,\frac{\text{ions}}{\text{cm}^3}$.[180,181] This allows the detection and quantification of a wide range of ions.

Due to the amount of signals it can be difficult to determine which ions correlate to degradation and which ions do not. Comparing samples without degradation and with samples with degradation would be very time consuming and unreliable. This is why, for an advanced analysis, a statistical approach using PCA, explained in more detail in sec. 2.9 on page 28, is helpful.

2.8.2 X-Ray Photoelectron Spectroscopy

X-ray photoelectron spectroscopy (XPS) is a surface-sensitive analytical technique with an information depth of around 7 nm – 18 nm.[182,183] It is used to determine the elemental and chemical composition of a sample. X-rays are used to excite photoelectrons out of the sample whose kinetic energy is then measured to determine the binding energy of the electron in the sample.

XPS has been used to investigate degradation in thiophosphate-based SSBs both at the anode and the cathode interfaces.[81,84,184] At the Li | LGPS interface reduction of the LGPS electrolyte can be observed.[81,184] In this case reduction of the thiophosphate electrolyte to Li_2S can be observed. Conversely, on the cathode oxidation of the thiophosphate electrolyte can be observed.[82–84]

This was used in a study by Kim et al. to show an the beneficial effect of a $LiNbO_3$ coating on NCM622 compared to the pristine material.[133] However, the signal-to-noise ratio of

XPS is comparably low and the detection limit of specific species is around 1 at%.[185] This makes distinguishing several coatings difficult. Furthermore, oxygenated sulphur species can hardly be detected with XPS due to their low concentration. That means, that XPS is only suited for detecting electrochemically oxidized sulphur and chemically oxidized phosphorus species. Therefore, XPS is not well suited for the degradation analysis of thiophosphate-based SSB cathodes due to high detection limit and lack of differentiating between the different pathways of degradation.

2.9 PCA Assisted Degradation Analysis of ToF-SIMS Data

The main purpose of PCA is to reduce the dimensionality of datasets without losing significant amounts of information. Here, this will be used to reduce the dimensionality of ToF-SIMS data. Here, each ion fragment ($n > 70$) is a dimension and is analysed in terms of it's intensity. As this is way too much to visualize properly which fragments are related to degradation a reduction of the dimensions is necessary.

PCA transforms these dimensions in such a way that, the first dimension, i. e. the first principal component, describes most of the variance (or information) of the data. This is visualized in fig. 8. First, the data is centered so that the average of each dimension/axis is $m = 0$ (fig. 8a and b). Next, the principal components are determined such that the first PC describes the most variance of the data. The second PC is orthogonal to the first PC and describes most of the leftover variance (fig. 8b). In case of more dimensions this is repeated until the the number of PCs is equal to the number of dimensions. Lastly, the data is replotted with the PCs as the new axis. Note, that until there, the data was only transformed. Finally, higher dimensions can be omitted from the representation as they only describe very little variance and thus contain only little information. In fig. 8 it can be seen that most of the information lies on PC 1 and the data is scattered around PC 2. Thus, PC 2 could be omitted for further analysis.

In a next step, the loadings of the principal components are calculated. The loadings are a linear combination of the original axes/dimensions and combined they make up the new principal components. In the example in fig. 8 PC 1 is made up of a positive contribution of x_1 and x_2 while PC 2 is made up of a negative contribution of x_1 and a negative contribution of x_2. For ToF-SIMS data this can help identifying which fragments correlate most with the variance in the data.

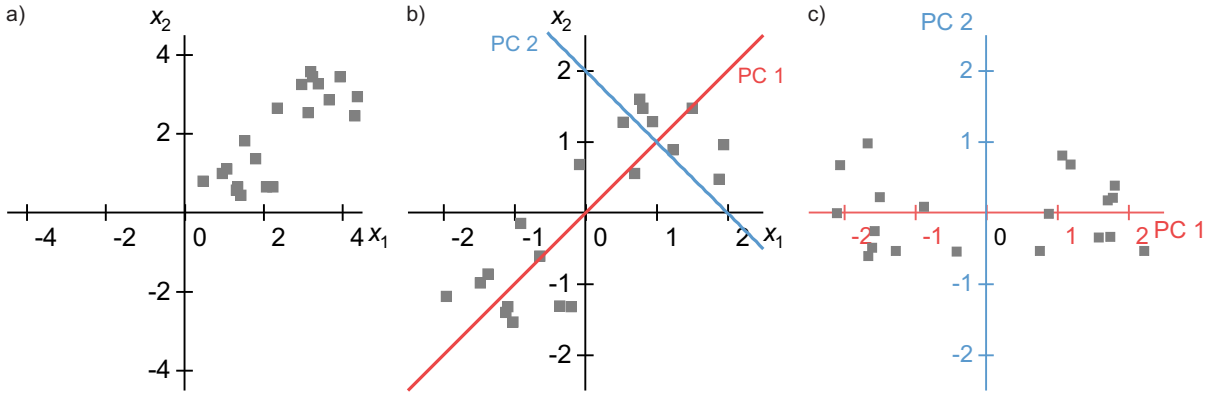

Figure 8: Exemplary representation of a PCA. a) raw data, the data is described in terms of two variables x_1 and x_2. In ToF-SIMS analysis x_1 and x_2 would be two fragments and their respective intensities. b) The data is centered so that the mean of each variable is 0. PC 1 is calculated so that most variance of the data lies on this line. PC 2 is calculated so that it is orthogonal to PC 1 and describing the most leftover variance. Data with higher dimension are calculated accordingly. c) The axis are rotated. Now, most of the variance is described with PC 1. In this example the data can almost fully be fully explained in terms of PC 1 whereas the data is randomly scattered around PC 2.

3 Publications

At the beginning of this thesis project, many studies investigating interfacial degradation in SSB cathodes could be found in literature. While the advantageous effect of protective coatings was already discussed as early as 2006 by Ohta et al.,[137,186] these publications usually focused on the simple comparison of coated and uncoated samples and the true effect of the coatings was rarely discussed in detail. Furthermore, these studies focused mostly on long-term cycling and rate-tests using simple 2E setups to investigate both the stability of the coatings against the SE as well as the kinetics of the coatings. While these approaches are straight forward they come with several downsides.

Long-term cycling stability is affected by many factors such as interfacial stability of CAM | SE interface, morphological degradation and crystallinity of the SE. However, only the interfacial stability of the CAM | SE interface is affected by a coating. In many systems the other effects have a stronger influence on the long-term stability and therefore it is difficult to make statements about the effect of the coating itself. Rate tests performed with simple 2E setups always suffer from the influence of the counter-electrode (i. e. the anode in this thesis) and an usually unknown overpotential is introduced. This effect cannot be considered using a 2E setup. Furthermore, 2E impedance measurement always contain contributions from the counter-electrode (anode) complicating the analysis.

Another gap in literature was the lack of comprehensive and systematic approaches to compare the effect of different coatings on the electrode's and cell's performance. Research focused on simple yet incomplete characterizations of coated CAMs.

Publication I therefore focuses on the introduction of a 3E setup for SSB to allow for a more comprehensive analysis of SSB electrodes without the detrimental influence of a counter-electrode. Publication II focuses on systematic benchmarking of several coated and uncoated CAMs. Existing knowledge was brought together and enhanced to give future researchers a better understanding of the performance of coatings for CAMs in SSB.

3.1 Publication I

In the first publication of the thesis a novel 3E setup for SSB was developed. This setup enables the independent investigation of both electrodes separately with minimal influence on potential full cell measurements. Before this thesis 3E setups were not used in SSB although their advantages are well establish in electrochemistry in general and LIB research specifically.

Due to the advantages of 3E setups, until now, several publications have been published describing different variations and possibilities to use multiple electrodes in SSB.[187–192] Because the challenges and considerations for building 3E setups for SSBs are independent of the cell chemistry, the main concept is now also used in Na-SSB and K-SSB.[193,194]

In the future this concept can be adapted to fabricate even more complicated cell setups. For example, the setup can be used to build 4-electrode cells. This would allow measuring contact resistances of different electrolytes reliably. This has been done for air-stable electrolytes such as LLZO, PEO, and oxygen-ion conductors.[195–197]

This study was part of the International Network for Batteries and Electrochemistry by BASF SE. The project was accompanied by X. Wu through scientific exchange. Reprinted from Hertle, J; Walther, F.; Mogwitz, B; Schröder, S.; Wu, X; Richter, F. H.; Janek, J.; Miniaturization of Reference Electrodes for Solid-State Lithium-Ion Batteries; *J. Electrochem. Soc.*, 170 (4), 040519, **2023**. doi:10.1149/1945-7111/accb6f;

J. Hertle designed the experiments and the cell design, analyzed the results and wrote the manuscript. F. Walther carried out ToF-SIMS experiments and helped with the experimental design and the structure of the manuscript. B. Mogwitz carried out FIB-SEM experiments. S. Schröder built and cycled cells. X. Wu helped with scientific feedback. F. H. Richter helped with scientific feedback and correction of the manuscript. J. Janek supervised the study.

Journal of The Electrochemical Society, 2023 **170** 040519

Miniaturization of Reference Electrodes for Solid-State Lithium-Ion Batteries

Jonas Hertle,[1,2] Felix Walther,[1,2] Boris Mogwitz,[1,2] Steffen Schröder,[1,2] Xiaohan Wu,[3] Felix H. Richter,[1,2] and Jürgen Janek[1,2,z]

[1]*Institute of Physical Chemistry, Justus Liebig University Giessen, Heinrich-Buff-Ring 17, 35392 Giessen, Germany*
[2]*Center for Materials Research (ZfM), Justus-Liebig-University Giessen, Heinrich-Buff-Ring 16, 35392 Giessen, Germany*
[3]*BASF SE, 67056 Ludwigshafen, Germany*

Enabling simple three-electrode (3E) setups for solid-state battery cells is important allowing investigation of individual electrodes to shed more light on interface charge transfer and reactions occurring in solid-state battery cells. Two different 3E setups are compared, and their practical value is evaluated. A miniaturized reference electrode (μ-RE) is developed from lithium-plated gold wires with a tungsten core providing a stable potential. Cells with Li_6PS_5Cl as solid electrolyte, $Li_{1-x}Ni_{0.85}Co_{0.10}Mn_{0.05}O_2$ (NCM851005) as cathode active material and $Li_4Ti_5O_{12}/Li_7Ti_5O_{12}$ (LTO) or In/InLi as anode are investigated. The reference electrode provides a stable potential of 0 V vs Li^+/Li, hence allowing the precise measurement of single electrode potentials. The setup leaves the usual cell geometry essentially unchanged and causes only minor additional work during cell assembly, allowing widespread application. Evidence is provided that 3E setups are needed to evaluate the rate capability of active materials correctly and that two-electrode (2E) setups can massively underestimate the rate capability of electrodes. The impedance of full cells is systematically analyzed based on separate anode and cathode impedances.
 [DOI: 10.1149/1945-7111/accb6f]

Manuscript submitted January 31, 2023; revised manuscript received March 13, 2023. Published April 19, 2023.

Supplementary material for this article is available online

Solid-state batteries (SSB) are a promising technology for future energy storage i.e. in electric vehicles or mobile devices.[1–3] By using a less flammable solid electrolyte (SE), the safety of SSBs is inherently increased compared to liquid electrolyte-based lithium-ion cells.[4–6] A higher energy density is expected once the lithium metal anode can be applied, and a wider temperature window for operation might ease the construction of battery packs. Despite these potential advantages SSBs are not yet competitive with their liquid counterparts.[7–10] Degradation occurs at both the lithium metal anode and the cathode, leading to capacity fading and decreasing rate performance.[7,11,12] This is particularly true in the case of lithium thiophosphate SEs that currently show the highest ionic conductivity among all SEs and are needed for the construction of competitive SSBs—at least as catholyte. Understanding the degradation processes at both electrodes separately and with high precision is therefore of great relevance in developing and improving solid-state battery cells. This remains an experimental challenge and, with this work, we aim to advance the detailed study of well separated electrode processes in SSBs.

Conventional 2E measurements always show contributions from both anode and cathode, that hardly can be separated without additional analytical efforts.[13] Impedance spectroscopy suffers from this limitation as well. Processes occurring at the electrodes are often overlapping in the low-frequency region of the impedance spectra. Separation of the two electrode contributions might in some cases be possible by combination of results from different cells and systematic electrode variation, however, this is time-consuming and necessarily not unequivocal or even not possible. 3E cells are able to overcome these issues, and it is needless to add that 3E cells are well established in the field of electrochemistry using liquid electrolytes.[14–19] Interestingly, even though reference electrodes are quite well established in liquid-based cells, they are rarely used, mainly because it increases the amount of work to build one cell.[20–23] Clearly, the solid state provides serious difficulties in constructing and positioning reference electrodes properly close to the electrode interface, as easily achieved in liquid electrolytes with e.g. a Haber-Luggin capillary. However, separation of the working and counter electrode half-cell potentials is also possible, even if it is experimentally more challenging.[24–26]

Due to these challenges, 3E setups are rarely reported in the field of solid-state electrochemistry and not well established,[27–30] and even in the field of polymer electrolytes reports including the use of reference electrodes (RE) are scarce.[31] The major issue is always the proper placement of the reference electrode within the solid electrolyte close the working electrode, as well as miniaturization that leaves the cell mostly unchanged. An additional problem arises, when the solid electrolyte cells require thermal treatment at elevated temperatures before application which easily leads to degradation of the RE inside the electrolyte. Clearly, while the amount of information would vastly increase from building 3E cells it is often considered as a bad trade-off and not worth the extra effort.

Up to now, 3E setups for solid-state Li-ion cells have rarely been reported and we are aware of only two examples and in only of these impedance data were shown.[28,30] Reported 3E setups can be distinguished either as pseudo-reference electrochemical double cells where an electrode is placed on top of a normal cell separated by an SE layer[29] or cells in which a third (reference) electrode is placed in the middle between anode and cathode.[28,30] Setups with the RE in the middle between anode and cathode rely on different approaches. Cells with indium strips and $Li_4Ti_5O_{12}/Li_7Ti_5O_{12}$ covered metal meshes have been reported.[28,30] Cells with a point-like gold contact using liquid electrolyte lithium-ion batteries have also been reported.[20] Figure 1 shows a comparison of the different geometries used in the literature and in this work.

In this work we present and prove the function of a miniaturized RE that is easily implemented in typical cell setups and that is not changing the cell geometry significantly while well separating the electrode potentials. This allows direct comparison to existing 2E setups. We use In/InLi as anode, Li_6PS_5Cl as solid electrolyte both in the separator and $Li_{1-x}Ni_aCo_bMn_{1-a-b}O_2$ (NCM)/Li_6PS_5Cl composite cathodes. The RE used herein is formed by lithiating a thin gold-plated tungsten wire with 10 μm diameter. As the surface of the tungsten wire is completely covered with gold it will be referred to as "gold-wire" as the interface chemistry toward the cell is completely determined by the gold coating, while the tungsten core only provides mechanical stability.

[z]E-mail: juergen.janek@pc.jlug.de

Journal of The Electrochemical Society, 2023 170 040519

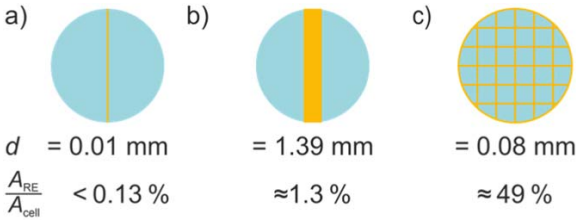

Figure 1. Simplified cross section geometries of 3E setups found in literature. (a) This work. The (gold) microwire μ-RE covers less than 0.13% of the cell's cross-section leading to a negligible perturbation of the current flow between cathode and anode. (b) Arrangement reported by Chang et al.;[30] the indium strip covers about 1.26% of the cross-sectional area of the cell. (c) Arrangement by Ikezawa et al.;[28] the nickel net has an open area of about 90%. The net is covered with an LTO slurry leading to an area coverage of about 49% (estimated from a picture published by the authors of the electrode by automated pixel counting). Note that the thicknesses of the REs and the cell diameters are not shown to scale.

To highlight the micro-reference electrode (μ-RE) approach, we compare different RE constructions. A top-sided pseudo-RE as shown in Fig. 3b) does not allow impedance measurements which is why a μ-RE setup is shown as well. The influence of the shape of the wire on the impedance results is emphasized and guidelines for setting up a successful RE measurement will be given below.

We demonstrate the use of the μ-RE in both cycling experiments as well as in impedance analysis. Post-mortem analysis with time-of-flight secondary ion mass spectrometry (ToF-SIMS) and focused-ion-beam scanning electron microscopy (FIB-SEM) is shown as well. Significant errors are made when performing rate tests without the use of a proper 3E setup.

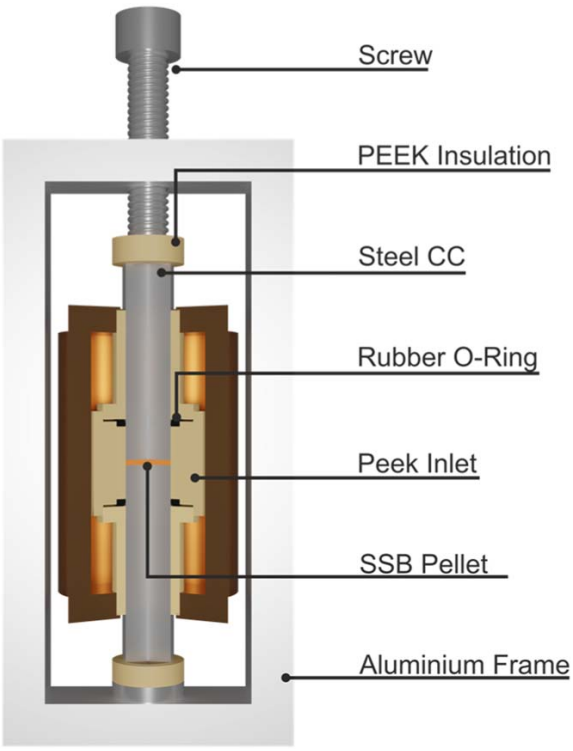

Figure 2. SSB cell in a brass housing and an aluminium frame for pressure-controlled electrochemical measurements.

Experimental

Materials.—For the assembly of all-solid-state batteries the crystalline SE Li_6PS_5Cl with an ionic conductivity of 1.4 mS/cm (NEI Corp., NJ, USA) was used as received and stored in an argon filled glovebox with impurity levels of $p(O_2)/p < 1.0$ ppm and $p(H_2O)/p < 1.0$ ppm. Indium foil (100 μm, chemPUR, Germany) and gold-plated tungsten wire with 10 μm diameter and 3–5 wt% gold coverage (Goodfellow, Germany; called gold wire from here on for simplicity) were dried in vacuum at 60 °C prior to use. Lithium (abcr GmbH, Germany) was used as received and stored in an argon filled glovebox with the same impurity levels as well. Lithium foil was prepared by taking small pieces (~5 mg) of lithium and pressing it between pouch bag foil resulting in ~200 μm thick foil. NCM ($LiNi_{0.85}Co_{0.10}Mn_{0.05}O_2$) was provided by BASF SE and dried in vacuum at 250 °C for 12 h prior to use.

Gold wire μ-reference electrode.—The gold-wire μ-REs were preassembled to facilitate subsequent assembly of the solid-state cell. A small piece of gold wire was taken and attached to one side of a polyether ether ketone (PEEK) inlet with Kapton tape as shown in Fig. S1. The gold wire was spanned across the PEEK inlet and then attached to the other side of the PEEK inlet with another piece of Kapton tape. The gold wire was connected to the brass housing therefore providing a connection the outside circuitry.

Cell-assembly.— *Two-electrode cell.*—2E cells were prepared using the sequence In/InLi | Li_6PS_5Cl | cathode with varying cathodes. First, a 60 mg SE layer was prepressed at 382 MPa in a PEEK inlet with an inner diameter of 10 mm. 12 mg of cathode composite were added and distributed homogeneously over the prepressed SE layer. The composites were prepared by hand mixing the components in an agate mortar for 15 min. The pellet was then pressed at 382 MPa for 45 s. After pressing the In/InLi anode was added by first putting indium foil (9 mm diameter, 100 μm thickness), then lithium foil (4 mm diameter, ~100 μm) and lastly steel foil (10 mm diameter) on top of the pressed SE layer. During cycling the cell was held at a pressure of 63.7 MPa using an outer aluminum frame as shown in Fig. 2.

Top-sided double electrochemical cell.—For the assembly of the top-sided RE (TSRE) a 2E cell was prepared as described above. After this first step the cell was opened and the current collector was replaced by a hollow cylinder with PEEK insulation in the middle as shown in Fig. 3b. In this hollow cylinder 10 mg of SE were put in and were carefully pressed with a steel stamp. The stamp was removed and indium foil with 3 mm diameter was placed inside and the stamp was put in again.

Three-electrode cell.—For the assembly of full cells with a μ-RE (3E cells), the same materials as in the 2E setup were used. Additionally, a μ-RE was used. First, a SE layer (100 mg) was prepressed at around 40 MPa in a PEEK inlet with an inner diameter of 10 mm. A small steel plate was placed on top of the PEEK inlet to create a flat surface on the upper edge of the inlet. The second half of the PEEK inlet with the gold wire was attached, and another 100 mg of SE were added. After prepressing at around 40 MPa again, 12 mg of cathode composite were added. The pellet was then pressed uniaxially at 374 MPa for 45 s. After pressing the In/InLi anode was added as described above and the cell was held at a pressure of 63.7 MPa during the experiments using the same outer aluminum frame as for 2E cells shown in Fig. 2.

Formation of the reference electrode by lithiation.—The gold wire was lithiated in situ using the In/InLi anode as counter electrode making use of the excess lithium and the stable potential in the In/InLi anode. A current of 1 μA ($A = 3.14 \cdot 10^{-3}$ cm^2) was applied for 8 h leading to lithiation of the gold wire and formation of the μ-RE. Assuming 100% coulomb efficiency the charge transported during

Journal of The Electrochemical Society, 2023 170 040519

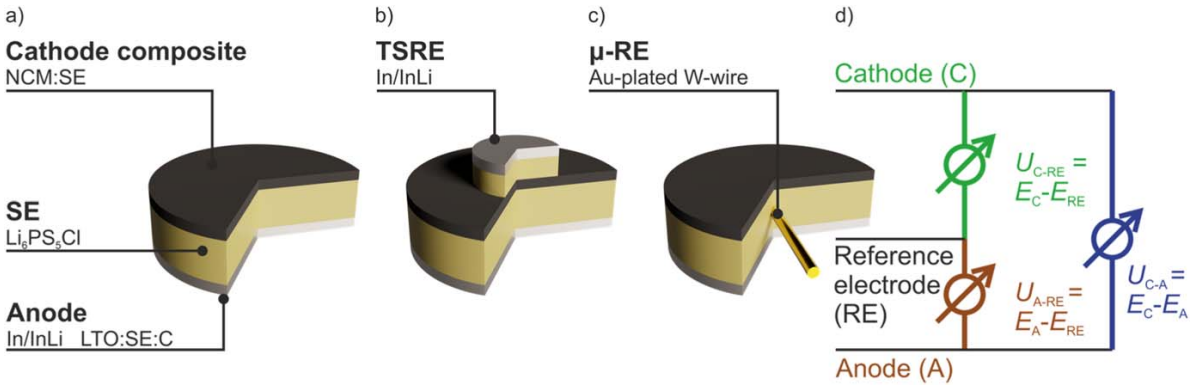

Figure 3. Geometry and description of the voltages and connections of the three different cell setups used in this work. (a) Conventional 2E pellet-type setup with three layers, i.e. anode ($d \approx 120$ μm), SE separator ($d \approx 400$ μm) and composite cathode ($d \approx 60$ μm). (b) 3E setup based on the geometry of the 2E setup using a top-sided reference electrode out of In/InLi ($d \approx 120$ μm) separated by a SE layer ($d \approx 200$ μm). (C) 3E setup based on the 2E setup with a μ-RE in the middle of the separator. The geometry is essentially unchanged compared to the 2E setup. (D) Cell voltages U and potentials E used in this work. All potentials are given vs $E(Li^+/Li) = 0$ V if not stated otherwise. Note that the color code in this graph applies to all electrochemical data shown in this work.

this plating progress corresponds to 4.3 μm lithium metal on top of the $AuLi_3$ layer which contains a lithium equivalent of $Q_{AuLi_3} = 0.43$ μAh.

Impedance measurements.—Impedances of 2E and 3E cells with μ-RE were both measured using a VMP-300 from BioLogic (France) after resting for 3 h after each charging or discharging step. For the 2E cells full cell impedances were recorded, for the 3E μ-RE cells cathode and anode impedances were recorded independently. Impedances were recorded from 300 kHz to 100 mHz with 15 points per frequency decade and an excitation voltage of 10 mV relative to the previously measured open circuit voltage (OCV). At each frequency step a waiting time of 2 sine wave periods was implemented to avoid artefacts of transient behavior. After that, the impedance was measured and averaged for 6 sine wave periods.

Cycling experiments.—3E cells were cycled with constant current between an upper cut-off potential of the cathode of 4.3 V and a lower cut-off potential of 2.5 V vs Li^+/Li at various C-rates where 1 C corresponds to 190 mA/g_{NCM} unless stated otherwise. 2E cells using In/InLi as anode were cycled accordingly with an upper cut-off voltage of 3.7 V and a lower cut-off voltage of 1.8 V. 2E cells using $Li_4Ti_5O_{12}$ (LTO) as anode material were cycled with an upper cut-off voltage of 2.75 V and a lower cut-off voltage of 0.95 V.

SEM and FIB-SEM measurements.—The pellet containing the μ-RE was attached to the sample holder with non-conductive tape. The pellet was broken horizontally in the middle revealing the μ-RE. All samples were directly transferred without contact to air with a LEICA EM VCT500 transfer system. FIB craters were created with a 30 kV Xe plasma FIB at a current of 1 μA with subsequent polishing at 30 kV and 100 nA using a XEIA3 Triglav from Tescan. FIB-scanning electron microscopy (SEM) measurements were performed on a XEIA3 Triglav from Tescan. SEM images were recorded at 3 kV with a current of 290 pA using a secondary electron detector and a backscattered electron (BSE) detector.

SEM measurements were performed on a Zeiss Merlin Gemini. Electron images were recorded using a secondary electron or BSE detector. Energy dispersive X-ray spectroscopy (EDS) measurements were performed on a XMax 50 from Oxford instruments with an electron current of 3 nA and an acceleration voltage of 5 kV.

ToF-SIMS measurements.—Time of flight secondary ion mass spectroscopy (TOF-SIMS) measurements were performed on a TOF-SIMS 5–100 by IonTOF GmbH, Germany, which is equipped with a 25 keV Bi cluster primary ion gun for SIMS analysis and a dual-source column for depth-profiling with up to 2 keV using O_2^+ or Cs^+. Additionally, craters were milled with a focused-ion beam using monoatomic gallium at 30 keV. The pellets used for FIB-SEM measurements were transferred to the ToF-SIMS. The sample surface was flooded with low-energy electrons for charge compensation. Measurements were performed in negative ion mode with Bi_3^+ (25 keV) and a cycle time of 60 μs.

To investigate the μ-RE in the SE separator a 45° FIB crater sidewall was used. The crater (120 × 80 μm^2) was milled with 512 × 512 pixels. The crater was created using a 700 μm aperture and a dwell time of 200 ms per pixel with a current of 16–17 nA. The analysis was performed in fast imaging mode with a primary ion current of 0.2 pA. The region of interest was set such that only the sidewall was analyzed. Prior to the analyses, the crater sidewall was cleaned as described in previous work.[7,12,32] The analysis was performed with a raster size of 1024 × 1024 pixels with 1 shot per pixel and 50 frames corresponding a theoretical resolution of 122 nm. This was the best resolution in this case as the topography had a negative effect on the resolution.

The data were analyzed with the software SurfaceLab 7.2 (IONTOF GmbH, Germany). Secondary ion images were all normalized to the total ion signal in order to minimize topographic effects.

Results and Discussion

Two-electrode cells.—2E cells were characterized by rate tests and impedance analysis. Investigation of a single electrode in a 2E setup, in this study a composite cathode, is critically dependent on the counter electrode, i.e. the anode in this study. However, the same principles apply of course to the investigation of anodes with cathodes as the counter electrode and symmetric setups as well. Figure 4 shows a rate test performed on a 2E cell using NCM/Li_6PS_5Cl as cathode and LTO/Li_6PS_5Cl as anode. The cell was cycled at currents from 0.1 C to 1.0 C to an upper cut-off voltage of 2.75 V and a lower cut-off voltage of 0.9 V corresponding to 4.3 V vs Li^+/Li and 2.45 V vs Li^+/Li, respectively. At both the upper and lower cut-off voltage the influence of the anode is *a priori* unknown. Ideally, the overpotential of the anode is low and therefore not influencing the analysis of the cathode characteristics. This assumption, however, is usually neither checked nor confirmed leaving potential problems of the anode undetected. We like to add that impedance data often do not allow unequivocal deconvolution of cathode and anode partial impedances.

Additionally, when measuring the impedance of a typical 2E cell consisting of a $NCM851005/Li_6PS_5Cl$ composite cathode and an In/

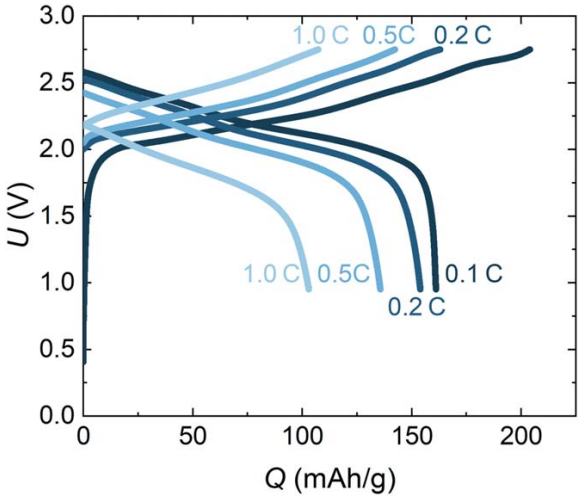

Figure 4. Rate test performed with a conventional 2E setup at $\theta = 25$ °C. A strong decrease in capacity from 0.1 C to 1.0 C is observed. From these data alone it is not clear whether this capacity decrease is mainly due to the kinetics of the cathode or the anode.

InLi anode problems arise during analysis of the data. The results are shown in Fig. 5. Due to the overlap of the cathode and anode contributions fitting the data is ambiguous. Both sets of parameters fit the experimental data equally well using the same equivalent circuit. The exact fit values and residuals of these datasets are given in Table SI.

Cells with top-sided pseudo-reference electrode.—Cells with the TSRE were cycled at 0.1 C and the respective charge and discharge curves of a cell are shown in Fig. 6. The charge and discharge profiles of the cell show sharp peaks and dips throughout the whole charge and discharge. This profile clearly indicates that the cell was not cycling properly. However, it is not clear whether the cathode or the anode causes this behavior. The setup with the TSRE allows separating the cell voltage in a voltage of the anode and a voltage of the cathode vs the TSRE, respectively as shown in Fig. S6.

The anode voltage profile shows no distinct features with a more or less constant overvoltage of about 40 mV during charge. During discharge the overvoltage is rising constantly, probably due to worse contact as the lithium is depleted from the In/InLi anode. This effect comes with no surprise as the electrode itself is shrinking during depletion of Li. The cathode shows the same features that are also visible in the full cell voltage profile. Therefore, the problem of this cell clearly arises from the cathode, as the working electrode is not only connected to the current collector but also connected to the pseudo-reference electrode which is located in the middle. Usually, a constant pressure is applied to a cell during cycling, however, this setup does not allow applying high pressure as the steel stamp of the pseudo-reference electrode in the middle needs to be longer than the outer steel stamp to allow contacting it to the instrument. Therefore, little to no pressure is applied to the cell during cycling leading to a poor performance.

This setup is a good demonstration on how to use 3E setups for failure diagnosis in cells. Unfortunately, comparison to already existing systems using standard 2E cells are difficult because the outer parameters such as pressure during cycling and other electrochemical testing are changed. A setup where these parameters can stay unchanged is therefore preferred.

Three-electrode cells.— *Lithiation of the gold wire μ-reference electrode (μ-RE).*—To enable direct comparison to conventional 2E cells a 3E setup is introduced that leaves the geometry of the 2E cell

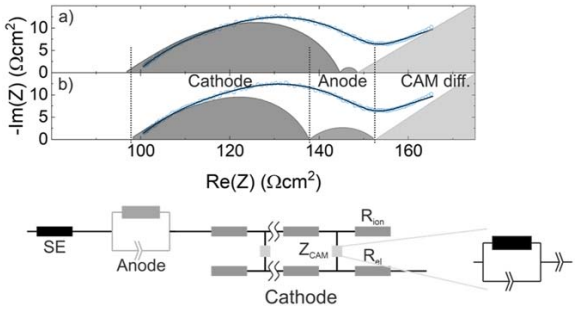

Figure 5. Impedance data analysis for 2E cells showing the ambiguity of data analysis due to the overlap of anode and cathode contributions. Both fits in (a) and (b) match the experimental data well with the same equivalent circuit used. Deciding which fit represents the system more accurately requires additional experiments. The detailed fit parameters and a separated fit for the anode are given in Table SI and Fig. S7 in the SI.

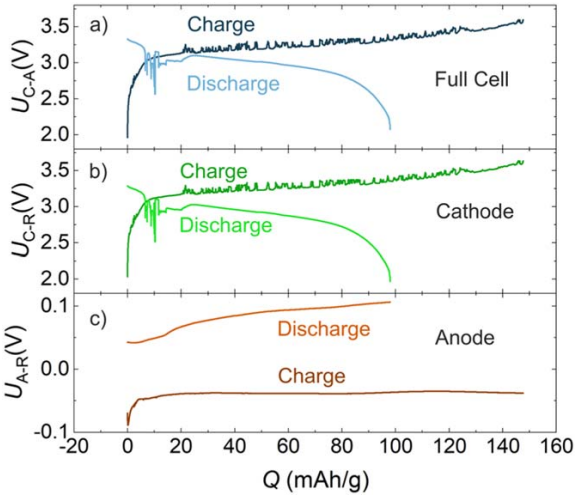

Figure 6. Charge and discharge curves of a cell with TSRE. (a) Full cell voltage vs capacity. Both the charge and discharge show sharp voltage fluctuations. The cell is clearly not performing as intended. (b) Cathode vs TSRE. The same voltage rises and drops are visible here indicating a problem on the cathode side. (c) Flat charge and discharge curves are present in the anode vs TSRE pseudo-reference indicating no problems on the anode side as this cycling profile shows no voltage fluctuations.

essentially unchanged by introducing a gold wire μ-RE. The unlithiated μ-RE exhibits an unstable potential of around 1.73 V–2.13 V vs Li^+/Li (1.11 V–1.50 V vs In/InLi) after assembly, as expected. Lithiation is required to form a proper RE with stable and thermodynamically defined electrode potential. For gold and lithium two electrochemically stable intermetallic phases AuLi and $AuLi_3$ are known, exhibiting a potential of $E(AuLi/AuLi_3) = 134$ mV and $E(Au/AuLi) = 215$ mV vs Li^+/Li in OCV, respectively.[20,33–35] The first plateau, corresponding to the Au/AuLi phase equilibrium is barely visible when using a gold wire with a tungsten core with a diameter of 10 μm, as the potential almost immediately drops further down to the second plateau corresponding to the $AuLi/AuLi_3$ equilibrium (see Fig. 7). When we used a thicker wire with 100 μm diameter the lithium plating process is better resolved. Due to the larger amount of Li required to lithiate Au to AuLi and $AuLi_3$ it takes longer and the voltage plateaus become better visible (see Fig. 7). After complete lithiation of gold to $AuLi_3$, lithium metal is plated on the μ-RE leading to another plateau of 0 V vs Li^+/Li. Depending on the current and

Journal of The Electrochemical Society, 2023 170 040519

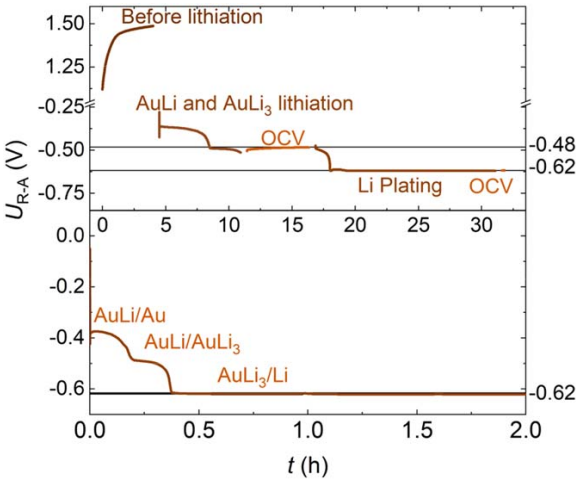

Figure 7. Top - Voltage measurement during lithiation of a gold-plated tungsten wire in a solid-state cell, measured between the μ-RE and the In/InLi anode. The plateaus of the Au/AuLi and Au/$AuLi_3$ two-phase systems are well visible. As shown in the top graph it is also possible to stop the lithiation at the $AuLi_3$ potential plateau and observe a stable OCV. As the required amount of lithium is quite small even minor side reactions can lead to an unstable potential of the RE. Therefore, lithium metal is plated on the μ-RE, as can be seen by the potential in both graphs leading to a stable potential of –618 mV vs In/InLi. Bottom—faster lithiation showing the same plateaus as observed on the top graph.

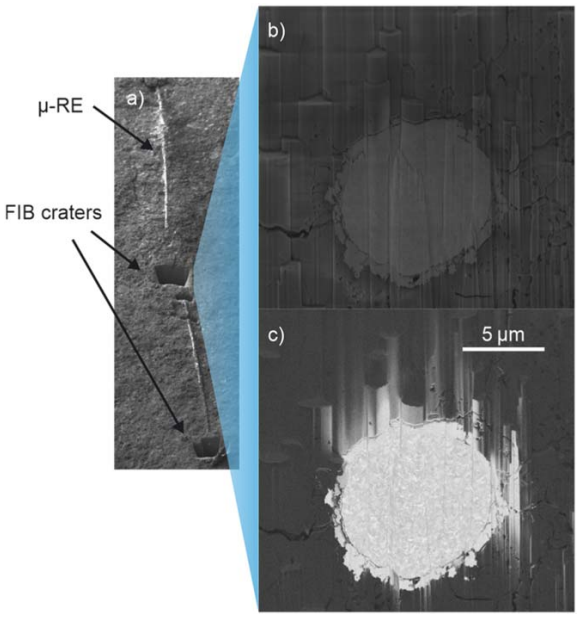

Figure 8. (a) SEM images of the gold-wire lying on top of the solid electrolyte after breaking the pellet in halves. Both the morphology of the wire itself and the FIB-craters are visible. (b) Secondary electron image of the lithiated gold-wire embedded in Li_6PS_5Cl. (c) Backscattered electron image of the lithiated μ-RE. The different materials are distinguishable with the tungsten core in the middle surrounded by the $AuLi_3$ and the lithium phase. Delamination is visible in some places. This does not pose a problem as the SE holds the phases tightly in place.

plating time, lithium layers with different thicknesses can be plated on the μ-RE. While thin layers of lithium are advantageous because of their small size, it is possible that the lithium on the wire reacts completely with the SE which then results in a different potential of the RE. Plating thick layers of lithium on the μ-RE leads to a stable potential over a prolonged time but increases the size of the reference electrode, thus decreasing the quality of the measured impedance spectra. It was therefore necessary to find a compromise. Here, a mean thickness of 4 μm was used for the μ-RE, leading to a stable potential of 0 V vs Li^+/Li for at least 8 days. It should be noted that it is in principle also possible to use the Au/AuLi and AuLi/$AuLi_3$ potential plateaus as reference as well, which would result in very thin and morphologically simple reference electrodes. The potentials of these plateaus, however, still lead to reductive degradation of the solid electrolyte around it, which led to quick depletion of lithium in the wire and therefore an unstable potential over a prolonged period of time.

Another way of providing a stable potential would be the use of an In/InLi reference electrode. In/InLi would have the advantage of not reducing thiophosphate SEs. However, indium wires that are thin enough for practical use in solid-state cells are currently not available commercially. Alternatively, indium would be needed to be plated on a tungsten wire, analogous to the current approach. As indium is easier corroded, we preferred to operate with gold. We like to add that any SEI formation on the μ-RE will not influence the potential of the RE, as long as the SEI is primarily ion-conducting.

ToF-SIMS and FIB-SEM analysis of the μ-RE.—FIB-SEM and ToF-SIMS analyses were carried out in order to investigate the lithiated μ-RE inside the separator. The cell pellet was broken in half in the middle and the morphology of the gold wire was then well visible in the SEM (Fig. 8). A few cracks are visible in the Li_6PS_5Cl around the wire. Otherwise the SEM images show a good contact of the μ-RE to the SE. The tungsten core can be well distinguished from the outer $AuLi_3$/Li layer (Fig. 9). The gold layer seems to have cracked and delaminated from the tungsten core at some points. This could be due to the volume expansion of 269% upon lithiation to $AuLi_3$.[36,37] However, the SE is preventing complete delamination and contact to the $AuLi_3$ phase is still maintained. As the SEM images were recorded post-mortem and after FIB-cutting the metallic lithium cannot anymore be detected. The original thickness of the plated lithium metal is expected to be 5 μm.

Stability of the gold wire μ-reference electrode.—The stability of the lithiated μ-RE was controlled between the various experiments by measuring the voltage $U_{RE\text{-}A}$ between the μ-RE and the In/InLi anode. The In/InLi anode was assembled with the appropriate lithium/indium ratio and therefore exhibited a stable potential of 618 mV vs Li^+/Li. Long-term cycling experiments show that the μ-RE was typically stable for about 8 days. This time span was enough to do most electrochemical testing. For long-term cycling experiments two strategies to keep the μ-RE stable long enough were applied. Either the μ-RE was "refreshed" by plating additional lithium before starting the cycling experiment, thus providing a stable potential for a longer period of time. Or the μ-RE was checked regularly (against the In/InLi anode) and it was quickly relithiated ("refreshed") when needed. We note that long time experiments could thus be run without major issues.

Impedance measurements.—Validation: To validate the quality of the impedance spectra we compared measurements of 2E cells with results from 3E cells. 3E cells yield two independent spectra, one spectrum for the anode and one spectrum for the cathode—both measured against the same μ-RE. The sum of these spectra yields, in theory, the impedance spectrum of the full cell as measured in a conventional 2E cell, see formula (1).

$$Z(3E)_{C-A} = Z(3E)_{C-R} + Z(3E)_{R-A} \quad [1]$$

In a real experiment, however, these two datasets will never perfectly agree. Deviations may arise from natural noise,

Journal of The Electrochemical Society, 2023 **170** 040519

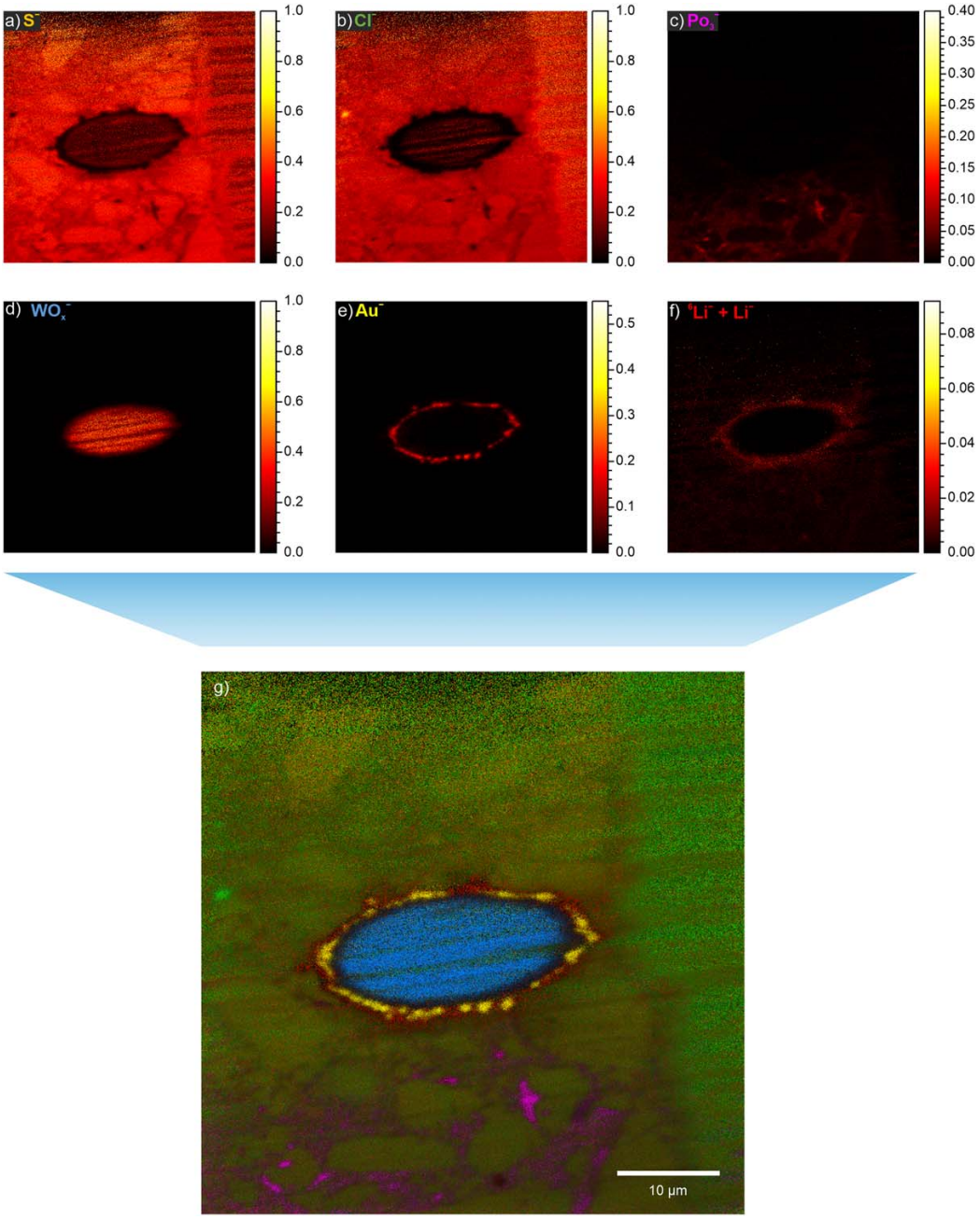

Figure 9. ToF-SIMS images of the lithiated μ-RE embedded in the solid electrolyte matrix (cross section after FIB cut). All signals are normalized to the total ion signal. (a), (b) S^- and Cl^- mass signals corresponding to Li_6PS_5Cl. The homogeneous distribution and the grain structure of the material are visible. (c) The PO_3^- signal is assigned to oxidative degradation products of Li_6PS_5Cl. (d) The WO_x^- signal is assigned to W metal in the μ-RE core. The dimension of the wire is nicely visible. (e) The Au^- signal is assigned to gold or gold alloys. The gold layer is distributed around the tungsten but the layer appears to be not fully dense. (f) $^6Li^-$ and $^7Li^-$ signals are assigned to lithium rich degradation products of Li_6PS_5Cl. These species are present around the tungsten as well. The thickness is on the order of magnitude that is expected. (g) Overlay of the signals above. We like to note that the apparent oval shape of the cylindrical wire is caused by the 45° angle of view on the wire.

differences in external factors such as temperature or pressure. These differences can only be minimized. Issues with the cell setups can result in larger deviations and can be investigated by plotting the residuals e as defined in formula (2) of the 3E and the 2E measurement.

$$e = Z(3E)_{C-R} + Z(3E)_{R-A} - Z(2E)_{C-A} \quad [2]$$

As shown in Fig. 10, the 2-electrode impedance of a cell with a NCM851005/Li_6PS_5Cl composite cathode and an In/InLi anode and the sum of the two individual impedances of cathode and anode

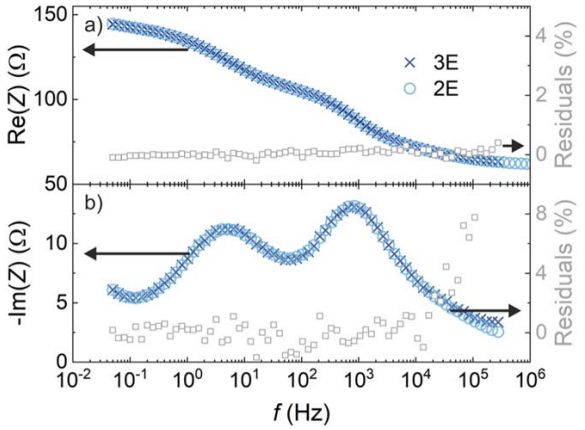

Figure 10. Comparison of impedance data obtained from a 2E cell and a 3E cell. (a) Real part of the impedance of the 2E cell in comparison to the sum of the individual anode and cathode impedances obtained in a 3E cell. Even at high frequencies the 2E and 3E results are almost identical. The residuals are shown as grey squares. (b) Imaginary part of the impedances with similar color code. Even at high frequencies the 2E and 3E results are almost identical. At high frequencies above 100 kHz slight deviations are visible but still under 1% in the real part.

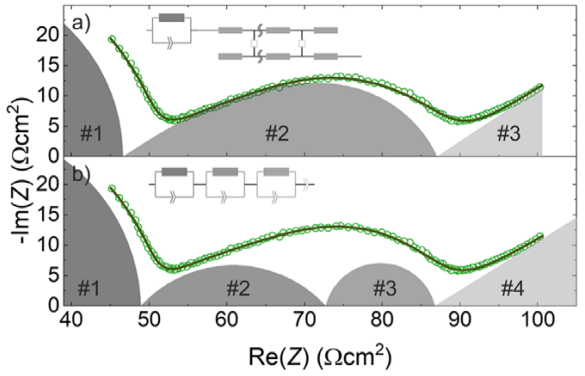

Figure 11. Separate cathode impedance in a In/InLi | Li_6PS_5Cl | NCM851005/Li_6PS_5Cl cell in 3E setup. Only the composite cathode and a part of the separator form the impedance spectrum. (a) Fit with a TLM, that describes the experimental data very well. The first dark grey semicircle (#1) is caused by the SE separator. The middle grey contribution (#2) is caused by the composite cathode. The light grey contribution (#3) is due to lithium diffusion in the NCM851005. (b) Fit with a series of 3 R-CPE elements and a CPE. The dark grey semicircle (#1) is again caused by the SE separator. The two middle grey semicircles (#2 and #3) are caused by the composite cathode. One of the resulting semicircles shown in grey (#2) is very depressed, indicating that the equivalent is badly suited for this data. The light grey contribution (#4) is due to lithium diffusion in the NCM851005.

(measured each vs the μ-RE) yield almost exactly the same results. The residuals are below 1% for the real part and below 10% for the imaginary part demonstrating very good agreement between the two measurements and validating the results of the reference electrode concept and construction. We like to note that the residuals for the imaginary part only get higher than about 1%, when the frequency increases beyond 10 kHz. Thus, the frequency range that is typically monitoring electrode impedances can be very well used for electrode studies relative to the μ-RE.

Impedance fitting: as often noted, contributions from anode and cathode may strongly overlap. This leads to difficulties in fitting and analyzing the data as the contributions cannot be separated unequivocally. Separating the anode and cathode contributions through the use of our μ-RE facilitates the fitting and analysis of electrode impedances, as the complexity gets reduced drastically.

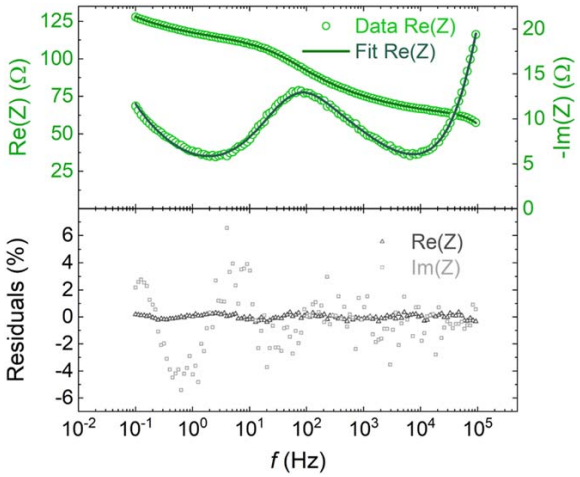

Figure 12. Fitted impedance data of an individual NCM851005/Li_6PS_5Cl composite cathode impedance obtained in a 3E cell, relative to a μ-RE. Top: Bode plot; the symbols show the measured data; the line shows the respective fit. Bottom: Relative residuals for this dataset for the real and imaginary part. Nyquist plot of the fitted impedance with the transmission line model.

In order to demonstrate the ability to fit physically meaningful models to separate impedance spectra of composite cathodes, a transmission-line model (TLM) is chosen. This type of model has previously been used in the literature to describe porous electrodes.[38–40] In solid-state battery cells the electrodes are porous as well as they consist of active material with SE in the pores (or vice versa). The model used here describes the cathode composite with two separate conduction pathways, one electronic pathway provided by the active material and one ionic pathway, provided by the SE. These two pathways are connected by the charge transfer (CT) between these materials and the diffusion of lithium in the active material. The CT is described by a parallel R-CPE element where CPE is a constant phase element and a constant phase element describing the diffusion of Li-ions in the active material. More correctly, a finite Warburg element needs to be used here, however, only a part of the diffusion contribution is visible in the impedance spectra due to chosen frequency range. Effectively, it is not possible to fit the finite Warburg element reliably as lower frequency data would be needed. The advantage of using a TLM over the conventional approach of using R-CPE elements in series is that the TLM directly yields physically meaningful parameters such as CT resistance and SE conductivity. These parameters can be found in Table S1 in the SI. Figure 11 shows the comparison of the fits using a TLM as model (top graph (a)) and using R-CPE elements in series as a model (bottom graph (b)). The serial R-CPE model shows a very depressed semicircle for one of the elements. This is usually a sign that the model is not physically meaningful as very depressed semicircles cannot be explained properly. Figure 12 shows a fit to the impedance data of the NCM851005/Li_6PS_5Cl composite cathode using the TLM. The fit describes the measured data very well, and the resulting fit parameters are physically reasonable. The (effective) specific ionic conductivity in the composite results as $\sigma_{ion}(\text{eff}) = 0.145$ mS/cm (the ionic conductivity of bulk Li_6PS_5Cl is 1.4 mS/cm) whereas the charge-transfer resistance between the SE and the active material results as $R_{CT} = 17.8\ \Omega\text{cm}^2$. These values are calculated as described by Braun et al.[38]

Rate tests.—Rate tests are commonly used to investigate the response of a battery cell under different current densities to evaluate

Journal of The Electrochemical Society, 2023 170 040519

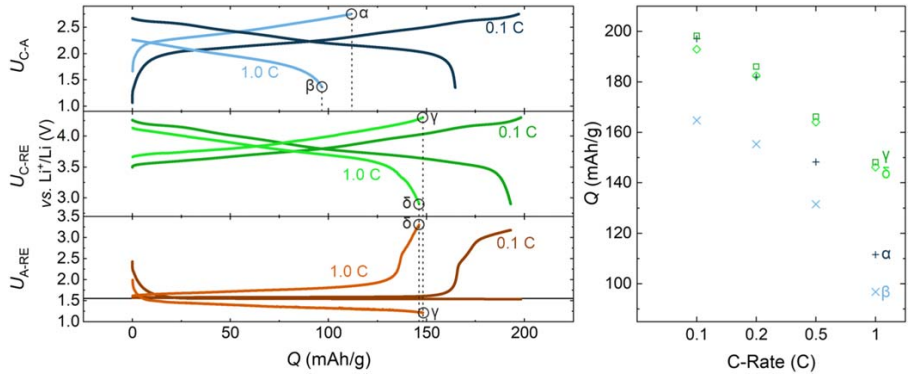

Figure 13. Rate test performed with NCM851005 | Li_6PS_5Cl and $Li_4Ti_5O_{12}$. (a) The cycling results for the 2E cell (top) show massive decrease in capacity for high currents whereas the decrease in capacity is drastically reduced for the 3E cell where only the cathode side (middle) is evaluated for the cut-off of the cycling. The simultaneously recorded data for the anode (bottom) explains why the capacity decrease is so severe for the 2E cell. (b) Charge and discharge capacities for the 2E and 3E cell at various currents.

the potential power density. When charging and discharging at higher currents the overpotentials at anode and cathode rise, leading to an earlier cut-off and loss in performance.

Usually, a full cell is used and the respective cell is cycled under different current loads. Often, one electrode is of particular interest for the rate test. For example, when investigating different cathode active materials the same anode is used, but its kinetics is not of further interest. If the overpotential of the anode is non-negligible the rate performance of the cathode will be underestimated in a simple 2E setup. In extreme cases the differences in the cathode performance will be barely recognizable and the rate performance may even be dominated by the anode.

To highlight this, a 3E cell with LTO as anode material and NCM851005/Li_6PS_5Cl as cathode composite with a μ-RE was constructed. The cell was charged and discharged between 2.9 V and 4.3 V vs Li^+/Li at 0.1 C, 0.2 C, 0.5 C, 1.0 C (1.0 C = 1.44 mA), respectively, for 2 cycles each. The 3E setup yields three voltages. Firstly, $U_{C\text{-}RE}$ describing the voltage of the cathode vs the RE; secondly, $U_{A\text{-}RE}$ being the voltage of the anode vs the RE and thirdly $U_{C\text{-}A}$ which is the voltage of the full cell and which is $U_{C\text{-}A} = U_{C\text{-}RE} - U_{A\text{-}RE}$.

The anode used here was a LTO/Li_6PS_5Cl/Carbon (C65) composite exhibiting a potential of 1.55 V vs Li^+/Li in OCV. The respective cut-off voltages are 1.35 V and 2.9 V when measuring in a 2E setup.

$$U_{C\text{-}A} = E_C - E_A \quad [3]$$

$$E_C = E_C^0 + \eta_C \quad [4]$$

$$E_A = E_A^0 + \eta_A \quad [5]$$

Equations 3–5 show that the measured voltage of a full cell always contains the overpotential of the anode (here: In/InLi or LTO).

Figure 13 shows the resulting charge and discharge curves for 0.1 C and 1.0 C. Data for other currents can be found in Fig. S3 in the SI. At low currents (0.1 C) the charge capacities of the 2E setup are not changed significantly compared to the 3E setup with 198 mAh g^{-1} and 197 mAh g^{-1}, respectively. The discharge capacities, however, show larger differences with 193 mAh g^{-1}, and 165 mAh g^{-1}, respectively. The 2E data gives no clear-cut information as to why the discharge capacity is so much lower compared to the 3E setup while the charge capacity is virtually the same. Looking at the 3E data on the other hand gives additional information. When looking at the data for the anode, it can be seen that during charge the potential is deviating only slightly from 1.55 V which is the OCV of the anode. Therefore, very small overpotentials are observed and the anode is not influencing the performance of the cathode significantly during charge. During the discharge, the voltage is at first also only deviating very little from 1.55 V indicating small overpotentials. At around 160 mAh g^{-1}, however, the voltage of the anode $U_{A\text{-}RE}$ is rising suddenly to as high as 3.2 V. This is lowering the full cell voltage $U_{C\text{-}A}$ drastically leading to an earlier cut-off and hence to lower capacities. This sudden rise of the anode voltage $U_{A\text{-}RE}$ is due to the anode active material $(Li_4Ti_5O_{12})_x/(Li_7Ti_5O_{12})_y$ having a stable potential of 1.55 V vs Li^+/Li as long as both the lithiated and delithiated phase are present in the electrode. During discharge the anode is delithiated and as soon as the $Li_7Ti_5O_{12}$ phase is used up a steep increase in the anode potential is observed. Interestingly this increase is happening early indicating side reactions that are consuming Li.

At higher current densities the charge capacities of the 2E (112 mAh g^{-1}) cell are significantly lower compared to the 3E setup (148 mAh g^{-1}). Again, the 3E data of the anode gives information as to why the capacities are so much lower. At these currents, high overpotentials up to 300 mV can be observed at the anode side leading to an earlier cut-off of the 2E cell. The discharge capacities are much lower as well for the 2E setup (96.8 mAh g^{-1}) compared to the 3E setup (146 mAh g^{-1}). The reason for this is the same as for low currents, but this time high overpotentials are observed from the beginning on leading to an even higher decrease in capacity.

The reason for the deviation from 1.55 V on the anode during discharge can be attributed to lithium deficiency on the anode side. LTO is delithiated when assembling the cell and no lithium excess is present. During charge the LTO is lithiated forming $(Li_4Ti_5O_{12})_x/(Li_7Ti_5O_{12})_{1-x}$ with a stable potential of 1.55 V vs Li^+/Li. During discharge the anode is delithiated again and at some point the two-phase region $(Li_4Ti_5O_{12})_x/(Li_7Ti_5O_{12})_{1-x}$ is left leading to a sudden increase in the anode potential.

Conclusions

We have presented a versatile, easy to adopt and straightforward technique to implement µ-sized wire-type reference electrodes into solid-state battery cells. The proper function of the μ-RE is firstly demonstrated by impedance analysis of 2E and 3E cells. The 3E cells allow separation of the individual anode and cathode impedance contributions. Their combination agrees perfectly with results from 2E cells. Single electrode impedance spectra are recorded and allow precise analysis of the electrode kinetics. The physical separation of the anode and cathode impedances by our μ-RE is highly reliable and offers precise electrode data.

Secondly, the function and use of the μ-RE was demonstrated in rate capability tests. High overpotentials arising from the anode can overshadow effects from the cathode. This was demonstrated by

using a LTO | Li_6PS_5Cl | NCM 3E cell that allows measuring the true potential of the cathode. The 3E setup shows that the true rate capability of the cathode is 33% higher than the one evaluated from the 2E cell.

The μ-RE design presented herein can be applied to virtually every SSB cell setup with thiophosphate SEs or other mechanically not too rigid SEs with little effort. Application of this setup will allow for better comparability between different studies. Therefore, due to the advantages of this setup, we encourage other researchers in the field to use of this type of reference electrodes and hope for a more widespread application.

Acknowledgments

Financial support by BASF SE within the International Network for Batteries and by Bundesministerium für Bildung und Forschung (BMBF) within the Cluster of Competence FESTBATT (project 03XP0177A) is acknowledged.

ORCID

Jonas Hertle https://orcid.org/0000-0001-8040-8038
Jürgen Janek https://orcid.org/0000-0002-9221-4756

References

1. J. Janek and W. G. Zeier, *Nat. Energy*, **1**, 16141 (2016).
2. K. J. Kim, M. Balaish, M. Wadaguchi, L. Kong, and J. L. M. Rupp, *Adv. Energy Mater.*, **11**, 1 (2021).
3. M. J. Kim, J. W. Park, B. G. Kim, Y. J. Lee, Y. C. Ha, S. M. Lee, and K. J. Baeg, *Sci. Rep.*, **10**, 1 (2020).
4. H. Lee, P. Oh, J. Kim, H. Cha, S. Chae, S. Lee, and J. Cho, *Adv. Mater.*, **31**, 31 (2019).
5. S. P. Culver, R. Koerver, W. G. Zeier, and J. Janek, *Adv. Energy Mater.*, **1900626**, 1900626 (2019).
6. A. Neumann, S. Randau, K. Becker-Steinberger, T. Danner, S. Hein, Z. Ning, J. Marrow, F. H. Richter, J. Janek, and A. Latz, *ACS Appl. Mater. Interfaces*, **12**, 9277 (2020).
7. F. Walther, R. Koerver, T. Fuchs, S. Ohno, J. Sann, M. Rohnke, W. G. Zeier, and J. Janek, *Chem. Mater.*, **31**(10), 3745 (2019).
8. J. E. Harlow et al., *J. Electrochem. Soc.*, **166**, A3031 (2019).
9. L. Zhou, T. T. Zuo, C. Y. Kwok, S. Y. Kim, A. Assoud, Q. Zhang, J. Janek, and L. F. Nazar, *Nat. Energy*, **7**, 83 (2022).
10. L. Nazar, L. Zhou, C. Y. Kwok, A. Shyamsunder, Q. Zhang, and X. Wu, *Energy Environ. Sci.*, **13**, 2056 (2020).
11. L. M. Riegger, R. Schlem, J. Sann, W. G. Zeier, and J. Janek, *Angew. Chemie - Int. Ed.*, **60**, 6718 (2021).
12. F. Walther, S. Randau, Y. Schneider, J. Sann, M. Rohnke, F. H. Richter, W. G. Zeier, and J. Janek, *Chem. Mater.*, **32**, 6123 (2020).
13. G. Conforto, R. Ruess, D. Schröder, E. Trevisanello, R. Fantin, F. H. Richter, and J. Janek, *J. Electrochem. Soc.*, **168**, 070546 (2021).
14. D. P. Abraham, S. D. Poppen, A. N. Jansen, J. Liu, and D. W. Dees, *Electrochim. Acta*, **49**, 4763 (2004).
15. A. N. Jansen, D. W. Dees, D. P. Abraham, K. Amine, and G. L. Henriksen, *J. Power Sources*, **174**, 373 (2007).
16. J. Zhou and P. H. L. Notten, *J. Electrochem. Soc.*, **151**, A2173 (2004).
17. C. Delacourt, P. L. Ridgway, V. Srinivasan, and V. Battaglia, *J. Electrochem. Soc.*, **161**, A1253 (2014).
18. M. W. Verbrugge, D. R. Baker, and B. J. Koch, *J. Power Sources*, **110**, 295 (2002).
19. S. Klink, E. Madej, E. Ventosa, A. Lindner, W. Schuhmann, and F. La Mantia, *Electrochem. Commun.*, **22**, 120 (2012).
20. S. Solchenbach, D. Pritzl, E. J. Y. Kong, J. Landesfeind, and H. A. Gasteiger, *J. Electrochem. Soc.*, **163**, A2265 (2016).
21. J. Landesfeind, D. Pritzl, and H. A. Gasteiger, *J. Electrochem. Soc.*, **164**, A1773 (2017).
22. M. Dollé, F. Orsini, A. S. Gozdz, and J.-M. Tarascon, *J. Electrochem. Soc.*, **148**, A851 (2001).
23. R. Raccichini, M. Amores, and G. Hinds, *Batteries*, **5**, 1 (2019).
24. J. Rutman and I. Riess, *Electrochim. Acta*, **52**, 6073 (2007).
25. S. B. Adler, *J. Electrochem. Soc.*, **149**, E166 (2002).
26. J. Winkler, P. V. Hendriksen, N. Bonanos, and M. Mogensen, *J. Electrochem. Soc.*, **145**, 1184 (1998).
27. C. Rosenkranz and J. Janek, *Solid State Ionics*, **82**, 95 (1995).
28. A. Ikezawa, G. Fukunishi, T. Okajima, F. Kitamura, K. Suzuki, M. Hirayama, R. Kanno, and H. Arai, *Electrochem. Commun.*, **116**, 106743 (2020).
29. Y. J. Nam, K. H. Park, D. Y. Oh, W. H. An, and Y. S. Jung, *J. Mater. Chem. A*, **6**, 14867 (2018).
30. G. H. Chang, H. U. Choi, S. Kang, J. Y. Park, and H. T. Lim, *Ionics (Kiel).*, **26**, 1555 (2020).
31. F. J. Simon, L. Blume, M. Hanauer, U. Sauter, and J. Janek, *J. Electrochem. Soc.*, **165**, A1363 (2018).
32. F. Walther, F. Strauss, X. Wu, B. Mogwitz, J. Hertle, J. Sann, M. Rohnke, T. Brezesinski, and J. Janek, *Chem. Mater.*, **33**, 2110 (2021).
33. P. Bach, M. Stratmann, I. Valencia-Jaime, A. H. Romero, and F. U. Renner, *Electrochim. Acta*, **164**, 81 (2015).
34. A. N. Dey, *J. Electrochem. Soc.*, **118**, 1547 (1971).
35. A. D. Pelton, *Bull. Alloy Phase Diagrams*, **7**, 228 (1986).
36. G. Kienast, J. Verma, and W. Klemm, *ZAAC - J. Inorg. Gen. Chem.*, **310**, 143 (1961).
37. R. W. G. Wyckoff, *Crystal Structures* (New York, Interscience Publishers) (1963).
38. P. Braun, C. Uhlmann, M. Weiss, A. Weber, and E. Ivers-Tiffée, *J. Power Sources*, **393**, 119 (2018).
39. Y. Kato, S. Shiotani, K. Morita, K. Suzuki, M. Hirayama, and R. Kanno, *J. Phys. Chem. Lett.*, **9**, 607 (2018).
40. J. Bisquert, *Phys. Chem. Chem. Phys.*, **2**, 4185 (2000).

3.2 Publication II

The second publication introduces a benchmarking approach for coatings in SSB.[198] Prior to this publication no systematic approach to evaluate different coatings for SSB was reported in literature. This makes the comparison of different coating strategies and chemistries difficult. This publication combines state-of-the-art analytical and electrochemical techniques. The previously established 3E setup was used to get the most reliable results for rate-test performance. This was combined with in-depth ToF-SIMS analysis. Statistical analysis using PCA allowed for in depth comparison of the coatings showing their performance in different degradation pathways.

The findings of this publication can be used for Li-SSB research by other researchers. Furthermore, the findings can be transferred to other systems by establishing equivalent PCA analysis and ToF-SIMS analysis. The 3E-setup used in this study can be used in other systems as well when appropriate modifications are applied.

This study was part of the International Network for Batteries and Electrochemistry by BASF SE. The project was accompanied by X. Wu and Holger Schneider through scientific exchange. Reprinted with permission from Hertle, J.; Walther, F.; Lombardo, T.; Kern, C.; Pavlovic, B.; Mogwitz, B.; Schneider, H.; Rohnke, M.; Janek, J., Benchmarking of Coatings for Cathode Active Materials in Solid-State Batteries, *ACS Appl. Mater. & Interfaces*, 16 (7), 9400-9413, **2024**. doi:10.1021/acsami.3c15723.

J. Hertle designed the experiments and the cell design, analyzed the results and wrote the manuscript. F. Walther carried out ToF-SIMS experiments and helped with the experimental design and the structure of the manuscript. T. Lombardo and C. Kern wrote and developed the Python script for automated ToF-SIMS analysis. B. Pavlovic built the cells for the benchmarking. B. Mogwitz carried out FIB-SEM experiments. H. Schneider helped with scientific feedback. M. Rohnke helped with the ToF-SIMS and PCA analysis. J. Janek supervised the study.

ACS APPLIED MATERIALS & INTERFACES

www.acsami.org Research Article

Benchmarking of Coatings for Cathode Active Materials in Solid-State Batteries Using Surface Analysis and Reference Electrodes

Jonas Hertle, Felix Walther, Teo Lombardo, Christine Kern, Boris Pavlovic, Boris Mogwitz, Xiaohan Wu, Holger Schneider, Marcus Rohnke, and Jürgen Janek*

Cite This: ACS Appl. Mater. Interfaces 2024, 16, 9400−9413 Read Online

ACCESS | Metrics & More | Article Recommendations | Supporting Information

ABSTRACT: Fast and reliable evaluation of degradation and performance of cathode active materials (CAMs) for solid-state batteries (SSBs) is crucial to help better understand these systems and enable the synthesis of well-performing CAMs. However, there is a lack of well-thought-out procedures to reliably evaluate CAMs in SSBs. Current approaches often rely on X-ray photoelectron spectroscopy (XPS) for the evaluation of degradation. Unfortunately, XPS sensitivity is not very high, and minor but relevant degradation products may not be detected and distinguished. Furthermore, degradation caused by the current collector (CC) itself is usually not distinguished from CAM-induced degradation. This study uses a modified CC, which allows us to separate electrochemical degradation caused by the CC from degradation at the CAM itself. Using this CC, we present an approach using time-of-flight secondary ions mass spectrometry (ToF-SIMS) that offers high sensitivity and reliability. Principal component analysis (PCA) is applied to differentiate secondary ions as well as identify those mass fragments that correlate with degradation products. This approach also enables distinguishing between different pathways of degradation. To evaluate the kinetic performance of the samples, three-electrode rate tests are performed. Electrochemical characterization evaluates the kinetic performance of the samples under investigation. The samples are finally rated with a score that allows a reliable comparison between the different materials and offers a complete picture of the materials' characteristics in terms of electrochemical performance and degradation.

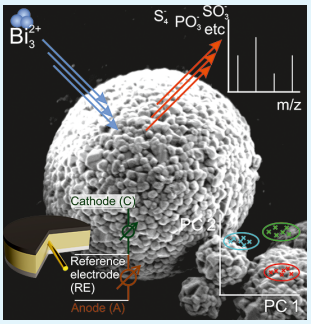

KEYWORDS: *solid-state battery, sulfide electrolyte, solid electrolyte, three-electrode setup, degradation, coating*

INTRODUCTION

Solid-state batteries (SSBs) are potentially able to surpass liquid-based lithium-ion batteries with increased energy and power density.[1−3] In SSBs, the liquid electrolyte is at least partially replaced by a single ion conducting solid electrolyte (SE).[4−6] In SSB cells, a dense solid electrolyte (SE) separator separates the anode and the cathode and thus stops any chemical crossover. In academic research, various negative electrode materials are used. The two-phase systems In/InLi and $Li_4Ti_5O_{12}/Li_7Ti_5O_{12}$ (LTO) are often chosen because of their constant electrode potentials independent from the state-of-charge (SOC) and their excellent stability together with SEs.[7−10] Lithium metal provides the highest specific capacity and leads to a high energy density of full cells.[11] Recently, silicon gained attention for use as an anode material in both LIBs and lithium SSBs.[12] A high specific capacity of 3590 mAh/g and its low potential of 0.4 V versus Li^+/Li make it suitable for high-energy density applications without the risk of dendrite formation.[13] Although first investigations of the Li−Si system date back as far as 1976 and first applications were presented more than 20 years ago, the use of the materials remains challenging.[14−16] High volume changes of up to 300% makes silicon electrodes with a long cycle life challenging, and a trade-off between a high volumetric energy density and long cycle-life has to be found.[12]

As cathode active materials (CAM), mostly layered oxides ($Li_xNi_yCo_zMn_{1-y-z}O_2$, NCM) and $LiFePO_4/FePO_4$ are used.[17−21] These materials provide the best energy densities for SSB and offer high potentials as well. For SEs, usually three groups are distinguished: first, oxides, such as cubic $Li_{6.25}Al_{0.25}La_3Zr_2O_{12}$ (LLZO) and $Li_{1+x}Al_xTi_{2-x}(PO_4)_3$ (LATP).[22−26] Despite their good electrochemical stability, their use is hampered by an ionic conductivity (usually <1 mS/cm) that is too low for high-energy and high-power composite electrodes, and their difficult processability due to their hardness and brittleness. Polymer electrolytes like poly(ethylene oxide) (PEO), for example, with lithium bis(trifluoromethane)sulfonimide (LiTFSI) as conducting salt, have excellent mechanic properties and processability.[27−31] However, the ionic conductivity is even lower at room

Received: October 26, 2023
Revised: December 31, 2023
Accepted: January 10, 2024
Published: February 7, 2024

temperature and the transference number of the Li^+ ions is small (σ < 1 mS/cm at 80 °C, $t_+ \approx 0.2$).[32] Thiophosphates (often also named as sulfides for simplicity) and ordered solid solutions with halides or metal sulfides such as Li_6PS_5Cl (LPSCl)[33] or $Li_{10}GeP_2S_{12}$ (LGPS)[34] are often seen as the most promising candidates because of their superior ionic conductivity of up to 32 mS/cm at room temperature and their good mechanical properties.[35]

The combination of thiophosphate-based solid electrolytes and NCM active materials, however, leads to different types of degradation.[36,37] First, morphological degradation takes place. This is due to the expansion and contraction of the CAM during charge and discharge, which leads to contact loss and cracking of the active materials' particles ultimately leading to high overpotentials and a lower practical capacity in the cell.[8,18] Second, when used in cathode composite electrodes, thiophosphate SE tend to decompose at high potentials, forming reactive oxygen and posing problems with long-term stability. Coatings of CAMs are a widespread approach to mitigate the degradation at the interface between the CAM and SE.[38,39] Additionally, they are used to increase the rate capability of the system by lowering the charge-transfer resistance between the CAM and the SE. Examples for coatings of cathode active materials are found frequently in the literature and the need for coatings of CAMs in all solid-state cells was already recognized by Ohta et al. in 2007.[38] The analyses reported in literature usually focus on the evaluation of a single coating in comparison to a not intentionally coated material, namely, a CAM with natural surface residues such as Li_2CO_3 and LiOH. These analyses are often combined with electrochemical tests such as electrochemical impedance spectroscopy (EIS), rate tests, and long-term cycling as well as post-mortem analysis with X-ray photoelectron spectroscopy (XPS) and time-of-flight secondary ion mass spectroscopy (ToF-SIMS).[10,37,38,40−44]

Since cathode degradation is caused both by morphological degradation of the CAM as well as by chemical degradation and as these contributions are not further differentiated, it is often unclear which factors contribute to a well working coating. Furthermore, coating compositions are difficult to assess due to the nature of only several nanometer thin films.[45] The positive effects of a coating are mostly attributed to their bulk properties, although the exact composition is unclear as lithium residual compounds can become part of the actual coating. Effects like the microstructure, residues on the CAM surface, and exact stochiometric compositions are not taken into consideration. Due to these limitations, only general and unspecific statements about coatings are found in the literature. It remains unclear which coating parameters, such as the coating thickness, ratio of precursor materials, annealing temperature, and so on, are leading to the best results. Finding optimal coatings is therefore quite difficult, and fundamental knowledge on the mechanism of the function of coatings is still mostly unknown. Apparently, the previous analytical approaches are not sufficient to completely characterize a coating; better and more reliable techniques are needed to allow for a better understanding of the functionality of different coating materials and techniques.

In this paper, we describe a fast and reliable approach to investigate the degradation of thiophosphate solid electrolytes with ToF-SIMS, allowing a direct comparison of different coatings. A full characterization includes the analysis of the coating microstructure as well as composition, electrochemical characterization such as the initial capacity, Coulombic efficiency, and rate tests as well as analysis of the degradation products caused by electrochemical and chemical decomposition at the SE|CAM interface. Structural degradation such as cracking and contact loss between the SE and the CAM is not included here as this highly depends on the CAM, the SE, and other additives used in the cell as well as the pressure that is applied during cycling. This is also why this study does not include long-term cycling data. According to the literature, the morphological degradation in SSBs can be severe. This effect is dominated by the choice of SE, specifically the crystallinity of SE, and the choice of additives. The addition of flexible binders, for example, reduces the effect of morphological degradation.[18] Introducing a binder to the cathode composite complicates the cathode composite further and makes the analysis more complicated. Here, we reduce the complexity of the system as much as possible without compromising the functionality of the cell; our target is the role of the coating.

Our strategy to investigate degradation in all-solid-state cells relies on a straightforward workflow: Electrochemical degradation is quantified by a novel ToF-SIMS analysis approach with higher sensitivity and less variance in the data by using a modified CC. Electrochemical measurements and rate tests are performed using a three-electrode setup to secure that only the cathode kinetics is investigated. No further additives are used to make sure that the differences in the performance arise from the differences in the active material itself. Combining both ToF-SIMS and electrochemical data allows for a complete assessment of the active material. Results are displayed in a radar chart that represents the effect of the coating on the interfacial degradation and the performance. This allows a fast comparison of different coatings and paves the way to finding the best coating for high-performance NCM composite cathodes.

EXPERIMENTAL SECTION

Materials. For the fabrication of all-solid-state battery cells, commercially available crystalline SE Li_6PS_5Cl with a measured ionic conductivity of σ = 1.4 mS/cm (NEI Corp., NJ, USA) was used without further modification. The Li_6PS_5Cl SE was received and stored in an argon-filled glovebox to maintain its integrity with impurity levels of oxygen ($p(O_2)/p$ < 1.0 ppm) and water vapor ($p(H_2O)/p$ < 1.0 ppm) being meticulously controlled. Prior to assembly, the indium foil (100 μm thickness, chemPUR, Germany) was subjected to vacuum-drying at 60 °C for at least 48 h. The lithium metal (abcr GmbH, Germany) used in this study was also stored in the argon-filled glovebox. The lithium foil was prepared by compressing small pieces (∼5 mg) of lithium between pouch bag foils, resulting in a final thickness of approximately 200 μm. Out of these foils, discs with a 4 mm diameter were punched out. The CAMs were provided by BASF SE and underwent vacuum-drying at 250 °C for 12 h prior to utilization. The uncoated CAM is $LiNi_{0.85}Co_{0.10}Mn_{0.05}O_2$ (NCM85, d_{50} = 3.5 μm, d_{90} = 5.0 μm), and all other coated CAMs were made using this base CAM.

Cell Setup. The basic cell setup used in this study can be found in previous publications.[7,46] A few modifications were applied to the setup to better suit the needs for this study which are described below.[47]

Current Collectors (CCs). CCs for three-electrode measurements were made of stainless steel with a polished surface toward the SSB pellet to ensure maximum surface smoothness and homogeneity of the pellets built. All CCs were polished with a 250 nm polycrystalline diamond suspension in the last step, and only freshly polished CCs were used for cell construction.

CCs for ToF-SIMS measurements were produced by gluing an Al_2O_3 cylinder into a stainless-steel CC as shown in Figure 1. These

https://doi.org/10.1021/acsami.3c15723
ACS Appl. Mater. Interfaces 2024, 16, 9400−9413

ACS Applied Materials & Interfaces www.acsami.org Research Article

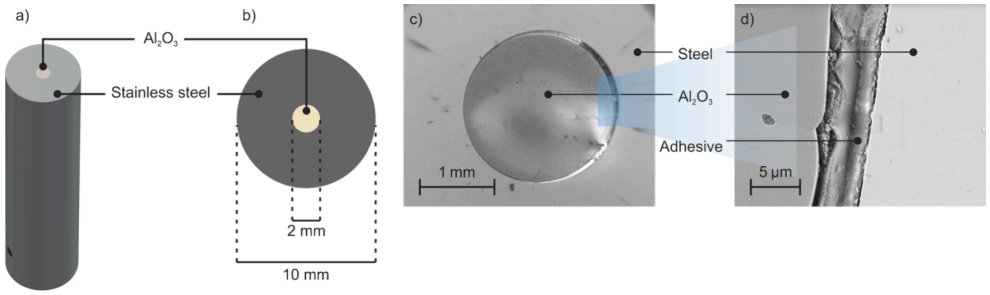

Figure 1. Modified CC were used for ToF-SIMS analysis. The inner part of the CC consists of Al_2O_3, which is neither ionically nor electronically conductive. (a, b) Different schematic views on the steel CC rod; (c) top view and (d) cross section of the CC with the alumina area (optical micrographs).

CCs were subsequently polished with the same procedure as that for the pure steel CCs.

Two-Electrode Setup and Cycling. Cells for degradation studies with ToF-SIMS were built according to the following procedure. 60 mg of Li_6PS_5Cl was pressed with a hand-press to form a SE separator layer. On top of the resulting pellet, 12 mg of the cathode composite (80 wt:20 wt CAM:SE) was distributed homogeneously, and the whole pellet was pressed at 374 MPa for 3 min. Afterward, indium foil (9 mm diameter, 100 μm thickness) and lithium foil (4 mm diameter, ~200 μm thickness) were placed on the other side of the solid electrolyte separator. The complete cell was held at a constant pressure of 50 MPa during cycling.

The cells were cycled at 0.05 C (1 C = 1.92 mA $\triangleq$ 2.44 mA/cm^2) for 1.5 cycles (charge−discharge−charge) and relaxed overnight until the start of the ToF-SIMS measurement.

Three-Electrode Setup and Rate Test. Three-electrode cells as described in the literature were used.[47] 60 mg of SE was hand-pressed, and the gold-wire reference electrode was placed on top. Another layer of 60 mg of SE was put on top, and the pellet was hand-pressed again. 12 mg of the cathode composite (67 wt:30 wt:3 wt CAM:SE:carbon) were distributed homogeneously on top, and the pellet was pressed at 374 MPa for 3 min. Afterward, indium foil (9 mm diameter, 100 μm thickness) and lithium foil (4 mm diameter, ~100 μm thickness) were placed on the other side of the solid electrolyte separator. The complete cell was held at a constant pressure of 50 MPa during cycling.

All cells were cycled at 0.1, 0.3, 1.0, and 2.0 C for two cycles each with a 2 h rest step in between each charge and discharge step.

ToF-SIMS Measurements. ToF-SIMS measurements were performed on a TOF-SIMS 5−100 by IonTOF GmbH Germany, which is equipped with a 25 keV Bi cluster primary ion gun for SIMS analysis and a dual-source column for depth-profiling with up to 2 keV by using O_2^+ or Cs^+.

The pellet that was used for ToF-SIMS mapping was prepared with a FIB in a Xe plasma FIB-SEM prior to the measurement as described below. The surface of the sample was flooded with low-energy electrons for charge compensation. The measurement was performed in the negative ion mode with 25 keV Bi_3^{2+} primary ions with a total ion dose of 5 × 10^{12} ions/cm^2, a cycle time of 60 μs in the spectrometry mode, and a mass resolution of ~6000. The data were analyzed with SurfaceLab 7.3 (IONTOF GmbH, Germany).

Comparing ToF-SIMS results requires scaling to account for the intrinsic heterogeneities of battery samples, including the presence of more or fewer particles/pores in certain regions or their different rugosity/topography, which can shield part of the ions generated through the first ion beam, leading to fewer secondary ions (SI) detected by the analyzer.

Several procedures can be used for this purpose, the easiest being scaling the SI count by the total number of SIs detected during the measurement. Another (conceptually similar) approach consists of scaling by the number of SIs (peak area) associated with a given species. In the context of battery electrodes, a possible choice for this is a peak specifically associated with the active material. In both cases, however, the data are scaled using the SIs collected over the entire region of analysis, therefore falling short in accounting for the heterogeneities inside the region of analysis (i.e., CAM-related SI signal being much higher in the subregion where a CAM particle stands and lower in subregions containing pores).

Analyzing smaller regions would overcome or at least minimize this limitation but at the expense of representativeness. Alternatively, it is possible to subdivide the region of analysis (in our case, 150 × 150 μm^2) into n pixels (in our case, 256 × 256) and analyze the single spectrum obtained by each of those rather than the overall spectrum. In other words, it is possible to scale each peak of each spectrum of each pixel by the total ion count (or by the ions associated with a reference species) measured from that same pixel. Afterward, the scaled value of each pixel is summed to reconstruct the data representative of the entire region of analysis. This approach can therefore combine the representativeness brought by the analysis of a relatively large area with the higher accuracy offered by consideration of its local heterogeneities.

Pixel-by-pixel normalization was used for the data analysis in this study. The analysis was performed through an in-house Python code, which performed the pixel-by-pixel analysis on all the peaks identified as relevant.[48] The data are scaled by either the total ion count or a reference species associated with the CAM (in our case, NiO_2^-), offering both of these results. In addition, for each sample, 14 different regions were analyzed to obtain statistically relevant information. The code automatically compares all the results obtained by the same sample and computes the associated statistics (minimum, maximum, average, median, standard deviation, first and third quartiles). Lastly, the code can compare the so-obtained results with a reference sample, allowing us to easily quantify the relative difference (%) between the reference and the other samples for each species analyzed. For better clarity, we provide only the average of the signals in the main part of this publication.

Orbitrap SIMS. The IONTOF M6 Hybrid SIMS has both a ToF and an OrbiTrap analyzer. In general, the high mass resolving performance ($m/\Delta m$ > 240,000 at m/z = 200) and high mass accuracy (<2 ppm) of the OrbiTrap analyzer enable accurate mass calibration and signal assignment and are therefore ideally suited to create a mass list for the investigation of degradation products in battery electrodes. Parameters for OrbiTrap mass spectra using a liquid metal ion gun (LMIG) as a primary ion gun were the following: 30 keV Bi_3^+ as the primary ion species with a primary ion current of 0.210 pA. The field of view was 150 × 150 μm^2 with a dose density of 1.00 × 10^{12} ions/cm^2. The ROI was rastered in the random mode with 51 × 51 pixels and a cycle time of 100 μs in the negative ion mode. For each sample, three measurements were acquired. The mass range was from m/z = 50 to 750 and the mass resolution (fwhm) was $m/\Delta m$ > 400,000 (at m/z = 78.95, PO_3^- signal). Using the OrbiTrap mass spectra, a mass list was generated, which was then applied to ToF-SIMS measurements. Deviations of the assigned masses were less than ±10 ppm. OrbiTrap mass calibration was performed once at the

https://doi.org/10.1021/acsami.3c15723
ACS Appl. Mater. Interfaces 2024, 16, 9400−9413

beginning of the measurement session using Ag clusters between Ag_1 and Ag_{15} from a reference sample. As the mass calibration remains stable for >25 h, no recalibration using known peaks from the spectrum was necessary. Data analysis of M6 Hybrid SIMS measurements was done with Surface Lab Software version 7.3 (IONTOF GmbH, Münster, Germany).

Principal Component Analysis. For principal component analysis (PCA), first, the intensities of each fragment as obtained from ToF-SIMS analysis (normalized to the total ion intensity) were exported for the cycled and uncycled samples. Both the cycled and uncycled samples were measured at $n \geq 10$ regions for better reproducibility. As the intensities of different fragments may vary by multiple orders of magnitude, the PCA was performed in relative rather than absolute terms. In other words, for each fragment, the spectrum for which the highest intensity was found was used as a relative reference. The value of the area underneath this peak was then scaled to 1, and all of the intensities of the same peak for the other spectra were scaled accordingly. This approach ensures that the PCA is not dominated by the SI with the highest intensity and allows focusing on the relative differences between cycled and uncycled samples.

The PCA loadings (representing the importance of each SI in describing the differences between the analyzed samples) were then used to evaluate the effectiveness of coatings to prevent (electro)-chemical degradation. This procedure was carried out with a python code that is available on GitHub.[49] A complete mass list used in this study can be found in Table S1.

Calculation of Degradation Scores. To estimate the degree of degradation that occurred in the various samples, a raw degradation score DS_{raw} is introduced as outlined in eq 1, where n is the number of measurements for a particular sample, m is the specific measurement spot, f is a fragment, l is the loading of that fragment, and v is the normalized intensity of that fragment obtained from ToF-SIMS analysis.

$$DS_{raw} = \frac{1}{n} \sum_{m} \sum_{f} l \times v \tag{1}$$

Afterward, the raw scores DS_{raw} were scaled such that the uncycled sample has a value of 0 and the uncoated cycled samples have a value of 1, resulting in the degradation score DS. Several degradation scores were computed with a general degradation score where all the fragments are considered for the score as well as specific degradation scores where only certain fragments are taken into consideration. For the polysulfides, phosphate and sulfate degradation scores, namely, only the fragments labeled polysulfide PO_y and SO_y in Table S2, respectively, are taken into consideration.

XPS Measurements. X-ray photoelectron spectroscopy (XPS) measurements were conducted using a PHI5000 Versa Probe II system (Physical Electronics GmbH) instrument. All specimens were transferred from the glovebox to the spectrometer by utilizing a transfer system, ensuring continuous exposure to an argon environment throughout the process. The analysis employed monochromatic Al K_α radiation with an energy of 1486.6 eV. The X-ray source was operated at a power of 50 W and a voltage of 15 kV. The analysis beam had a diameter of 200 μm. To achieve charge neutralization, a dual beam system combining an ion beam and a low-energy electron beam was utilized. Pass energies of 23.50 were used. Data analysis was carried out using CasaXPS software (version 2.3.22, Casa Software Ltd.).

Prior to analysis, calibration of the XP spectra was conducted using a β-Li_3PS_4 reference material. The calibration was performed with respect to the signal of adventitious carbon at 284.8 eV. Subsequently, the signal position of the primary component of the S 2p signal corresponding to the $(PS_4)_3^-$ units was determined. The XP spectra of the composite cathodes were calibrated based on the main component of the β-Li_3PS_4 reference, thereby mitigating potential surface effects.

Signal fitting was executed using a Shirley background and GL(30) line shapes. Standard fitting constraints were implemented, including theoretical signal area ratios dependent on the orbital (e.g., p orbitals 1:2) and constraints on the full width at half-maximum (fwhm), and referenced to published values for spin−orbit splitting.

SEM and FIB-SEM Measurements. The SSB pellet was fixed to the sample holder using nonconductive tape. To ensure minimal exposure to air, all samples were directly transferred using a LEICA EM VCT500 transfer system, ensuring a transfer process without contact with air or moisture.

Focused ion beam (FIB) craters were generated using an XEIA3 Triglav instrument from Tescan utilizing a 30 kV Xenon plasma FIB operating at a current of 1 μA. Subsequent polishing of the craters was performed at 30 kV and 100 nA. FIB-scanning electron microscopy (SEM) measurements were conducted using a XEIA3 Triglav system from Tescan. SEM images were acquired at a 3 kV beam energy with a current of 290 pA, employing both a secondary electron detector and a backscattered electron (BSE) detector.

Further SEM measurements were carried out using a Zeiss Merlin Gemini instrument. Electron images were obtained using either a secondary electron or BSE detector.

RESULTS AND DISCUSSION

Experimental Design. *Two Pathways of Degradation.* In ToF-SIMS, a so-called primary ion beam scans the sample surface. During a collision cascade between primary ions and the sample surface among neutrals and electrons, SIs are also formed and collected by an electric field. Finally, the SIs are analyzed by their mass/charge ratio and detected locally resolved. A detailed introduction of the application of SIMS in battery research can be found in a publication by Lombardo et al.[48] For ToF-SIMS measurements, a modified CC was used as shown in Figure 1. Previous results show that there are two main pathways of degradation in solid-state cathode composites of thiophosphate-type SEs. One is arising from the SE being in contact with the CC and the other one is arising from the SE being in contact with the CAM particles.

Degradation at the Current Collector. Degradation arising from contact with a CC mainly leads to the formation of polysulfides, that is, oxidation of sulfur. This can be seen in XPS measurements as a shoulder in the S 2p signal at higher binding energies at around E_B = 163−165 eV as shown in Figure 3. This degradation occurs independently from the CAM as the surface of the cathode composite is always in contact with the CC and changes only slightly when different CAMs are used. Small differences in this degradation signal can arise from deviations in the electronic conductivity of the CAM surface as the electronically conductive CAMs serve as CCs themselves.[50] This signal of oxidation products is often used nonetheless to quantify degradation in a cathode composite despite its presence in any case.

Degradation by Oxygen. The other pathway of degradation directly at the SE|CAM contact leads to oxidation of the SE by oxygen, and sulfite/sulfate (Li_xSO_y) and phosphite/phosphate (Li_xPO_y) compounds are formed. These compounds can theoretically be detected with XPS, but in practice, the signal-to-noise ratio of SO_x is usually too low. Therefore, only polysulfides and general PO_x species can be detected with XPS, which is mainly attributed to CC-driven degradation as pointed out above.

Limited Suitability of XPS Surface Spectra for Analysis. Because of the effects described above, the XP surface spectra of cathode composite pellets are not suited to investigate degradation in solid-state cells properly, and a distinction is possible only between samples with little degradation and severe degradation. The evaluation of finer distinctions, that is, differences between different coatings, is not possible, and

https://doi.org/10.1021/acsami.3c15723
ACS Appl. Mater. Interfaces 2024, 16, 9400−9413

distinctions between degradation pathways are not possible. This is shown in previous publications by Walther et al., where cathode composites were investigated with XPS and ToF-SIMS.[36,37,51]

Sputtering to Minimize Current Collector Effects. As stated above, the CC leads to degradation of the SE forming mainly oxidized sulfur species like polysulfides. Sputtering the surface of the cathode composite pellet that removes this degradation layer caused by the CC only resolves this issue partly. The surface of the cathode composite is rough despite using polished (roughness of <250 nm) CCs. This roughness is determined by the particle size of the CAM and SE used. In the present case, the CAM particle size was in the range of 1−5 μm.

Sputtering this surface removes only a part of the degradation layer caused by the CC as depicted in Figure 2.

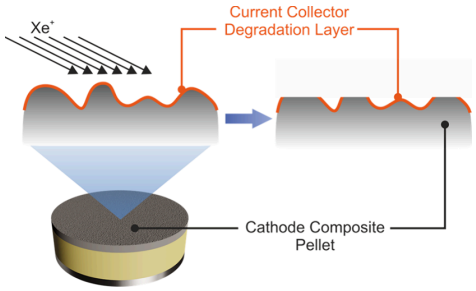

Figure 2. Sputtering the surface of a cathode composite pellet removes the degradation layer on top of the cathode composite pellet and leads to analytical results that are difficult to interpret due to uneven sputter removal.

Additionally, sputtering always alters the chemical composition of the investigated surface, which complicates analysis even further. These issues can be avoided when a part of the sample is not contacted by the CC, that is, it is only contacted by a nonconductive and inert material. In this work, this is achieved by using a modified CC with an outer stainless steel section and an inner Al_2O_3 section. The inner Al_2O_3 part is both electronically and ionically insulating, chemically inert, and mechanically stable.

Although this inner part is not directly contacted to the CC, the CAM particles are charged and discharged through contact with other active material particles due to their good electronic conductivity. As long as the CAM particles form a percolating network, the CAM particles in the inner section can be charged and discharged. Using a high loading of the active material (80:20 wt:wt, 63:37 vol:vol) ensures that all CAM particles are connected via their percolation network, and low currents during charging and discharging (0.05 C, 122 μA/cm^2) ensure negligible influence of overpotentials on the electrodes. This ensures that the SE on the surface of the pellet is subjected only to degradation caused by the CAM and not due to degradation caused by the CC. Separating CC-related degradation from CAM-related degradation allows for a better study of the CAM-related degradation.

Electrochemical Characterization besides SIMS Analysis. ToF-SIMS measurements offer information about the degree of degradation after cycling, and of course, the electrochemical performance of a coating is important as well. A very thick coating, potentially also a poorly conducting coating, for example, may lead to a low degree of degradation of the SE but would also perform electrochemically quite poor especially in high-current tests. A complete evaluation of any coating must therefore include electrochemical data as well, and in this study, we use rate tests for this evaluation. As we previously reported, it is important to use reference electrodes and three-electrode cells for the correct evaluation of the rate capability of an active material, thus avoiding any detrimental influence from the counter electrode (in the present case, the anode). The same setup as previously reported is used for this purpose.[47]

Long-Term Cycling. Previous publications in the field also report on long-term cycling as part of coating tests. There are several reasons why long-term cycling is not suited to the benchmarking presented in this study. In long-term cycling of SSBs, there is always an overlap between (electro)chemical and chemo-mechanical degradation. Due to the volume increase and decrease during cycling, the SE-CAM contact is partially lost in the electrode, leading to a decrease of the cell performance.[18] Investigating the long-term performance with the setup presented in this study (no binder, no conductive additives, crystalline SE), serious chemo-mechanical degradation is expected, and the difference introduced by the coating is small as the bulk active material is the same in every sample. The combined evaluation of degradation products and rate performance gives a sufficient and complete overview of the coating performance, and the comparison between different coatings becomes feasible. This approach also allows optimizing coatings, and balancing high-power performance and a long cycle life becomes possible.

In order to investigate and compare degradation of the SE in combination with different CAMs, different coatings were chosen. The coatings used for this comparison are listed in Table 1. These materials were selected as they represent commonly used coatings on the one hand ($LiNbO_3$ and ZrO_2) and, on the other hand, a promising new coating (X). This coating and the ZrO_2 coating were applied with two different thicknesses to investigate the influence of the coating thickness.

Table 1. CAMs Used in This Study[a]

CAM name	coating	amount
NCM uncoated	none	
NCM LiNbO3	$LiNbO_3$	1 wt %
NCM ZrO_2 thin	ZrO_2	1 wt %
NCM ZrO_2 thick	ZrO_2	5 wt %
NCM X thin	X	1 wt %
NCM X thick	X	5 wt %

[a]All coated samples are based on the uncoated material; that is, a coating was applied to the uncoated NCM.

Tof-SIMS and XPS. *Proof of Principle: XPS Analysis.* To show the difference in the inner and outer regions of the sample, XP spectra were recorded. The results are shown in Figure 3. The spectrum recorded on the outer steel contacted part shows oxidized sulfur at around E_B = 163−165 eV as a pronounced shoulder in the S 2p signal, indicating the formation of polysulfide species.[9] The phosphorus P 2p signal shows the oxidation of the phosphorus as well, which is visible as a shoulder in the range E_B = 132−136 eV. This becomes especially obvious when compared to the spectra recorded in the inner Al_2O_3 part, which shows a lower signal intensity in

https://doi.org/10.1021/acsami.3c15723
ACS Appl. Mater. Interfaces 2024, 16, 9400−9413

ACS Applied Materials & Interfaces www.acsami.org Research Article

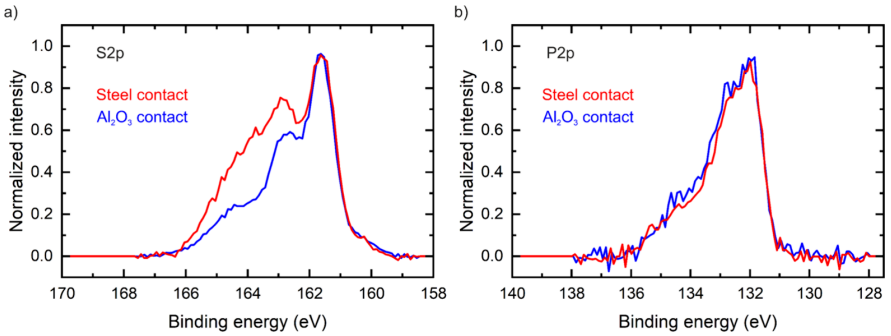

Figure 3. XP spectra (minimum to maximum normalized, background-subtracted) of a cathode composite contacted with the outer steel part (red) and Al_2O_3 inner part (blue). The S 2p signal (a) shows a pronounced shoulder at higher binding energies around 163−165 eV for the steel contacted spectrum. The P 2p (b) signal shows the same signal intensity for oxidized phosphorus species at higher binding energies of 132−136 eV as well. This is due to the contact with the stainless-steel CC, which leads to degradation of the solid electrolyte. However, the phosphorus degradation involves oxygen, which is the same for both the steel contacted and the Al_2O_3 contacted part of the sample. The graph without a background correction can be found in Figure S10.

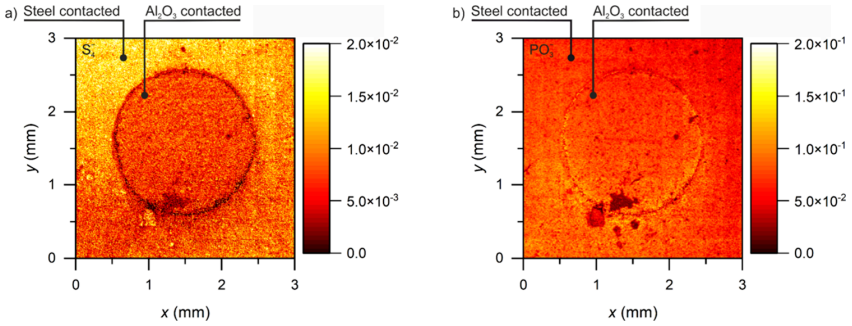

Figure 4. Large area SIMS scan of the cathode composite pellet, which was cycled with the modified CC. The image is normalized to the total ion intensity. (a) The S_4^- signal is much less pronounced in the inner part where the sample was contacted by Al_2O_3. As the S_4^- signal is indicative of polysulfide formation, which is driven by the CC, it can be concluded that this pathway of degradation is indeed suppressed in the inner part of the sample. (b) The PO_3^- signal is spread out equally throughout the whole pellet's surface. The PO_3^- signal is indicative of degradation driven by the oxygen containing CAM. As the CAM distribution is homogeneous throughout the whole pellet, the respective degradation products are spread out homogeneously as well. Furthermore, no significant change in the intensity can be observed, proving the concept of the modified CC.

this region and therefore lower amounts of degradation. The S 2p signal at around 169 eV is indicative of one of the known pathways of solid electrolyte degradation; however, this signal is hardly detectable in the recorded spectra.[9,36] Therefore, XPS is not suited to investigate coatings in solid-state cells as the compounds of the most interesting degradation pathway remain undetected, and the detected degradation products are mainly caused by the contact of the SE with the CC and are hence independent from the materials used.

Proof of Principle: ToF-SIMS. The working principle of the modified CC was further investigated by ToF-SIMS measurements. Large area scans of the inner Al_2O_3 and outer stainless-steel part were acquired. In these spectra, degradation products can be assigned to different fragments, that is, to SIs with different m/z ratios. Depending on the pathway of degradation, different degradation products form. CC-driven degradation leads to the formation of polysulfides, and these can be detected by S_x^- signals. As the inner part is contacted to Al_2O_3, the formation of polysulfides is suppressed in this area as can be seen in Figure 4a. The Al_2O_3 contacted part shows a smaller signal; however, the signal is not completely absent. This is due to two reasons. First, these fragments can be formed during a collision cascade with the Bi clusters even when no degradation products are present. The smaller the value x for the S_x^- fragment, the higher the probability that these fragments are formed during SIMS analysis; see Figure S3. For $x = 1$ and $x = 2$, no significant difference between the steel and the Al_2O_3 contacted area are observed (Figure S3a,b). For higher values ($x \geq 3$), the probability of these fragments being formed upon impact of the Bi clusters with the solid electrolyte becomes lower, and mostly degradation products are detected. For S_3^- and S_4^-, the difference between steel and the Al_2O_3 contacted area is easily detectable (Figure S3c,d). For even larger fragments such as S_7^- and S_8^-, the difference is still observable; however, the ionization probability gets lower and the signal-to-noise ratio of the mass spectrometric data is smaller. However, even for the signals where the difference between the inner and outer parts is observable, polysulfides are still detected in the inner Al_2O_3 region. This is because the CAM particles are electronically conductive and form a percolating network; that is, they act as CCs as described above. Because the CAM is in contact with the SE, polysulfides are formed as well. Due to the absence of the steel CC on top of the sample, the amount of polysulfides is reduced.

The distribution of oxygenated fragments such as SO_2^-, SO_3^-, PO_2^-, and PO_3^- can be evaluated in the same way. These

https://doi.org/10.1021/acsami.3c15723
ACS Appl. Mater. Interfaces 2024, 16, 9400−9413

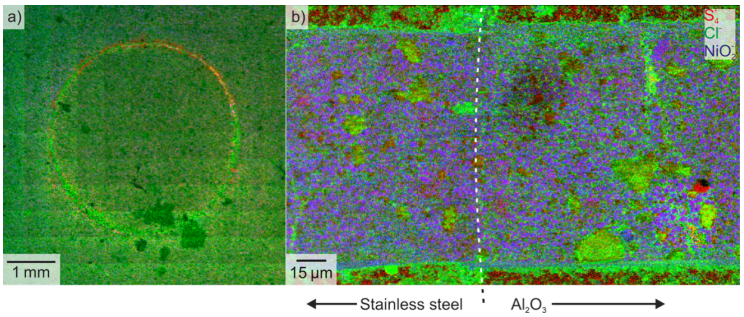

Figure 5. (a) Large-area scan of a cathode composite pellet without surface modifications. Here, mainly the SE shown in green (Cl^- signal) is visible. (b) High-lateral resolution ToF-SIMS image of a large area cross-section (FIB-cut with 5°) of a cathode composite pellet. The white dotted line marks the border between the steel and the Al_2O_3 contacts. CAM particles are distinctly visible in blue. The solid electrolyte is represented by the Cl^- signal shown in green. Single relatively large particles of SE are visible as well as the homogeneous distribution between the CAM particles in combination with degradation products shown in red.

degradation products are only formed in the presence of the active material as this is the only source of oxygen in the cathode. Therefore, if the CAM particles are connected through a percolation network within the electrode, the same amount of degradation products is expected on top of the electrode regardless of contact with Al_2O_3 or steel. In fact, there is no significant difference in the PO_3^- signal between the steel-contacted and the Al_2O_3-contacted regions in Figure 4b, confirming that there is no major difference in the amount of oxygenated degradation products. Figure S1 shows further signals SO_3^- and Li^- with no significant difference between the steel-contacted and the Al_2O_3-contacted regions. To further confirm the working principle of this analytical setup, the upper part of the pellet was removed with a low-angle FIB cut. The sample was tilted in a way that allowed a shallow cutting angle of only 10°. The cut was positioned at the edge between the steel and the Al_2O_3 contacted part of the pellet surface. This removes the upper few micrometers of the pellet and reveals a large cross-sectional area below. Potential differences caused by the different contact are now removed, and no more differences, both in polysulfide (detectable as S_4^-) and in oxygenated product formation (detectable as PO_3^-), are expected. This is indeed the case as can be seen in Figure 5 where an overlay of NiO_2^-, S_4^-, and Cl^- represents the CAM, the SE, and the degradation products, respectively. Figure S4 shows the same representation but with PO_3^- as a degradation product, and Figure S2 shows the SEM image of the FIB cut. In this case as well, no difference is observed between the inner and outer regions of the sample.

Mass Spectrometry with High Mass Resolution. While ToF-SIMS provides fast and reliable results for the benchmarking of degradation in solid-state battery cathodes, it is difficult to assign all signals precisely to specific fragments. For example, the difference in the masses of O_2^- and S_2^- is very small with m/z = 31.989830 and m/z = 31.972072, respectively. Therefore, signals such as SO_2^- and S_2^- that have almost similar m/z ratios are hard to distinguish in ToF measurements due to the low mass resolution of approximately 6000. Furthermore, ToF-SIMS suffers from decreased resolution due to the roughness of the sample surface. In order to clearly identify all signals in the measurement, it is necessary to measure the sample with higher mass resolution. To achieve this, one sample was measured with OrbiTrap-SIMS. The OrbiTrap detector allows a much higher mass resolution of up to 10^5, making it possible to identify all the signals observed in ToF-SIMS unequivocally. Additionally, the mass resolution of OrbiTrap-SIMS is not decreased by the sample surface roughness. The mass interval list obtained from the OrbiTrap measurement was then applied to all ToF-SIMS measurements, which strongly improved the quality of the analyses. This difference is also highlighted in Figure S6 in the Supporting Information.

ToF-SIMS Analysis Results. *PCA.* Previous ToF-SIMS studies on solid-state composite cathodes relied on picking relevant fragments manually for analysis. While this approach generally works sufficiently well, principal component analysis (PCA) can be used to identify all relevant fragments for degradation more reliably. For this purpose, an uncycled and a cycled sample were used for PCA with eight measurements for each sample. As in this case, only two different samples were investigated, the data can, as expected, be explained mostly by one principal component as shown in Figure 6.

The scores of principal component 1 show a clear distinction between the cycled and uncycled sample. Measurements of the cycled sample showed positive values for PC1 and negative values for the uncycled sample. PC2 and higher do not show any correlation of the SIMS data of the cycled and uncycled

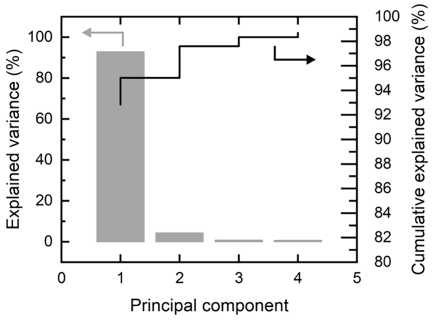

Figure 6. Variance and cumulative variance obtained by PCA performed on a cycled and uncycled cathode composite with uncoated CAM. As only two different samples were used, most of the variance in the data can be explained with one principal component. Most of the variance can be explained with only one principal component.

https://doi.org/10.1021/acsami.3c15723
ACS Appl. Mater. Interfaces 2024, 16, 9400−9413

sample. Therefore, only PC1 and PC2 are shown here in Figure 7. Scores for PC3 and PC4 can be found in Figure S5.

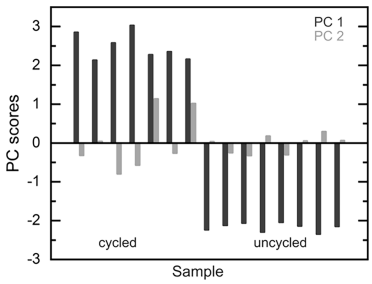

Figure 7. Scores for PC1 and PC2 for the cycled and uncycled sample. PC1 shows positive values for the cycled and negative values for the uncycled sample. The samples can be easily distinguished using PC1. PC2 shows no correlation between cycled and uncycled samples and can therefore not be used for distinction of the samples.

Because the scores for PC1 are clearly separated between the cycled and uncycled samples, the loadings of these PCs can be used to determine which fragments are indicative of degradation because the cycled samples are clearly more prone to degradation compared to the uncycled samples. Figure 8 shows the loadings for PC1 for the selected fragments.

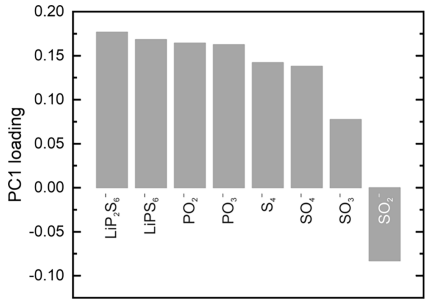

Figure 8. Loadings for PC1 are for selected fragments. The fragments with the highest loadings are shown as well as fragments that are commonly used to indicate degradation in cycled cathode composites.

The fragments with the highest loadings, namely, those fragments that are most indicative of degradation and other fragments that were used in previous studies, were chosen. A complete list can be found in Table S1. Some of the previously used fragments such as PO_2^-, PO_3^-, and S_4^- were found to be good indicators of degradation according to their PC1 loadings. However, further useful fragments could also be identified. SO_4^- can be used to identify oxygen related degradation, and $LiP_2S_6^-$ as well as $LiPS_6^-$ can be used to identify polysulfide formation. Moreover, other fragments such as SO_2^- can now be ruled out as indicators for degradation as the intensity of SO_2^- is actually inversely related to the presence of degradation products in the cathode composite.

PCA of Coated Samples. In addition to PCA of the uncycled and cycled sample, PCA was performed on all cycled samples as well. The goal here is to examine the coatings and try to find similarities and differences among the groups.

First, PCA was performed on the cycled (coated and uncoated) samples and the uncycled sample. The explained variance shown in Figure 9 indicates that at least over half of the data's variance is well explained with only one PC. At least

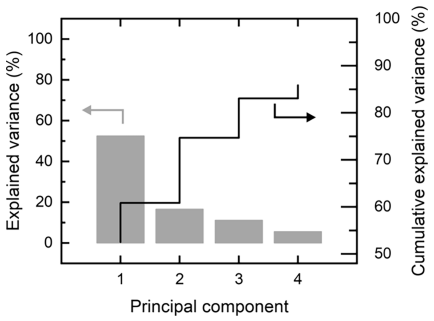

Figure 9. Explained variance of the PCA performed on cycled samples (coated and uncoated) and the uncoated sample. Multiple PCs are needed to explain the variance in the data.

three PCs are needed to describe the rest of the data sufficiently. The first PC separates the cycled sample from the uncycled sample, and the other PCs separate the cycled samples. Each sample forms a cluster, and PCA therefore allows grouping and separation of the cycled samples. The PC1 versus PC2 plots show this relation between the samples as shown in Figure 10. The higher PC versus PC can be found in Figures S7 and S8.

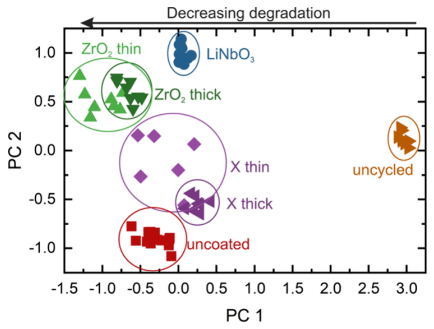

Figure 10. PCA of cycle-coated and uncoated samples. The strongest separation is present between the uncycled and cycled samples in PC1 as shown. The separations on PC2 are not as strong, but clustering of the different coatings is still observed on PC2. Plots for the other PCs can be found in Figures S7 and S8.

The loadings of this PCA shown in Figure S9 are very similar to the PCA performed with the uncycled and cycled (uncoated) samples only. To conclude, PC1 can be used as a general degradation marker. Here, a high score for PC1 is desirable as it indicates less degradation and a higher similarity to the uncycled sample. This allows scoring the performance of the coating in terms of degradation by simply evaluating the PC1 score. One can arbitrarily scale this score for better comparison, for example, here, the scores are scaled from 0 (for the uncycled sample) to 1 (for uncoated sample); therefore, low values in the degradation score are favorable over high values. The results of the overall degradation score are listed in Figure 11. These data show that not all coatings lead to less degradation and lower degradation scores. In this example, both CAMs coated with ZrO_2 actually lead to more

https://doi.org/10.1021/acsami.3c15723
ACS Appl. Mater. Interfaces 2024, 16, 9400−9413

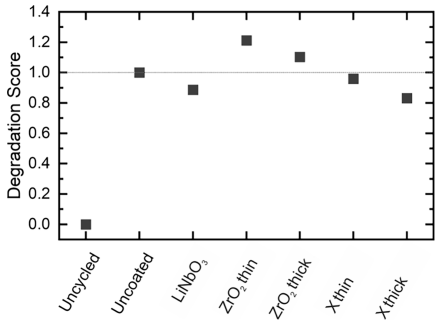

Figure 11. Degradation scores obtained from the PCA analysis of different samples. The values are scaled from 0 to 1, where 0 is assigned to the uncycled sample and 1 is assigned to the uncoated cycled sample. High values indicate high amounts of degradation and vice versa.

degradation compared to that of the uncoated sample. The best degradation score is obtained by the sample with the thick X coating and the $LiNbO_3$ coating. This degradation score, however, does not indicate which degradation pathway leads to higher or lower scores.

Detailed ToF-SIMS Analysis Results. While the PCA allows one to evaluate the samples in terms of degradation in general, further evaluation in terms of electrochemical and chemical degradation is not possible with PCA. For this purpose, the fragments require manual categorization. This categorization can be found in Table S2. With this categorization and the PCA results shown before, all fragments that are designated to a specific kind of degradation can be considered for evaluation instead of just taking a few representative fragments for quantification of degradation.

Here, two main pathways of degradation are considered. First, the electrochemical degradation leads to polysulfide formation. Fragments assigned to this pathway are labeled with "polysulfide" in Table S2. Second, chemical degradation leads to the formation of oxygenated sulfur and phosphorus compounds. Fragments assigned to these pathways are labeled with SO_y^- and PO_y^-. A detailed description of how the degradation scores are obtained is given in the Experimental Section.

The general degradation score shows stronger degradation for the $LiNbO_3$ and the ZrO_2 coatings, indicating higher amounts of degradation products for these samples. However, these values have to be interpreted with care. The PCA as applied here describes the data in terms of the highest variance when the intensity of each fragment is normalized to one. In other words, the fragments with the highest relative difference between the samples have the highest loading in PC1. PCA does not distinguish where this difference arises from. This is why further interpretation of the data is still necessary. In addition to the general degradation score, more specific degradation scores are introduced, namely, polysulfide degradation and sulfate and phosphate degradation scores. The fragments used for these degradation scores are chosen manually based on the chemical understanding of the cathode composite. Oxygenated sulfur compounds will lead to more fragments of the type $Li_{0/1}SO_x$, oxygenated phosphorus compounds will lead to fragments of the type $Li_{0/1}PO_x$, and polysulfide will lead to more fragments of the type $Li_{0/1}P_xS_y$.

Looking at the polysulfide formation in Figure 12b, it becomes clear why the ZrO_2 coatings have high general

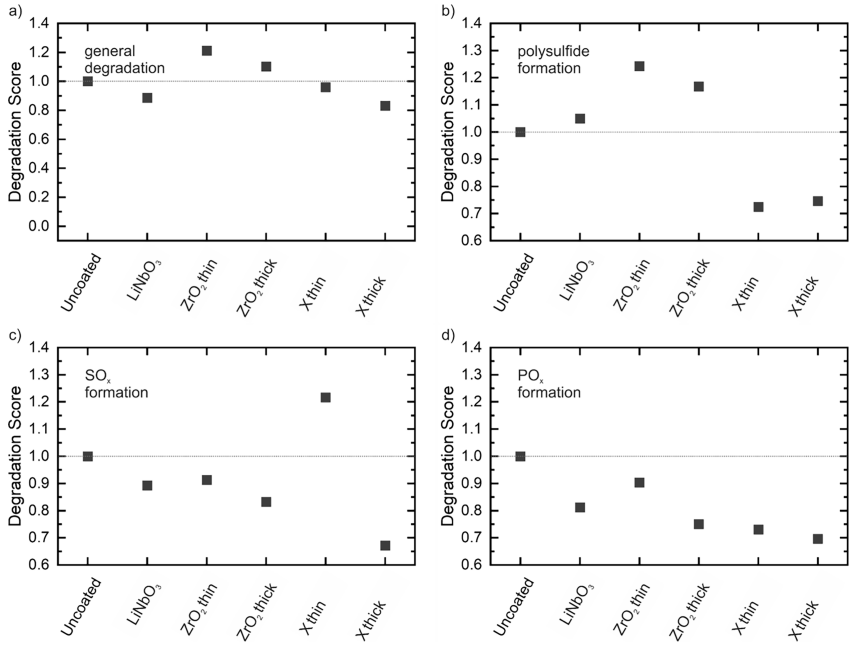

Figure 12. Specific degradation scores for specific degradation pathways. (a) Overall degradation score of the coatings. $LiNbO_3$ and ZrO_2 have higher degradation scores than the uncoated sample, indicating higher amounts of degradation. Only the X coatings show less overall degradation scores. (b) Polysulfide formation is suppressed in every coating except the thin X coating. (c, d) SO_x is suppressed in every coating except for the thin X coating, and PO_x formation is suppressed in every coating to different extents.

https://doi.org/10.1021/acsami.3c15723
ACS Appl. Mater. Interfaces 2024, 16, 9400−9413

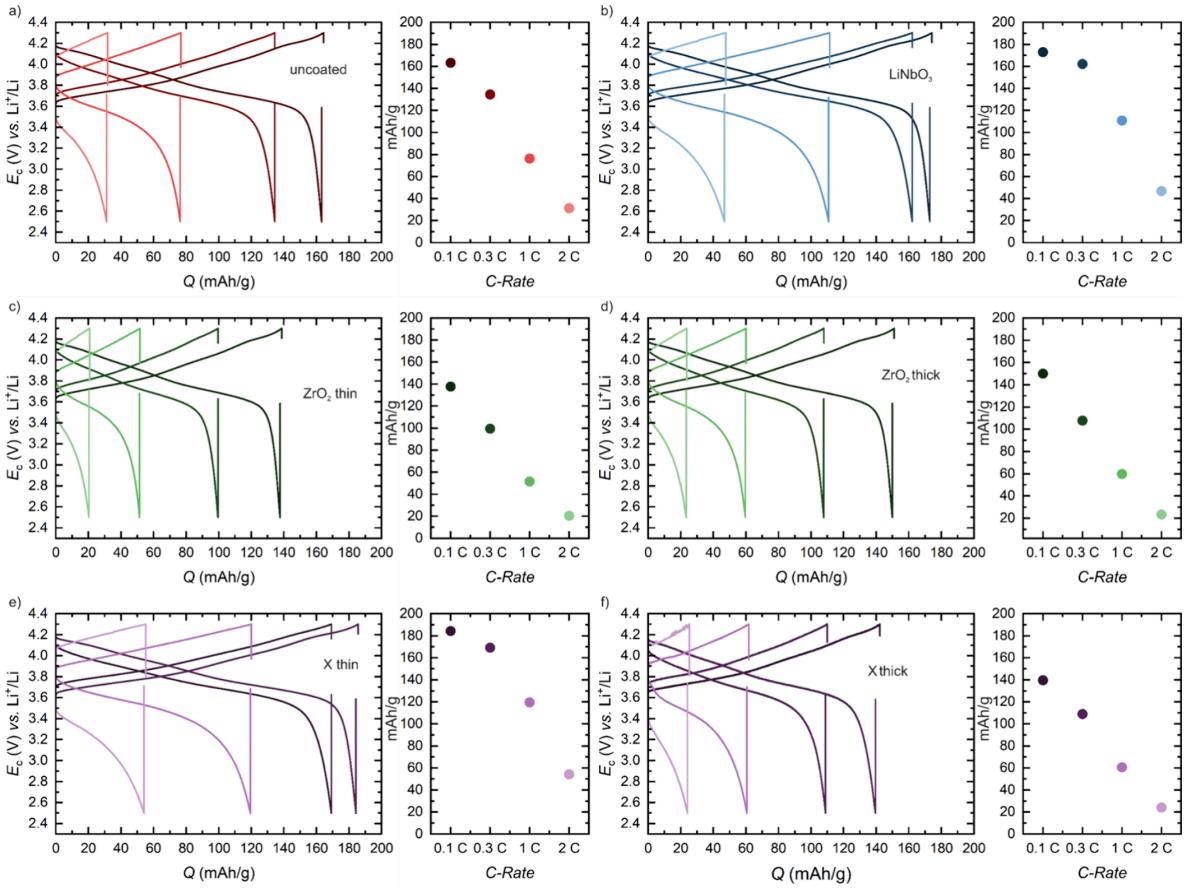

Figure 13. (a–f) Results of the rate tests performed on the different CAMs. The thin X (e) and $LiNbO_3$ coating (b) improve the electrochemical performance. The thick X coating (f) decreases the electrochemical performance despite showing good degradation results. The ZrO_2 (c, d) coatings decrease the electrochemical performance.

degradation scores. The polysulfide formation in these coatings is actually higher compared with the uncoated sample. The other coatings show slight ($LiNbO_3$) or substantial improvement (X) compared to the uncoated sample as shown in Figure 12. The increased or decreased polysulfide formation could be explained by the electronic partial conductivities (σ_{el}) of the respective coatings. According to Nakamura et al., a coating with a lower σ_{el} will protect the SE from electrochemical degradation while a coating with a higher σ_{el} will not protect the SE from electrochemical degradation.[52] The formation of oxygenated sulfur compounds is suppressed in every coating with the highest suppression being observed in the thick X sample. A similar trend is observed in the formation of oxygenated phosphorus compounds. The X coatings perform best, while all coatings reduce the amount of oxygenated phosphorus compounds.

Not surprising, in all degradation scores, the thick coatings show less degradation compared to their thin counterparts.

Rate Tests. Rate tests were performed for each active material in order to evaluate the electrochemical performance. The materials are compared with respect to their low-current (0.1 C) discharge capacity, their high-current (1.0 and 2.0 C) discharge capacity, and their capacity retention at high currents. Furthermore, the overpotential was measured (against a reference electrode). Uncoated NCM serves as a baseline measurement to which the other materials are then referenced.

Rate tests were performed to evaluate the kinetic performance of the coatings as well as the initial capacity they provide. The capacity retention at high currents (2.0 C) is used as a simple indicator for kinetic improvement or worsening of the CAM/SE system. Here, scores QS_0 and QS_{ret} are introduced for the initial capacity and the capacity retention at 2.0 C, respectively, to allow for a quick overview over the electrochemical performance of the CAM. Again, the values of the uncoated NCM serve as reference data and their scores for the initial capacity and capacity retention are set to 1. The values for the other CAMs are calculated relative to the uncoated material, cf. eqs 2 and 3.

$$QS_0 = \frac{\frac{Q_{0.1C}}{Q_{2C}}}{\frac{Q_{0.1C,uncoated}}{Q_{2C,uncoated}}} \quad (2)$$

$$QS_{ret} = \frac{Q_{ret}}{Q_{ret,uncoated}} \quad (3)$$

https://doi.org/10.1021/acsami.3c15723
ACS Appl. Mater. Interfaces 2024, 16, 9400−9413

ACS Applied Materials & Interfaces www.acsami.org Research Article

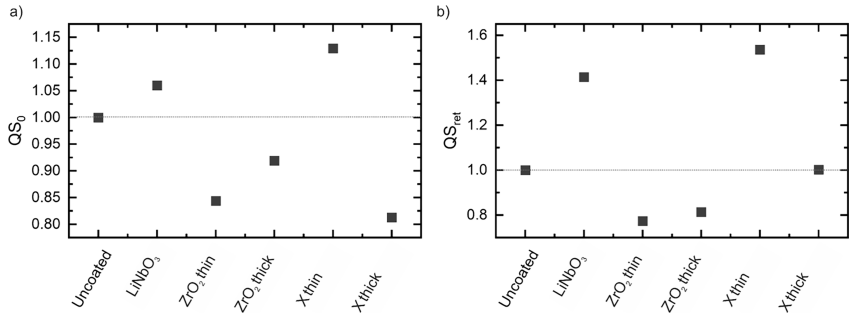

Figure 14. Scores for (a) initial capacity and (b) capacity retention at high currents. The ZrO_2-based coatings decrease electrochemical performance as well as the thick X coating. The other coatings, especially the thin X coating, led to an improvement in electrochemical performance.

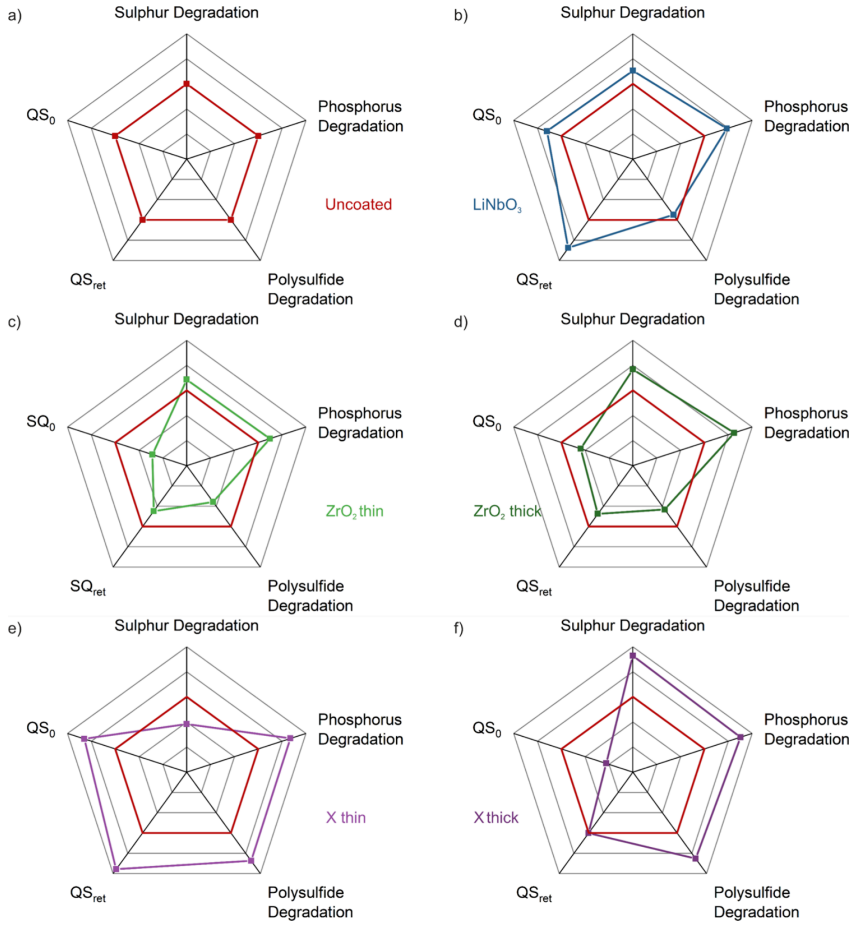

Figure 15. (a–f) Radar charts for the electrochemical and degradation performance of the CAMs used in this study. Only two coatings, namely, $LiNbO_3$ (b) and thin X (e), improve the electrochemical performance. The other coatings (c, d, f) do not lead to electrochemical performance improvements compared to the uncoated sample (a).

Out of the data given in Figure 13, the respective scores of QS_0 and QS_{ret} can be calculated. The results are shown in Figure 14. Only two coatings increase the initial capacity at 0.1 C, namely, $LiNbO_3$ and the thin X coating. The other coatings actually lead to a decrease in capacity. These results also highlight the importance of the thickness of the coating. For both the ZrO_2 and the X coating, the thick coating shows worse electrochemical performance probably due to the bad conductivity of the coating layer.

Radar Charts. The aforementioned results can be conveniently summarized in radar charts with each axis representing one score, resulting in a total of five axes/scores

https://doi.org/10.1021/acsami.3c15723
ACS Appl. Mater. Interfaces 2024, 16, 9400−9413

for each sample. The radar charts are presented such that values further from the middle represent favorable scores. Note that the scaling of these radar charts is arbitrarily chosen and that it can be adjusted to the specific needs of researchers working on similar benchmarking approaches.

Looking at the radar charts in Figure 15, it becomes immediately clear which coatings perform well and which coatings perform badly in different aspects.

SUMMARY AND CONCLUSIONS

In this study, a relatively fast and reliable way of benchmarking different coatings for CAMs in SSB is introduced based on the quantification of degradation products of the sulfide SE. First, the shortcomings of widespread techniques in the literature were discussed. In contrast to previous publications, the focus lies on getting reliable degradation and performance data instead of focusing only on certain aspects of the coating. Second, several coatings are compared, highlighting each of their advantages and disadvantages. Our study demonstrates how to utilize ToF-SIMS data effectively by using a PCA-based approach. This allows us to determine those fragments, namely, secondary ions, that are most relevant to quantify SE degradation as well as distinguish between different pathways of degradation. Using this approach, we found that some of the coatings do not mitigate degradation. Furthermore, we are able to determine which degradation pathway is actually responsible for the declining performance.

Second, precise electrochemical testing using three-electrode cells was performed. This allows for an accurate judgment of the kinetic capabilities of the different coatings. In fact, we found that not all coatings improve the performance. The X coatings reduced the degree of degradation for both the thick and thin coating layers. However, only the thin coating also improved the electrochemical performance. This highlights the need for systematic optimization of coating chemistries.

The approach presented here is widely applicable and can easily be adapted to other active materials and coating compositions. It relies on the high sensitivity and good spatial resolution of ToF-SIMS and thus cannot be achieved with other analytical techniques.

ASSOCIATED CONTENT

Supporting Information

The Supporting Information is available free of charge at https://pubs.acs.org/doi/10.1021/acsami.3c15723.

Additional ToF-SIMS large area scans, cross-sectional ToF-SIMS image, FIB-SEM image, Orbi-Trap vs ToF comparison, and additional PCA figures (PDF)

AUTHOR INFORMATION

Corresponding Author

Jürgen Janek − *Institute of Physical Chemistry, Justus Liebig University Giessen, D-35392 Giessen, Germany; Center for Materials Research (ZfM), Justus Liebig University Giessen, D-35392 Giessen, Germany; Battery and Electrochemistry Laboratory, Institute of Nanotechnology, Karlsruhe Institute of Technology (KIT), D-76344 Eggenstein-Leopoldshafen, Germany;* orcid.org/0000-0002-9221-47756; Email: juergen.janek@phys.chemie.uni-giessen.de

Authors

Jonas Hertle − *Institute of Physical Chemistry, Justus Liebig University Giessen, D-35392 Giessen, Germany; Center for Materials Research (ZfM), Justus Liebig University Giessen, D-35392 Giessen, Germany*

Felix Walther − *Institute of Physical Chemistry, Justus Liebig University Giessen, D-35392 Giessen, Germany; Center for Materials Research (ZfM), Justus Liebig University Giessen, D-35392 Giessen, Germany;* orcid.org/0000-0002-5843-4237

Teo Lombardo − *Institute of Physical Chemistry, Justus Liebig University Giessen, D-35392 Giessen, Germany; Center for Materials Research (ZfM), Justus Liebig University Giessen, D-35392 Giessen, Germany*

Christine Kern − *Institute of Physical Chemistry, Justus Liebig University Giessen, D-35392 Giessen, Germany; Center for Materials Research (ZfM), Justus Liebig University Giessen, D-35392 Giessen, Germany*

Boris Pavlovic − *Institute of Physical Chemistry, Justus Liebig University Giessen, D-35392 Giessen, Germany*

Boris Mogwitz − *Institute of Physical Chemistry, Justus Liebig University Giessen, D-35392 Giessen, Germany; Center for Materials Research (ZfM), Justus Liebig University Giessen, D-35392 Giessen, Germany*

Xiaohan Wu − *BASF SE, 67056 Ludwigshafen, Germany*

Holger Schneider − *BASF SE, 67056 Ludwigshafen, Germany;* orcid.org/0000-0002-8798-2961

Marcus Rohnke − *Institute of Physical Chemistry, Justus Liebig University Giessen, D-35392 Giessen, Germany; Center for Materials Research (ZfM), Justus Liebig University Giessen, D-35392 Giessen, Germany;* orcid.org/0000-0002-8867-950X

Complete contact information is available at: https://pubs.acs.org/10.1021/acsami.3c15723

Notes

The authors declare no competing financial interest.

ACKNOWLEDGMENTS

Financial support by BASF SE within the International Network for Batteries and Electrochemistry and by Bundesministerium für Bildung und Forschung (BMBF) within the projects PROGRAL (no. 03XP0427) and the Cluster of Competence for Solid State Batteries (no. 03XP0433D) is acknowledged. Many thanks to the DFG for funding the Hybrid-SIMS under Grant No. INST 162/544-1 FUGG.

REFERENCES

(1) Janek, J.; Zeier, W. G. A Solid Future for Battery Development. *Nat. Energy* **2016**, *1* (9), 16141.

(2) Kim, K. J.; Balaish, M.; Wadaguchi, M.; Kong, L.; Rupp, J. L. M. Solid-State Li−Metal Batteries: Challenges and Horizons of Oxide and Sulfide Solid Electrolytes and Their Interfaces. *Adv. Energy Mater.* **2021**, *11* (1), 1−63.

(3) Kim, M.-J.; Park, J.-W.; Kim, B. G.; Lee, Y.-J.; Ha, Y.-C.; Lee, S.-M.; Baeg, K.-J. Facile Fabrication of Solution-Processed Solid-Electrolytes for High-Energy-Density All-Solid-State-Batteries by Enhanced Interfacial Contact. *Sci. Rep.* **2020**, *10* (1), 11923.

(4) Yu, X.; Bates, J. B.; Jellison, G. E.; Hart, F. X. A Stable Thin-Film Lithium Electrolyte: Lithium Phosphorus Oxynitride. *J. Electrochem. Soc.* **1997**, *144* (2), 524−532.

(5) Seino, Y.; Takada, K.; Kim, B. C.; Zhang, L.; Ohta, N.; Wada, H.; Osada, M.; Sasaki, T. Synthesis of Phosphorous Sulfide Solid

https://doi.org/10.1021/acsami.3c15723
ACS Appl. Mater. Interfaces 2024, 16, 9400−9413

Electrolyte and All-Solid-State Lithium Batteries with Graphite Electrode. *Solid State Ionics* **2005**, *176* (31−34), 2389−2393.
(6) Bates, J. Thin-Film Lithium and Lithium-Ion Batteries. *Solid State Ionics* **2000**, *135* (1−4), 33−45.
(7) Zhang, W.; Weber, D. A.; Weigand, H.; Arlt, T.; Manke, I.; Schröder, D.; Koerver, R.; Leichtweiss, T.; Hartmann, P.; Zeier, W. G.; Janek, J. Interfacial Processes and Influence of Composite Cathode Microstructure Controlling the Performance of All-Solid-State Lithium Batteries. *ACS Appl. Mater. Interfaces* **2017**, *9* (21), 17835−17845.
(8) Koerver, R.; Aygün, I.; Leichtweiß, T.; Dietrich, C.; Zhang, W.; Binder, J. O.; Hartmann, P.; Zeier, W. G.; Janek, J. Capacity Fade in Solid-State Batteries: Interphase Formation and Chemomechanical Processes in Nickel-Rich Layered Oxide Cathodes and Lithium Thiophosphate Solid Electrolytes. *Chem. Mater.* **2017**, *29* (13), 5574−5582.
(9) Koerver, R.; Walther, F.; Aygün, I.; Sann, J.; Dietrich, C.; Zeier, W. G.; Janek, J. Redox-Active Cathode Interphases in Solid-State Batteries. *J. Mater. Chem. A* **2017**, *5* (43), 22750−22760.
(10) Kitsche, D.; Tang, Y.; Hemmelmann, H.; Walther, F.; Bianchini, M.; Kondrakov, A.; Janek, J.; Brezesinski, T. Atomic Layer Deposition Derived Zirconia Coatings on Ni-Rich Cathodes in Solid-State Batteries: Correlation Between Surface Constitution and Cycling Performance. *Small Sci.* **2023**, *3* (2), 2200073.
(11) Riegger, L. M.; Schlem, R.; Sann, J.; Zeier, W. G.; Janek, J. Lithium-Metal Anode Instability of the Superionic Halide Solid Electrolytes and the Implications for Solid-State Batteries. *Angew. Chemie Int. Ed.* **2021**, *60* (12), 6718−6723.
(12) Huo, H.; Janek, J. Silicon as Emerging Anode in Solid-State Batteries. *ACS Energy Lett.* **2022**, *7* (11), 4005−4016.
(13) Franco Gonzalez, A.; Yang, N.-H.; Liu, R.-S. Silicon Anode Design for Lithium-Ion Batteries: Progress and Perspectives. *J. Phys. Chem. C* **2017**, *121* (50), 27775−27787.
(14) Sharma, R. A.; Seefurth, R. N. Thermodynamic Properties of the Lithium-Silicon System. *J. Electrochem. Soc.* **1976**, *123* (12), 1763−1768.
(15) Beaulieu, L. Y.; Hatchard, T. D.; Bonakdarpour, A.; Fleischauer, M. D.; Dahn, J. R. Reaction of Li with Alloy Thin Films Studied by In Situ AFM. *J. Electrochem. Soc.* **2003**, *150* (11), A1457.
(16) Wilson, A.; Reimers, J.; Fuller, E.; Dahn, J. Lithium Insertion in Pyrolyzed Siloxane Polymers. *Solid State Ionics* **1994**, *74* (3−4), 249−254.
(17) Bianchini, M.; Roca-Ayats, M.; Hartmann, P.; Brezesinski, T.; Janek, J. There and Back Again—The Journey of LiNiO 2 as a Cathode Active Material. *Angew. Chemie Int. Ed.* **2019**, *58* (31), 10434−10458.
(18) Teo, J. H.; Strauss, F.; Walther, F.; Ma, Y.; Payandeh, S.; Scherer, T.; Bianchini, M.; Janek, J.; Brezesinski, T. The Interplay between (Electro)Chemical and (Chemo)Mechanical Effects in the Cycling Performance of Thiophosphate-Based Solid-State Batteries. *Mater. Futur.* **2022**, *1* (1), No. 015102.
(19) Bianchini, M.; Wang, J.; Clément, R.; Ceder, G. A First-Principles and Experimental Investigation of Nickel Solubility into the P2 Na x CoO 2 Sodium-Ion Cathode. *Adv. Energy Mater.* **2018**, *8* (26), 1801446 DOI: 10.1002/aenm.201801446.
(20) Bianchini, M.; Wang, J.; Clément, R. J.; Ouyang, B.; Xiao, P.; Kitchaev, D.; Shi, T.; Zhang, Y.; Wang, Y.; Kim, H.; Zhang, M.; Bai, J.; Wang, F.; Sun, W.; Ceder, G. The Interplay between Thermodynamics and Kinetics in the Solid-State Synthesis of Layered Oxides. *Nat. Mater.* **2020**, *19* (10), 1088−1095.
(21) Cronk, A.; Chen, Y.-T.; Deysher, G.; Ham, S.-Y.; Yang, H.; Ridley, P.; Sayahpour, B.; Nguyen, L. H. B.; Oh, J. A. S.; Jang, J.; Tan, D. H. S.; Meng, Y. S. Overcoming the Interfacial Challenges of LiFePO 4 in Inorganic All-Solid-State Batteries. *ACS Energy Lett.* **2023**, *8* (1), 827−835.
(22) Mertens, A.; Granwehr, J. Two-Dimensional Impedance Data Analysis by the Distribution of Relaxation Times. *J. Energy Storage* **2017**, *13*, 401−408.
(23) DeWees, R.; Wang, H. Synthesis and Properties of NaSICON-type LATP and LAGP Solid Electrolytes. *ChemSusChem* **2019**, *12* (16), 3713−3725.
(24) Kraft, M. A.; Ohno, S.; Zinkevich, T.; Koerver, R.; Culver, S. P.; Fuchs, T.; Senyshyn, A.; Indris, S.; Morgan, B. J.; Zeier, W. G. Inducing High Ionic Conductivity in the Lithium Superionic Argyrodites Li 6+ x P 1− x Ge x S 5 I for All-Solid-State Batteries. *J. Am. Chem. Soc.* **2018**, *140* (47), 16330−16339.
(25) Krauskopf, T.; Hartmann, H.; Zeier, W. G.; Janek, J. Toward a Fundamental Understanding of the Lithium Metal Anode in Solid-State Batteries—An Electrochemo-Mechanical Study on the Garnet-Type Solid Electrolyte Li 6.25 Al 0.25 La 3 Zr 2 O 12. *ACS Appl. Mater. Interfaces* **2019**, *11* (15), 14463−14477.
(26) Fuchs, T.; Mogwitz, B.; Otto, S.; Passerini, S.; Richter, F. H.; Janek, J. Working Principle of an Ionic Liquid Interlayer During Pressureless Lithium Stripping on Li 6.25 Al 0.25 La 3 Zr 2 O 12 (LLZO) Garnet-Type Solid Electrolyte. *Batter. Supercaps* **2021**, *4* (7), 1145−1155.
(27) Chen, R.; Li, Q.; Yu, X.; Chen, L.; Li, H. Approaching Practically Accessible Solid-State Batteries: Stability Issues Related to Solid Electrolytes and Interfaces. *Chem. Rev.* **2020**, *120* (14), 6820−6877.
(28) Tian, C.; Nordlund, D.; Xin, H. L.; Xu, Y.; Liu, Y.; Sokaras, D.; Lin, F.; Doeff, M. M. Depth-Dependent Redox Behavior of LiNi 0.6 Mn 0.2 Co 0.2 O 2. *J. Electrochem. Soc.* **2018**, *165* (3), A696−A704.
(29) Qiu, J.; Liu, X.; Chen, R.; Li, Q.; Wang, Y.; Chen, P.; Gan, L.; Lee, S.; Nordlund, D.; Liu, Y.; Yu, X.; Bai, X.; Li, H.; Chen, L. Enabling Stable Cycling of 4.2 V High-Voltage All-Solid-State Batteries with PEO-Based Solid Electrolyte. *Adv. Funct. Mater.* **2020**, *30* (22), 1−8.
(30) Xue, Z.; He, D.; Xie, X. Poly(Ethylene Oxide)-Based Electrolytes for Lithium-Ion Batteries. *J. Mater. Chem. A* **2015**, *3* (38), 19218−19253.
(31) Nair, J. R.; Imholt, L.; Brunklaus, G.; Winter, M. Lithium Metal Polymer Electrolyte Batteries: Opportunities and Challenges. *Electrochem. Soc. Interface* **2019**, *28* (2), 55−61.
(32) Hoffman, Z. J.; Shah, D. B.; Balsara, N. P. Temperature and Concentration Dependence of the Ionic Transport Properties of Poly(Ethylene Oxide) Electrolytes. *Solid State Ionics* **2021**, *370* (July), No. 115751.
(33) Deiseroth, H. J.; Kong, S. T.; Eckert, H.; Vannahme, J.; Reiner, C.; Zaiß, T.; Schlosser, M. Li6PS5X: A Class of Crystalline Li-Rich Solids with an Unusually High Li+ Mobility. *Angew. Chemie - Int. Ed.* **2008**, *47* (4), 755−758.
(34) Kamaya, N.; Homma, K.; Yamakawa, Y.; Hirayama, M.; Kanno, R.; Yonemura, M.; Kamiyama, T.; Kato, Y.; Hama, S.; Kawamoto, K.; Mitsui, A. A Lithium Superionic Conductor. *Nat. Mater.* **2011**, *10* (9), 682−686.
(35) Li, Y.; Song, S.; Kim, H.; Nomoto, K.; Kim, H.; Sun, X.; Hori, S.; Suzuki, K.; Matsui, N.; Hirayama, M.; Mizoguchi, T.; Saito, T.; Kamiyama, T.; Kanno, R. A Lithium Superionic Conductor for Millimeter-Thick Battery Electrode. *Science (80-.)* **2023**, *381* (6653), 50−53.
(36) Walther, F.; Koerver, R.; Fuchs, T.; Ohno, S.; Sann, J.; Rohnke, M.; Zeier, W. G.; Janek, J. Visualization of the Interfacial Decomposition of Composite Cathodes in Argyrodite-Based All-Solid-State Batteries Using Time-of-Flight Secondary-Ion Mass Spectrometry. *Chem. Mater.* **2019**, *31* (10), 3745−3755.
(37) Walther, F.; Strauss, F.; Wu, X.; Mogwitz, B.; Hertle, J.; Sann, J.; Rohnke, M.; Brezesinski, T.; Janek, J. The Working Principle of a Li 2 CO 3 /LiNbO 3 Coating on NCM for Thiophosphate-Based All-Solid-State Batteries. *Chem. Mater.* **2021**, *33* (6), 2110−2125.
(38) Ohta, N.; Takada, K.; Sakaguchi, I.; Zhang, L.; Ma, R.; Fukuda, K.; Osada, M.; Sasaki, T. LiNbO3-Coated LiCoO2 as Cathode Material for All Solid-State Lithium Secondary Batteries. *Electrochem. commun.* **2007**, *9* (7), 1486−1490.
(39) Ohta, N.; Takada, K.; Zhang, L.; Ma, R.; Osada, M.; Sasaki, T. Enhancement of the High-Rate Capability of Solid-State Lithium

https://doi.org/10.1021/acsami.3c15723
ACS Appl. Mater. Interfaces 2024, 16, 9400−9413

Batteries by Nanoscale Interfacial Modification. *Adv. Mater.* **2006**, *18* (17), 2226−2229.
(40) Culver, S. P.; Koerver, R.; Zeier, W. G.; Janek, J. On the Functionality of Coatings for Cathode Active Materials in Thiophosphate-Based All-Solid-State Batteries. *Adv. Energy Mater.* **2019**, *9* (24), 1900626.
(41) Zhang, Y. Q.; Tian, Y.; Xiao, Y.; Miara, L. J.; Aihara, Y.; Tsujimura, T.; Shi, T.; Scott, M. C.; Ceder, G. Direct Visualization of the Interfacial Degradation of Cathode Coatings in Solid State Batteries: A Combined Experimental and Computational Study. *Adv. Energy Mater.* **2020**, *10* (27), 1903778 DOI: 10.1002/aenm.201903778.
(42) Ito, Y.; Sakurai, Y.; Yubuchi, S.; Sakuda, A.; Hayashi, A.; Tatsumisago, M. Application of LiCoO 2 Particles Coated with Lithium Ortho-Oxosalt Thin Films to Sulfide-Type All-Solid-State Lithium Batteries. *J. Electrochem. Soc.* **2015**, *162* (8), A1610−A1616.
(43) Jung, S. H.; Oh, K.; Nam, Y. J.; Oh, D. Y.; Brüner, P.; Kang, K.; Jung, Y. S. Li 3 BO 3 − Li 2 CO 3: Rationally Designed Buffering Phase for Sulfide All-Solid-State Li-Ion Batteries. *Chem. Mater.* **2018**, *30* (22), 8190−8200.
(44) Woo, J. H.; Travis, J. J.; George, S. M.; Lee, S.-H. Utilization of Al 2 O 3 Atomic Layer Deposition for Li Ion Pathways in Solid State Li Batteries. *J. Electrochem. Soc.* **2015**, *162* (3), A344−A349.
(45) Moryson, Y.; Walther, F.; Sann, J.; Mogwitz, B.; Ahmed, S.; Burkhardt, S.; Chen, L.; Klar, P. J.; Volz, K.; Fearn, S.; Rohnke, M.; Janek, J. Analyzing Nanometer-Thin Cathode Particle Coatings for Lithium-Ion Batteries−The Example of TiO_2 on NCM622. *ACS Appl. Energy Mater.* **2021**, *4* (7), 7168−7181.
(46) Koerver, R.; Zhang, W.; de Biasi, L.; Schweidler, S.; Kondrakov, A. O.; Kolling, S.; Brezesinski, T.; Hartmann, P.; Zeier, W. G.; Janek, J. Chemo-Mechanical Expansion of Lithium Electrode Materials − on the Route to Mechanically Optimized All-Solid-State Batteries. *Energy Environ. Sci.* **2018**, *11* (8), 2142−2158.
(47) Hertle, J.; Walther, F.; Mogwitz, B.; Schröder, S.; Wu, X.; Richter, F. H.; Janek, J. Miniaturization of Reference Electrodes for Solid-State Lithium-Ion Batteries. *J. Electrochem. Soc.* **2023**, *170* (4), No. 040519.
(48) Lombardo, T.; Walther, F.; Kern, C.; Moryson, Y.; Weintraut, T.; Henss, A.; Rohnke, M. ToF-SIMS in Battery Research: Advantages, Limitations, and Best Practices. *J. Vac. Sci. Technol., A* **2023**, *41* (5), No. 053207, DOI: 10.1116/6.0002850.
(49) Lombardo, T. Https://Github.Com/Teolombardo/User-Friendly-Scripts-for-Experimental-Battery-Researchers.
(50) Bielefeld, A.; Weber, D. A.; Janek, J. Microstructural Modeling of Composite Cathodes for All-Solid-State Batteries. *J. Phys. Chem. C* **2019**, *123* (3), 1626−1634.
(51) Walther, F.; Randau, S.; Schneider, Y.; Sann, J.; Rohnke, M.; Richter, F. H.; Zeier, W. G.; Janek, J. Influence of Carbon Additives on the Decomposition Pathways in Cathodes of Lithium Thiophosphate-Based All-Solid-State Batteries. *Chem. Mater.* **2020**, *32* (14), 6123−6136.
(52) Nakamura, T.; Amezawa, K.; Kulisch, J.; Zeier, W. G.; Janek, J. Guidelines for All-Solid-State Battery Design and Electrode Buffer Layers Based on Chemical Potential Profile Calculation. *ACS Appl. Mater. Interfaces* **2019**, *11* (22), 19968−19976.

https://doi.org/10.1021/acsami.3c15723
ACS Appl. Mater. Interfaces 2024, 16, 9400−9413

4 Summary and Conclusion

In the beginning of this research thesis the stability issues of layered oxide CAMs and thiophosphate SEs have already been known.[137,202] Numerous research articles have been published about different coatings that improve the performance and stability of these systems. However, most research articles focused on comparing uncoated, i. e. not intentionally coated CAMs, to coated materials. Comparisons of different coatings were rarely reported and no common method for evaluating the performance of different CAMs was used or established. Furthermore, both rate-tests and long-term cycling tests were performed using 2-electrode setups exclusively. The anodes used for these tests are usually LTO or In/InLi due to their good stability and lack of dendrite formation. These electrodes, however, show significant impedance and they therefore introduce a large overpotential at higher current densities. A well established method to overcome this issue in electrochemistry is to use a reference electrode with a known potential. While this was well established a long time ago using liquid electrolytes, no work had been published in the beginning of this thesis. The first publication therefore tackled this issue and a way to use reference electrodes in SSBs. Besides proofing the concept of reference electrodes in SSBs the study shows that the rate performance of SSB cathodes is underestimated in a 2E setup. Large overpotentials are introduced and incomplete delithiation of $Li_7Ti_5O_{12}$ in LTO electrodes is another problem.

The second publication addressed the lack of comparability between different coatings and underdeveloped analytical techniques. ToF-SIMS analysis was used in combination with PCA to differentiate and semi-quantify different degradation pathways and products. Furthermore, previously established 3E cells were used to reliable determine the rate-capability of the different materials. This publication marks the first comparative evaluation of similarly performing coatings and provides a tool for future researchers in the field.

5 Outlook and future research possibilities

In order to match or even outperform state-of-the-art liquid-electrolyte LIBs the performance of SSB still needs to improve substantially. Thiophosphate based SSBs suffer from degradation both on the cathode and anode side.[63,81,82] While the degradation pathways are understood well at this point and a lot of different coating strategies have been published, to this day, the degradation issues have not been overcome. No reports of coatings with degradation suppressed to match LIBs. Especially the rate performance of solid-state cells lacks behind the performance of liquid cells. While liquid-based cathodes show excellent rate-capability, thiophosphate-based SSB consistently show worse rate-performance.[199,200] The cycling life of SSB is usually also worse compared to LIBs. Liquid cells can by cycled for up to 10 000 cycles. With SSBs this can be achieved as well, however, halide SEs are used which are very expensive.[5,201] Nonetheless, the performance of halide SEs is very promising and further research is warranted.

This thesis allows interested researchers to apply the findings presented herein to these systems. The 3E setup can be directly used in these systems. The benchmarking using ToF-SIMS can easily be transferred to these systems by performing an appropriate PCA analysis on ToF-SIMS measurements where these halide SEs are used in combination with CAMs and possibly other SEs and additives. The time-consuming manual analysis used in the past for new and unknown systems can be accelerated by using this approach.

6 Appendix

6.1 References

[1] Yoshino, A. *Angewandte Chemie - International Edition* **2012**, *51*, 5798–5800, DOI: doi:10.1002/anie.201105006. (Cited on page 1)

[2] Size of the global battery market from 2018 to 2021, with a forecast through 2030, by technology. https://www.statista.com/statistics/1339880/global-battery-market-size-by-technology/. (Cited on page 1)

[3] Estimated production capacity of tier 1 to 3 lithium-ion battery factories worldwide in 2018 with a forecast for 2023 and 2028. https://www.statista.com/statistics/1247625/global-production-capacity-of-lithium-ion-battery-factories/. (Cited on page 1)

[4] Blomgren, G. E. *Journal of The Electrochemical Society* **2017**, *164*, A5019–A5025, DOI: doi:10.1149/2.0251701jes. (Cited on page 1)

[5] Aiken, C. P.; Logan, E. R.; Eldesoky, A.; Hebecker, H.; Oxner, J. M.; Harlow, J. E.; Metzger, M.; Dahn, J. R. *Journal of The Electrochemical Society* **2022**, *169*, 050512, DOI: doi:10.1149/1945-7111/ac67b5. (Cited on pages 1, 13, and 61)

[6] Burns, J. C.; Kassam, A.; Sinha, N. N.; Downie, L. E.; Solnickova, L.; Way, B.; Dahn, J. R. *Journal of The Electrochemical Society* **2013**, *160*, A1451–A1456, DOI: doi:10.1149/2.060309jes. (Cited on page 1)

[7] International Energy Agency *World Energy Investment 2023*; World Energy Investment; OECD, 2023; DOI: doi:10.1787/e0e92e98-en. (Cited on page 1)

[8] Chalamala, B. No Title. https://www.osti.gov/biblio/1831370. (Cited on page 1)

[9] U.S. Department of Energy *U.S. Department of Energy* **2020**, *Technical*, 65. (Cited on page 1)

[10] Sullivan, J.; Deese, B. *Executive Order 14017: America's Supply Chain*; 2021; Vol. 86; pp 11849–11854. (Cited on page 1)

[11] Gravimetric energy density of different types of batteries in 2020. https://www.statista.com/statistics/1249539/gravimetric-energy-density-of-batteries/. (Cited on page 1)

[12] Aditya, J. P.; Ferdowsi, M. *2008 IEEE Vehicle Power and Propulsion Conference, VPPC 2008* **2008**, 1–6, DOI: doi:10.1109/VPPC.2008.4677500. (Cited on page 1)

[13] Chalamala, B. Energy Storage and the Electric Grid - Stabilizing the Renewable Energy Dominated Utility Grid Through Storage. Proposed for presentation at the Intersolar India 2021 conference (virtual) held December 10, 2020. 2020; DOI: doi:10.2172/1835230. (Cited on page 1)

[14] Mizushima, K.; Jones, P.; Wiseman, P.; Goodenough, J. *Materials Research Bulletin* **1980**, *15*, 783–789, DOI: doi:10.1016/0025-5408(80)90012-4. (Cited on pages 1 and 5)

[15] Whittingham, M. S. *Journal of The Electrochemical Society* **1976**, *123*, 315–320, DOI: doi:10.1149/1.2132817. (Cited on page 1)

[16] Godshall, N.; Raistrick, I.; Huggins, R. *Materials Research Bulletin* **1980**, *15*, 561–570, DOI: doi:10.1016/0025-5408(80)90135-X. (Cited on page 1)

[17] Yoshino, A.; Kenichi, S.; Takyuku, N. *US4668595 (A)* **1987**, (Cited on page 1)

[18] Janek, J.; Zeier, W. G. *Nature Energy* **2016**, *1*, 16141, DOI: doi:10.1038/nenergy.2016.141. (Cited on page 2)

[19] Lin, F.; Liu, Y.; Yu, X.; Cheng, L.; Singer, A.; Shpyrko, O. G.; Xin, H. L.; Tamura, N.; Tian, C.; Weng, T. C.; Yang, X. Q.; Meng, Y. S.; Nordlund, D.; Yang, W.; Doeff, M. M. *Chemical Reviews* **2017**, *117*, 13123–13186, DOI: doi:10.1021/acs.chemrev.7b00007. (Cited on page 2)

[20] Xu, J.; Cai, X.; Cai, S.; Shao, Y.; Hu, C.; Lu, S.; Ding, S. *Energy and Environmental Materials* **2023**, 1–26, DOI: doi:10.1002/eem2.12450. (Cited on page 2)

[21] Li, F.; Xu, J.; Hou, Z.; Li, M.; Yang, R. *ChemNanoMat* **2020**, *6*, 720–738, DOI: doi:10.1002/cnma.201900708. (Cited on page 2)

[22] Sharma, R. A.; Seefurth, R. N. *Journal of The Electrochemical Society* **1976**, *123*, 1763–1768, DOI: doi:10.1149/1.2132692. (Cited on page 2)

[23] Moyassari, E.; Roth, T.; Kücher, S.; Chang, C.-C.; Hou, S.-C.; Spingler, F. B.; Jossen, A. *Journal of The Electrochemical Society* **2022**, *169*, 010504, DOI: doi:10.1149/1945-7111/ac4545. (Cited on page 2)

[24] Tranchot, A.; Etiemble, A.; Thivel, P. X.; Idrissi, H.; Roué, L. *Journal of Power Sources* **2015**, *279*, 259–266, DOI: doi:10.1016/j.jpowsour.2014.12.126. (Cited on page 2)

[25] Ruther, R. E.; Hays, K. A.; An, S. J.; Li, J.; Wood, D. L.; Nanda, J. *ACS Applied Materials and Interfaces* **2018**, *10*, 18641–18649, DOI: doi:10.1021/acsami.8b02197. (Cited on page 2)

[26] Takeda, Y.; Yamamoto, O.; Imanishi, N. *Electrochemistry* **2016**, *84*, 210–218, DOI: doi:10.5796/electrochemistry.84.210. (Cited on page 2)

[27] Zhang, X.; Wang, A.; Liu, X.; Luo, J. *Accounts of Chemical Research* **2019**, *52*, 3223–3232, DOI: doi:10.1021/acs.accounts.9b00437. (Cited on page 2)

[28] Li, Y.; Song, S.; Kim, H.; Nomoto, K.; Kim, H.; Sun, X.; Hori, S.; Suzuki, K.; Matsui, N.; Hirayama, M.; Mizoguchi, T.; Saito, T.; Kamiyama, T.; Kanno, R. *Science* **2023**, *381*, 50–53, DOI: doi:10.1126/science.add7138. (Cited on pages 2 and 8)

[29] Culver, S. P.; Koerver, R.; Zeier, W. G.; Janek, J. *Advanced Energy Materials* **2019**, *1900626*, 1900626, DOI: doi:10.1002/aenm.201900626. (Cited on pages 2 and 14)

[30] Janek, J.; Zeier, W. G. *Nature Energy* **2023**, *8*, 230–240, DOI: doi:10.1038/s41560-023-01208-9. (Cited on page 5)

[31] Ober, S.; Mesnier, A.; Manthiram, A. *ACS Applied Materials & Interfaces* **2023**, *15*, 1442–1451, DOI: doi:10.1021/acsami.2c20268. (Cited on page 5)

[32] Louli, A. J.; Eldesoky, A.; DeGooyer, J.; Coon, M.; Aiken, C. P.; Simunovic, Z.;

Metzger, M.; Dahn, J. R. *Journal of The Electrochemical Society* **2022**, *169*, 040517, DOI: doi:10.1149/1945-7111/ac62c4. (Cited on page 5)

[33] Li, Q.; Yang, Y.; Yu, X.; Li, H. *Chinese Physics Letters* **2023**, DOI: doi:10.1088/0256-307x/40/4/048201. (Cited on page 5)

[34] Takada, K.; Inada, T.; Kajiyama, A.; Sasaki, H.; Kondo, S.; Watanabe, M.; Murayama, M.; Kanno, R. *Solid State Ionics* **2003**, *158*, 269–274, DOI: doi:10.1016/S0167-2738(02)00823-8. (Cited on page 5)

[35] Mizushima, K.; Jones, P.; Wiseman, P.; Goodenough, J. *Solid State Ionics* **1981**, *3-4*, 171–174, DOI: doi:10.1016/0167-2738(81)90077-1. (Cited on page 5)

[36] Xie, Q.; Cui, Z.; Manthiram, A. *Advanced Materials* **2021**, *33*, 1–14, DOI: doi:10.1002/adma.202100804. (Cited on pages 5 and 11)

[37] Yabuuchi, N.; Ohzuku, T. *Journal of Power Sources* **2003**, *119-121*, 171–174, DOI: doi:10.1016/S0378-7753(03)00173-3. (Cited on page 5)

[38] Patoux, S.; Doeff, M. M. *Electrochemistry Communications* **2004**, *6*, 767–772, DOI: doi:10.1016/j.elecom.2004.05.024. (Cited on page 5)

[39] Han, F.; Zhu, Y.; He, X.; Mo, Y.; Wang, C. *Advanced Energy Materials* **2016**, *6*, 1–9, DOI: doi:10.1002/aenm.201501590. (Cited on page 6)

[40] Yu, C.; van Eijck, L.; Ganapathy, S.; Wagemaker, M. *Electrochimica Acta* **2016**, *215*, 93–99, DOI: doi:10.1016/j.electacta.2016.08.081. (Cited on page 6)

[41] Auvergniot, J.; Cassel, A.; Foix, D.; Viallet, V.; Seznec, V.; Dedryvère, R. *Solid State Ionics* **2017**, *300*, 78–85, DOI: doi:10.1016/j.ssi.2016.11.029. (Cited on page 6)

[42] Takada, K. *Acta Materialia* **2013**, *61*, 759–770, DOI: doi:10.1016/j.actamat.2012.10.034. (Cited on page 6)

[43] Kim, T.; Kim, K.; Lee, S.; Song, G.; Jung, M. S.; Lee, K. T. *Chemistry of Materials* **2022**, *34*, 9159–9171, DOI: doi:10.1021/acs.chemmater.2c02106. (Cited on pages 6, 9, 10, and 11)

[44] Wang, S.; Wu, Y.; Ma, T.; Chen, L.; Li, H.; Wu, F. *ACS Nano* **2022**, *16*, 16158–16176, DOI: doi:10.1021/acsnano.2c04905. (Cited on pages 6 and 9)

[45] Rui, X.; Ren, D.; Liu, X.; Wang, X.; Wang, K.; Lu, Y.; Li, L.; Wang, P.; Zhu, G.; Mao, Y.; Feng, X.; Lu, L.; Wang, H.; Ouyang, M. **2023**, DOI: doi:10.1039/d3ee00084b. (Cited on page 6)

[46] Yu, X.; Chen, R.; Gan, L.; Li, H.; Chen, L. *Engineering* **2023**, *21*, 9–14, DOI: doi:10.1016/j.eng.2022.06.022. (Cited on page 6)

[47] Bates, A. M.; Preger, Y.; Torres-Castro, L.; Harrison, K. L.; Harris, S. J.; Hewson, J. *Joule* **2022**, *6*, 742–755, DOI: doi:10.1016/j.joule.2022.02.007. (Cited on page 6)

[48] Huang, W.; Feng, X.; Han, X.; Zhang, W.; Jiang, F. *Cell Reports Physical Science* **2021**, *2*, 100285, DOI: doi:10.1016/j.xcrp.2020.100285. (Cited on page 6)

[49] Rumble, J. *CRC Handbook of Chemistry and Physics*; CRC Press: Boca Raton, USA, 2023. (Cited on page 7)

[50] Ye, L. et al. *Angewandte Chemie - International Edition* **2019**, *58*, 2437–2442, DOI: doi:10.1002/anie.201814324. (Cited on page 7)

[51] Gao, X.; Zhou, Y. N.; Han, D.; Zhou, J.; Zhou, D.; Tang, W.; Goodenough, J. B. *Joule* **2020**, *4*, 1864–1879, DOI: doi:10.1016/j.joule.2020.06.016. (Cited on page 7)

[52] Xu, B.; Li, W.; Duan, H.; Wang, H.; Guo, Y.; Li, H.; Liu, H. *Journal of Power Sources* **2017**, *354*, 68–73, DOI: doi:10.1016/j.jpowsour.2017.04.026. (Cited on page 7)

[53] Foroozan, T.; Sharifi-Asl, S.; Shahbazian-Yassar, R. *Journal of Power Sources* **2020**, *461*, 228135, DOI: doi:10.1016/j.jpowsour.2020.228135. (Cited on page 7)

[54] Fuchs, T.; Mogwitz, B.; Otto, S. K.; Passerini, S.; Richter, F. H.; Janek, J. *Batteries and Supercaps* **2021**, *4*, 1145–1155, DOI: doi:10.1002/batt.202100015. (Cited on page 7)

[55] Fuchs, T.; Haslam, C. G.; Moy, A. C.; Lerch, C.; Krauskopf, T.; Sakamoto, J.; Richter, F. H.; Janek, J. *Advanced Energy Materials* **2022**, *12*, DOI: doi:10.1002/aenm.202201125. (Cited on pages 7 and 9)

[56] Krauskopf, T.; Hartmann, H.; Zeier, W. G.; Janek, J. *ACS Applied Materials & Interfaces* **2019**, *11*, 14463–14477, DOI: doi:10.1021/acsami.9b02537. (Cited on pages 7 and 9)

[57] Ohzuku, T.; Ueda, A.; Yamamoto, N. *Journal of The Electrochemical Society* **1995**, *142*, 1431–1435, DOI: doi:10.1149/1.2048592. (Cited on pages 7 and 8)

[58] Hertle, J.; Walther, F.; Mogwitz, B.; Schröder, S.; Wu, X.; Richter, F. H.; Janek, J. *Journal of The Electrochemical Society* **2023**, *170*, 040519, DOI: doi:10.1149/1945-7111/accb6f. (Cited on page 7)

[59] Xu, W.; Chen, X.; Wang, W.; Choi, D.; Ding, F.; Zheng, J.; Nie, Z.; Choi, Y. J.; Zhang, J. G.; Yang, Z. G. *Journal of Power Sources* **2013**, *236*, 169–174, DOI: doi:10.1016/j.jpowsour.2013.02.055. (Cited on page 7)

[60] Teo, J. H.; Strauss, F.; Walther, F.; Ma, Y.; Payandeh, S.; Scherer, T.; Bianchini, M.; Janek, J.; Brezesinski, T. *Materials Futures* **2022**, *1*, 015102, DOI: doi:10.1088/2752-5724/ac3897. (Cited on page 7)

[61] Mukai, K.; Kato, Y.; Nakano, H. *The Journal of Physical Chemistry C* **2014**, *118*, 2992–2999, DOI: doi:10.1021/jp412196v. (Cited on page 8)

[62] Strauss, F.; De Biasi, L.; Kim, A. Y.; Hertle, J.; Schweidler, S.; Janek, J.; Hartmann, P.; Brezesinski, T. *ACS Materials Letters* **2020**, *2*, 84–88, DOI: doi:10.1021/acsmaterialslett.9b00441. (Cited on page 8)

[63] Koerver, R.; Zhang, W.; de Biasi, L.; Schweidler, S.; Kondrakov, A. O.; Kolling, S.; Brezesinski, T.; Hartmann, P.; Zeier, W. G.; Janek, J. *Energy & Environmental Science* **2018**, *11*, 2142–2158, DOI: doi:10.1039/C8EE00907D. (Cited on pages 8, 13, and 61)

[64] Nam, J. S.; To A Ran, W.; Lee, S. H.; Vuong, T. H. L.; Jo, H.; Lee, J. H.; Hwang, S. M.; Kim, Y. J. *Energy Storage Materials* **2022**, *46*, 155–164, DOI: doi:10.1016/j.ensm.2022.01.015. (Cited on page 8)

[65] Bae Song, Y.; Kwak, H.; Cho, W.; Kim, K. S.; Seok Jung, Y.; Park, K. H. *Current Opinion in Solid State and Materials Science* **2022**, *26*, 100977, DOI: doi:10.1016/j.cossms.2021.100977. (Cited on page 8)

[66] Li, Q.; Cao, Y.; Yin, G.; Gao, Y. *Chemical Communications* **2020**, *56*, 15458–15461, DOI: doi:10.1039/d0cc01552k. (Cited on page 8)

[67] Santhosha, A. L.; Medenbach, L.; Buchheim, J. R.; Adelhelm, P. *Batteries and Supercaps* **2019**, *2*, 524–529, DOI: doi:10.1002/batt.201800149. (Cited on page 8)

[68] Sedlmeier, C.; Schuster, R.; Schramm, C.; Gasteiger, H. A. *Journal of The Electrochemical Society* **2023**, *170*, 030536, DOI: doi:10.1149/1945-7111/acc699. (Cited on page 8)

[69] Luo, S.; Wang, Z.; Li, X.; Liu, X.; Wang, H.; Ma, W.; Zhang, L.; Zhu, L.; Zhang, X. *Nature Communications* **2021**, *12*, DOI: doi:10.1038/s41467-021-27311-7. (Cited on page 8)

[70] Bielefeld, A.; Weber, D. A.; Janek, J. *Journal of Physical Chemistry C* **2019**, *123*, 1626–1634, DOI: doi:10.1021/acs.jpcc.8b11043. (Cited on pages 8 and 12)

[71] Mercier, R.; Malugani, J.-P.; Fahys, B.; Robert, G. *Solid State Ionics* **1981**, *5*, 663–666. (Cited on page 8)

[72] Mercier, R.; Malugani, J.-P.; Fahys, B.; Robert, G.; Douglade, J. *Acta Crystallographica Section B Structural Crystallography and Crystal Chemistry* **1982**, *38*, 1887–1890, DOI: doi:10.1107/s0567740882007535. (Cited on page 8)

[73] Tachez, M.; Malugani, J. P.; Mercier, R.; Robert, G. *Solid State Ionics* **1984**, *14*, 181–185, DOI: doi:10.1016/0167-2738(84)90097-3. (Cited on page 8)

[74] Murayama, M.; Kanno, R.; Irie, M.; Ito, S.; Hata, T.; Sonoyama, N.; Kawamoto, Y. *Journal of Solid State Chemistry* **2002**, *168*, 140–148, DOI: doi:10.1006/jssc.2002.9701. (Cited on page 8)

[75] Deiseroth, H. J.; Kong, S. T.; Eckert, H.; Vannahme, J.; Reiner, C.; Zaiß, T.; Schlosser, M. *Angewandte Chemie - International Edition* **2008**, *47*, 755–758, DOI: doi:10.1002/anie.200703900. (Cited on page 8)

[76] Kamaya, N.; Homma, K.; Yamakawa, Y.; Hirayama, M.; Kanno, R.; Yonemura, M.; Kamiyama, T.; Kato, Y.; Hama, S.; Kawamoto, K.; Mitsui, A. *Nature Materials* **2011**, *10*, 682–686, DOI: doi:10.1038/nmat3066. (Cited on page 8)

[77] Sakuda, A.; Hayashi, A.; Tatsumisago, M. *Scientific Reports* **2013**, *3*, 2–6, DOI: doi:10.1038/srep02261. (Cited on page 9)

[78] Park, K. H.; Bai, Q.; Kim, D. H.; Oh, D. Y.; Zhu, Y.; Mo, Y.; Jung, Y. S. *Advanced Energy Materials* **2018**, *8*, 1–24, DOI: doi:10.1002/aenm.201800035. (Cited on page 9)

[79] Wenzel, S.; Weber, D. A.; Leichtweiss, T.; Busche, M. R.; Sann, J.; Janek, J. *Solid State Ionics* **2016**, *286*, 24–33, DOI: doi:10.1016/j.ssi.2015.11.034. (Cited on page 9)

[80] Riegger, L. M.; Schlem, R.; Sann, J.; Zeier, W. G.; Janek, J. *Angewandte Chemie - International Edition* **2021**, *60*, 6718–6723, DOI: doi:10.1002/anie.202015238. (Cited on page 9)

[81] Riegger, L. M.; Mittelsdorf, S.; Fuchs, T.; Rueß, R.; Richter, F. H.; Janek, J. *Chemistry of Materials* **2023**, DOI: doi:10.1021/acs.chemmater.3c00676. (Cited on pages 9, 27, and 61)

[82] Walther, F.; Koerver, R.; Fuchs, T.; Ohno, S.; Sann, J.; Rohnke, M.; Zeier, W. G.;

Janek, J. *Chemistry of Materials* **2019**, DOI: doi:10.1021/acs.chemmater.9b00770. (Cited on pages 9, 12, 27, and 61)

[83] Walther, F.; Randau, S.; Schneider, Y.; Sann, J.; Rohnke, M.; Richter, F. H.; Zeier, W. G.; Janek, J. *Chemistry of Materials* **2020**, *32*, 6123–6136, DOI: doi:10.1021/acs.chemmater.0c01825. (Cited on pages 9 and 27)

[84] Walther, F.; Strauss, F.; Wu, X.; Mogwitz, B.; Hertle, J.; Sann, J.; Rohnke, M.; Brezesinski, T.; Janek, J. *Chemistry of Materials* **2021**, *33*, 2110–2125, DOI: doi:10.1021/acs.chemmater.0c04660. (Cited on pages 9 and 27)

[85] Camacho-Forero, L. E.; Balbuena, P. B. *Journal of Power Sources* **2018**, *396*, 782–790, DOI: doi:10.1016/j.jpowsour.2018.06.092. (Cited on page 9)

[86] Takada, K.; Ohno, T.; Ohta, N.; Ohnishi, T.; Tanaka, Y. *ACS Energy Letters* **2018**, *3*, 98–103, DOI: doi:10.1021/acsenergylett.7b01105. (Cited on page 9)

[87] Murugan, R.; Thangadurai, V.; Weppner, W. *Angewandte Chemie - International Edition* **2007**, *46*, 7778–7781, DOI: doi:10.1002/anie.200701144. (Cited on page 9)

[88] Takada, K. *Journal of Power Sources* **2018**, *394*, 74–85, DOI: doi:10.1016/j.jpowsour.2018.05.003. (Cited on page 9)

[89] Sharafi, A.; Meyer, H. M.; Nanda, J.; Wolfenstine, J.; Sakamoto, J. *Journal of Power Sources* **2016**, *302*, 135–139, DOI: doi:10.1016/j.jpowsour.2015.10.053. (Cited on page 9)

[90] Benabed, Y.; Rioux, M.; Rousselot, S.; Hautier, G.; Dollé, M. *Frontiers in Energy Research* **2021**, *9*, 1–13, DOI: doi:10.3389/fenrg.2021.682008. (Cited on page 9)

[91] Kataoka, K.; Akimoto, J. *Journal of the Ceramic Society of Japan* **2019**, *127*, 521–526, DOI: doi:10.2109/jcersj2.19022. (Cited on page 9)

[92] Li, X.; Jin, L.; Song, D.; Zhang, H.; Shi, X.; Wang, Z.; Zhang, L.; Zhu, L. *Journal of Energy Chemistry* **2020**, *40*, 39–45, DOI: doi:10.1016/j.jechem.2019.02.006. (Cited on page 9)

[93] Li, S.; Zhang, S.; Shen, L.; Liu, Q.; Ma, J.; Lv, W.; He, Y.; Yang, Q. *Advanced Science* **2020**, *7*, DOI: doi:10.1002/advs.201903088. (Cited on page 9)

[94] Rosenwinkel, M. P.; Schönhoff, M. *Journal of The Electrochemical Society* **2019**, *166*, A1977–A1983, DOI: doi:10.1149/2.0831910jes. (Cited on page 9)

[95] Hu, Z.; Li, G.; Wang, A.; Luo, J.; Liu, X. *Batteries and Supercaps* **2020**, *3*, 331–335, DOI: doi:10.1002/batt.201900191. (Cited on page 9)

[96] Seidl, L.; Grissa, R.; Zhang, L.; Trabesinger, S.; Battaglia, C. *Advanced Materials Interfaces* **2022**, *9*, 1–10, DOI: doi:10.1002/admi.202100704. (Cited on page 9)

[97] Steiner, H.-J.; Lutz, H. D. *Zeitschrift für anorganische und allgemeine Chemie* **1992**, *613*, 26–30, DOI: doi:10.1002/zaac.19926130104. (Cited on page 9)

[98] Asano, T.; Sakai, A.; Ouchi, S.; Sakaida, M.; Miyazaki, A.; Hasegawa, S. *Advanced Materials* **2018**, *30*, 1–7, DOI: doi:10.1002/adma.201803075. (Cited on page 9)

[99] Li, X. et al. *Energy and Environmental Science* **2019**, *12*, 2665–2671, DOI: doi:10.1039/c9ee02311a. (Cited on page 9)

[100] Park, K. H.; Kaup, K.; Assoud, A.; Zhang, Q.; Wu, X.; Nazar, L. F. *ACS Energy*

Letters **2020**, 533–539, DOI: doi:10.1021/acsenergylett.9b02599. (Cited on page 9)

[101] Liang, J.; Li, X.; Wang, S.; Adair, K. R.; Li, W.; Zhao, Y.; Wang, C.; Hu, Y.; Zhang, L.; Zhao, S.; Lu, S.; Huang, H.; Li, R.; Mo, Y.; Sun, X. *Journal of the American Chemical Society* **2020**, *142*, 7012–7022, DOI: doi:10.1021/jacs.0c00134. (Cited on page 9)

[102] Wang, S.; Bai, Q.; Nolan, A. M.; Liu, Y.; Gong, S.; Sun, Q.; Mo, Y. *Angewandte Chemie - International Edition* **2019**, *58*, 8039–8043, DOI: doi:10.1002/anie.201901938. (Cited on page 9)

[103] Bianchini, M.; Roca-Ayats, M.; Hartmann, P.; Brezesinski, T.; Janek, J. *Angewandte Chemie - International Edition* **2019**, DOI: doi:10.1002/anie.201812472. (Cited on page 10)

[104] Padhi, A. K.; Nanjundaswamy, K. S.; Goodenough, J. B. *Journal of The Electrochemical Society* **1997**, *144*, 1188–1194, DOI: doi:10.1149/1.1837571. (Cited on page 10)

[105] Tang, K.; Sun, J.; Yu, X.; Li, H.; Huang, X. *Electrochimica Acta* **2009**, *54*, 6565–6569, DOI: doi:10.1016/j.electacta.2009.06.030. (Cited on page 10)

[106] Cronk, A.; Chen, Y.-T.; Deysher, G.; Ham, S.-Y.; Yang, H.; Ridley, P.; Sayahpour, B.; Nguyen, L. H. B.; Oh, J. A. S.; Jang, J.; Tan, D. H. S.; Meng, Y. S. *ACS Energy Letters* **2023**, *8*, 827–835, DOI: doi:10.1021/acsenergylett.2c02138. (Cited on page 10)

[107] Laubach, S.; Laubach, S.; Schmidt, P. C.; Ensling, D.; Schmid, S.; Jaegermann, W.; Thißen, A.; Nikolowski, K.; Ehrenberg, H. *Physical Chemistry Chemical Physics* **2009**, *11*, 3278, DOI: doi:10.1039/b901200a. (Cited on page 10)

[108] Van Elp, J.; Wieland, J. L.; Eskes, H.; Kuiper, P.; Sawatzky, G. A.; De Groot, F. M.; Turner, T. S. *Physical Review B* **1991**, *44*, 6090–6103, DOI: doi:10.1103/PhysRevB.44.6090. (Cited on page 10)

[109] Zhou, F.; Cococcioni, M.; Marianetti, C. A.; Morgan, D.; Ceder, G. *Physical Review B - Condensed Matter and Materials Physics* **2004**, *70*, 1–8, DOI: doi:10.1103/PhysRevB.70.235121. (Cited on page 10)

[110] Wolverton, C.; Zunger, A. *Journal of The Electrochemical Society* **1998**, *145*, 2424–2431, DOI: doi:10.1149/1.1838653. (Cited on page 10)

[111] Knauth, P.; Mate, L.; Charles, C. S.; Cedex, C. M.; Tuller, H. L. **2002**, *80*, 1654–1680. (Cited on page 10)

[112] Arai, H.; Okada, S.; Ohtsuka, H.; Ichimura, M.; Yamaki, J. *Solid State Ionics* **1995**, *80*, 261–269, DOI: doi:10.1016/0167-2738(95)00144-U. (Cited on page 10)

[113] Kushida, K.; Kuriyama, K. *Solid State Communications* **2002**, *123*, 349–352, DOI: doi:10.1016/S0038-1098(02)00325-3. (Cited on page 10)

[114] Anisimov, V. I.; Zaanen, J.; Andersen, O. K. *Physical Review B* **1991**, *44*, 943–954, DOI: doi:10.1103/PhysRevB.44.943. (Cited on page 10)

[115] Orman, H. J.; Wiseman, P. J. *Acta Crystallographica Section C Crystal Structure Communications* **1984**, *40*, 12–14, DOI: doi:10.1107/S0108270184002833. (Cited on page 10)

[116] Hirakawa, K.; Kadowaki, H.; Ubukoshi, K. *Journal of the Physical Society of Japan* **1985**, *54*, 3526–3536, DOI: doi:10.1143/JPSJ.54.3526. (Cited on page 10)

[117] Ryu, H. H.; Park, K. J.; Yoon, C. S.; Sun, Y. K. *Chemistry of Materials* **2018**, *30*, 1155–1163, DOI: doi:10.1021/acs.chemmater.7b05269. (Cited on page 11)

[118] Cui, Z.; Manthiram, A. *Angewandte Chemie - International Edition* **2023**, *202307243*, DOI: doi:10.1002/anie.202307243. (Cited on page 11)

[119] Liu, X.; Xu, G. L.; Yin, L.; Hwang, I.; Li, Y.; Lu, L.; Xu, W.; Zhang, X.; Chen, Y.; Ren, Y.; Sun, C. J.; Chen, Z.; Ouyang, M.; Amine, K. *Journal of the American Chemical Society* **2020**, *142*, 19745–19753, DOI: doi:10.1021/jacs.0c09961. (Cited on page 11)

[120] Ruess, R.; Schweidler, S.; Hemmelmann, H.; Conforto, G.; Bielefeld, A.; Weber, D. A.; Sann, J.; Elm, M. T.; Janek, J. *Journal of The Electrochemical Society* **2020**, *167*, 100532, DOI: doi:10.1149/1945-7111/ab9a2c. (Cited on pages 11, 12, and 22)

[121] Amin, R.; Chiang, Y.-M. *Journal of The Electrochemical Society* **2016**, *163*, A1512–A1517, DOI: doi:10.1149/2.0131608jes. (Cited on page 12)

[122] Minnmann, P.; Quillman, L.; Burkhardt, S.; Richter, F. H.; Janek, J. *Journal of The Electrochemical Society* **2021**, *168*, 040537, DOI: doi:10.1149/1945-7111/abf8d7. (Cited on pages 12 and 22)

[123] Minnmann, P.; Strauss, F.; Bielefeld, A.; Ruess, R.; Adelhelm, P.; Burkhardt, S.; Dreyer, S. L.; Trevisanello, E.; Ehrenberg, H.; Brezesinski, T.; Richter, F. H.; Janek, J. *Advanced Energy Materials* **2022**, *2201425*, DOI: doi:10.1002/aenm.202201425. (Cited on pages 12 and 22)

[124] Strauss, F.; Bartsch, T.; De Biasi, L.; Kim, A. Y.; Janek, J.; Hartmann, P.; Brezesinski, T. *ACS Energy Letters* **2018**, *3*, 992–996, DOI: doi:10.1021/acsenergylett.8b00275. (Cited on page 12)

[125] Tornheim, A.; Sharifi-Asl, S.; Garcia, J. C.; Bareño, J.; Iddir, H.; Shahbazian-Yassar, R.; Zhang, Z. *Nano Energy* **2019**, *55*, 216–225, DOI: doi:10.1016/j.nanoen.2018.10.065. (Cited on page 12)

[126] Zhang, X.; Wang, Z.; Li, X.; Su, Y.; Ye, Z.; Zhang, L.; Huang, Q.; Tang, Y.; Huang, J. *Materials Horizons* **2023**, *10*, 1856–1864, DOI: doi:10.1039/d2mh01588a. (Cited on page 12)

[127] Koerver, R.; Walther, F.; Aygun, I.; Sann, J.; Dietrich, C.; Zeier, W. G.; Janek, J. *Journal of Materials Chemistry A* **2017**, *5*, 22750–22760, DOI: doi:10.1039/C7TA07641J. (Cited on pages 12 and 22)

[128] Koerver, R. Interface Phenomena and Chemo-Mechanical Effects in All-Solid-State Batteries. Ph.D. thesis, 2018. (Cited on page 12)

[129] Morino, Y.; Kanada, S. *Journal of Power Sources* **2021**, *509*, 230376, DOI: doi:10.1016/j.jpowsour.2021.230376. (Cited on page 12)

[130] Dewald, G. F.; Ohno, S.; Kraft, M. A.; Koerver, R.; Till, P.; Vargas-Barbosa, N. M.; Janek, J.; Zeier, W. G. *Chemistry of Materials* **2019**, *31*, 8328–8337, DOI: doi:10.1021/acs.chemmater.9b01550. (Cited on pages 12 and 13)

[131] La Mantia, F.; Rosciano, F.; Tran, N.; Novák, P. *Journal of Applied Electrochemistry* **2008**, *38*, 893–896, DOI: doi:10.1007/s10800-008-9491-9. (Cited on page 13)

[132] La Mantia, F.; Rosciano, F.; Tran, N.; Novák, P. *Journal of The Electrochemical Society* **2009**, *156*, A823, DOI: doi:10.1149/1.3205495. (Cited on page 13)

[133] Kim, A. Y.; Strauss, F.; Bartsch, T.; Teo, J. H.; Hatsukade, T.; Mazilkin, A.; Janek, J.; Hartmann, P.; Brezesinski, T. *Chemistry of Materials* **2019**, *31*, 9664–9672, DOI: doi:10.1021/acs.chemmater.9b02947. (Cited on pages 13, 15, 16, and 27)

[134] Harlow, J. E.; Ma, X.; Li, J.; Logan, E.; Liu, Y.; Zhang, N.; Ma, L.; Glazier, S. L.; Cormier, M. M. E.; Genovese, M.; Buteau, S.; Cameron, A.; Stark, J. E.; Dahn, J. R. *Journal of The Electrochemical Society* **2019**, *166*, A3031–A3044, DOI: doi:10.1149/2.0981913jes. (Cited on page 13)

[135] Bianchini, M.; Roca-Ayats, M.; Hartmann, P.; Brezesinski, T.; Janek, J. *Angewandte Chemie - International Edition* **2019**, DOI: doi:10.1002/anie.201812472. (Cited on page 13)

[136] Conforto, G.; Ruess, R.; Schröder, D.; Trevisanello, E.; Fantin, R.; Richter, F. H.; Janek, J. *Journal of The Electrochemical Society* **2021**, *168*, 070546, DOI: doi:10.1149/1945-7111/ac13d2. (Cited on pages 13 and 14)

[137] Ohta, N.; Takada, K.; Sakaguchi, I.; Zhang, L.; Ma, R.; Fukuda, K.; Osada, M.; Sasaki, T. *Electrochemistry Communications* **2007**, *9*, 1486–1490, DOI: doi:10.1016/j.elecom.2007.02.008. (Cited on pages 14, 31, and 59)

[138] Nakamura, T.; Amezawa, K.; Kulisch, J.; Zeier, W. G.; Janek, J. *ACS Applied Materials & Interfaces* **2019**, *11*, 19968–19976, DOI: doi:10.1021/acsami.9b03053. (Cited on pages 14 and 17)

[139] Morchhale, A.; Tang, Z.; Yu, C.; Farahati, R.; Kim, J. H. *Current Opinion in Electrochemistry* **2023**, *39*, 101251, DOI: doi:10.1016/j.coelec.2023.101251. (Cited on pages 14, 15, and 16)

[140] Lee, J. S.; Park, Y. J. *ACS Applied Materials and Interfaces* **2021**, *13*, DOI: doi:10.1021/acsami.1c10294. (Cited on pages 14 and 16)

[141] Kim, Y. J.; Rajagopal, R.; Kang, S.; Ryu, K. S. *Chemical Engineering Journal* **2020**, *386*, DOI: doi:10.1016/j.cej.2019.123975. (Cited on page 14)

[142] Deng, S. et al. *Energy Storage Materials* **2021**, *35*, 661–668, DOI: doi:10.1016/j.ensm.2020.12.003. (Cited on page 14)

[143] Li, X. et al. *ACS Energy Letters* **2019**, *4*, 2480–2488, DOI: doi:10.1021/acsenergylett.9b01676. (Cited on pages 15 and 16)

[144] Lim, C. B.; Park, Y. J. *Scientific Reports* **2020**, *10*, 1–12, DOI: doi:10.1038/s41598-020-67493-6. (Cited on page 15)

[145] Sun, Z.; Lai, Y.; Lv, N.; Hu, Y.; Li, B.; Jing, S.; Jiang, L.; Jia, M.; Li, J.; Chen, S.; Liu, F. *Advanced Materials Interfaces* **2021**, *8*, 1–8, DOI: doi:10.1002/admi.202100624. (Cited on page 15)

[146] Kwak, H. W.; Park, Y. J. *Thin Solid Films* **2018**, *660*, 625–630, DOI: doi:10.1016/j.tsf.2018.04.038. (Cited on page 15)

[147] Jung, S. H.; Oh, K.; Nam, Y. J.; Oh, D. Y.; Brüner, P.; Kang, K.; Jung, Y. S. *Chemistry of Materials* **2018**, *30*, 8190–8200, DOI: doi:10.1021/acs.chemmater.8b03321. (Cited on page 15)

[148] Zhang, Y. Q.; Tian, Y.; Xiao, Y.; Miara, L. J.; Aihara, Y.; Tsujimura, T.; Shi, T.; Scott, M. C.; Ceder, G. *Advanced Energy Materials* **2020**, *10*, DOI: doi:10.1002/aenm.201903778. (Cited on page 15)

[149] Yoon, D. H.; Park, Y. J. *Applied Energy* **2022**, *326*, 119991, DOI: doi:10.1016/j.apenergy.2022.119991. (Cited on page 15)

[150] Li, Z.; Wang, Z.; Miao, Y.; Ma, Y.; Zhang, H.; Shi, X.; Song, D.; Zhang, L.; Zhu, L. *Journal of Power Sources* **2022**, *541*, 231703, DOI: doi:10.1016/j.jpowsour.2022.231703. (Cited on page 15)

[151] Yi, J.; He, P.; Liu, H.; Ni, H.; Bai, Z.; Fan, L. Z. *Journal of Energy Chemistry* **2021**, *52*, 202–209, DOI: doi:10.1016/j.jechem.2020.03.057. (Cited on page 15)

[152] Fan, Z.; Xiang, J.; Yu, Q.; Wu, X.; Li, M.; Wang, X.; Xia, X.; Tu, J. *ACS Applied Materials and Interfaces* **2022**, *14*, 726–735, DOI: doi:10.1021/acsami.1c18264. (Cited on page 15)

[153] Cao, D.; Zhang, Y.; Nolan, A. M.; Sun, X.; Liu, C.; Sheng, J.; Mo, Y.; Wang, Y.; Zhu, H. *Nano Letters* **2020**, *20*, 1483–1490, DOI: doi:10.1021/acs.nanolett.9b02678. (Cited on page 15)

[154] Kitsche, D.; Strauss, F.; Tang, Y.; Bartnick, N.; Kim, A. Y.; Ma, Y.; Kübel, C.; Janek, J.; Brezesinski, T. *Batteries and Supercaps* **2022**, *5*, DOI: doi:10.1002/batt.202100397. (Cited on page 15)

[155] Okada, K.; Machida, N.; Naito, M.; Shigematsu, T.; Ito, S.; Fujiki, S.; Nakano, M.; Aihara, Y. *Solid State Ionics* **2014**, *255*, 120–127, DOI: doi:10.1016/j.ssi.2013.12.019. (Cited on page 15)

[156] Negi, R. S.; Yusim, Y.; Pan, R.; Ahmed, S.; Volz, K.; Takata, R.; Schmidt, F.; Henss, A.; Elm, M. T. *Advanced Materials Interfaces* **2022**, *9*, DOI: doi:10.1002/admi.202101428. (Cited on page 15)

[157] Kitsche, D.; Tang, Y.; Ma, Y.; Goonetilleke, D.; Sann, J.; Walther, F.; Bianchini, M.; Janek, J.; Brezesinski, T. *ACS Applied Energy Materials* **2021**, *4*, 7338–7345, DOI: doi:10.1021/acsaem.1c01487. (Cited on page 15)

[158] Sun, N.; Song, Y.; Liu, Q.; Zhao, W.; Zhang, F.; Ren, L.; Chen, M.; Zhou, Z.; Xu, Z.; Lou, S.; Kong, F.; Wang, J.; Tong, Y.; Wang, J. *Advanced Energy Materials* **2022**, *12*, 1–9, DOI: doi:10.1002/aenm.202200682. (Cited on page 15)

[159] Machida, N.; Kashiwagi, J.; Naito, M.; Shigematsu, T. *Solid State Ionics* **2012**, *225*, 354–358, DOI: doi:10.1016/j.ssi.2011.11.026. (Cited on page 15)

[160] Deng, S. et al. *Energy Storage Materials* **2020**, *27*, 117–123, DOI: doi:10.1016/j.ensm.2020.01.009. (Cited on pages 15 and 16)

[161] Li, X.; Jiang, Z.; Cai, D.; Wang, X.; Xia, X.; Gu, C.; Tu, J. *Small* **2021**, *17*, 1–8, DOI: doi:10.1002/smll.202103830. (Cited on page 15)

[162] Ito, Y.; Sakurai, Y.; Yubuchi, S.; Sakuda, A.; Hayashi, A.; Tatsumisago, M. *Journal of The Electrochemical Society* **2015**, *162*, A1610–A1616, DOI:

doi:10.1149/2.0771508jes. (Cited on page 15)

[163] Wu, E. A.; Jo, C.; Tan, D. H. S.; Zhang, M.; Doux, J.-M.; Chen, Y.-T.; Deysher, G.; Meng, Y. S. *Journal of The Electrochemical Society* **2020**, *167*, 130516, DOI: doi:10.1149/1945-7111/abb8b3. (Cited on page 15)

[164] Strauss, F.; Teo, J. H.; Maibach, J.; Kim, A.-Y.; Mazilkin, A.; Janek, J.; Brezesinski, T. *ACS Applied Materials & Interfaces* **2020**, *12*, 57146–57154, DOI: doi:10.1021/acsami.0c18590. (Cited on page 15)

[165] Nakamura, H.; Kawaguchi, T.; Masuyama, T.; Sakuda, A.; Saito, T.; Kuratani, K.; Ohsaki, S.; Watano, S. *Journal of Power Sources* **2020**, *448*, 227579, DOI: doi:10.1016/j.jpowsour.2019.227579. (Cited on page 15)

[166] Kwak, H. W.; Park, Y. J. *Scientific Reports* **2019**, *9*, 1–9, DOI: doi:10.1038/s41598-019-44629-x. (Cited on page 15)

[167] Deng, S. et al. *ACS Energy Letters* **2020**, *5*, 1243–1251, DOI: doi:10.1021/acsenergylett.0c00256. (Cited on pages 15 and 17)

[168] Shi, B. X.; Yusim, Y.; Sen, S.; Demuth, T.; Ruess, R.; Volz, K.; Henss, A.; Richter, F. H. *Advanced Energy Materials* **2023**, *13*, 1–13, DOI: doi:10.1002/aenm.202300310. (Cited on pages 16 and 17)

[169] Shrestha, S.; Carpenter, C.; Kim, J.; Jeong, J.; Lee, H. J.; Kim, S. C.; Hah, H. J.; Song, M.-S.; Oh, K.; Lee, S.-H. *Journal of The Electrochemical Society* **2022**, *169*, 060541, DOI: doi:10.1149/1945-7111/ac79d2. (Cited on page 16)

[170] Liang, Y.; Liu, H.; Wang, G.; Wang, C.; Li, D.; Ni, Y.; Fan, L. Z. *Advanced Energy Materials* **2022**, *12*, 1–13, DOI: doi:10.1002/aenm.202201555. (Cited on page 16)

[171] Strauss, F.; Stepien, D.; Maibach, J.; Pfaffmann, L.; Indris, S.; Hartmann, P.; Brezesinski, T. *RSC Advances* **2019**, *10*, 1114–1119, DOI: doi:10.1039/c9ra10253a. (Cited on page 16)

[172] Zuo, T. T.; Walther, F.; Ahmed, S.; Rueß, R.; Hertle, J.; Mogwitz, B.; Volz, K.; Janek, J. *ACS Energy Letters* **2023**, *8*, 1322–1329, DOI: doi:10.1021/acsenergylett.2c02835. (Cited on pages 16 and 17)

[173] Strauss, F.; Payandeh, S.; Kondrakov, A.; Brezesinski, T. *Materials Futures* **2022**, *1*, DOI: doi:10.1088/2752-5724/ac5b7d. (Cited on page 16)

[174] Rosenbach, C.; Walther, F.; Ruhl, J.; Hartmann, M.; Hendriks, T. A.; Ohno, S.; Janek, J.; Zeier, W. G. *Advanced Energy Materials* **2023**, *13*, 1–9, DOI: doi:10.1002/aenm.202203673. (Cited on page 17)

[175] Schönleber, M.; Klotz, D.; Ivers-Tiffée, E. *Electrochimica Acta* **2014**, *131*, 20–27, DOI: doi:10.1016/j.electacta.2014.01.034. (Cited on page 19)

[176] Klotz, D.; Schönleber, M.; Schmidt, J. P.; Ivers-Tiffée, E. *Electrochimica Acta* **2011**, *56*, 8763–8769, DOI: doi:10.1016/j.electacta.2011.07.096. (Cited on page 19)

[177] Irvine, J. T.; Sinclair, D. C.; West, A. R. *Advanced Materials* **1990**, *2*, 132–138, DOI: doi:10.1002/adma.19900020304. (Cited on page 21)

[178] Zuo, T. T.; Rueß, R.; Pan, R.; Walther, F.; Rohnke, M.; Hori, S.; Kanno, R.; Schröder, D.; Janek, J. *Nature Communications* **2021**, *12*, DOI: doi:10.1038/s41467-021-26895-4. (Cited on page 22)

[179] Braun, P.; Uhlmann, C.; Weiss, M.; Weber, A.; Ivers-Tiffée, E. *Journal of Power Sources* **2018**, *393*, 119–127, DOI: doi:https://doi.org/10.1016/j.jpowsour.2018.04.111. (Cited on page 22)

[180] Peres, P.; Merkulov, A.; Desse, F.; Schuhmacher, M. *Surface and Interface Analysis* **2011**, *43*, 643–645, DOI: doi:10.1002/sia.3525. (Cited on page 27)

[181] Gnaser, H. *Surface and Interface Analysis* **1997**, *25*, 737–740, DOI: doi:10.1002/(SICI)1096-9918(199709)25:10<737::AID-SIA294>3.0.CO;2-M. (Cited on page 27)

[182] Strohmeier, B. R. *Surface and Interface Analysis* **1990**, *15*, 51–56, DOI: doi:10.1002/sia.740150109. (Cited on page 27)

[183] Carlson, T. A.; McGuire, G. *Journal of Electron Spectroscopy and Related Phenomena* **1972**, *1*, 161–168, DOI: doi:10.1016/0368-2048(72)80029-X. (Cited on page 27)

[184] Wenzel, S.; Randau, S.; Leichtweiß, T.; Weber, D. A.; Sann, J.; Zeier, W. G.; Janek, J. *Chemistry of Materials* **2016**, *28*, 2400–2407, DOI: doi:10.1021/acs.chemmater.6b00610. (Cited on page 27)

[185] Shard, A. G. *Surface and Interface Analysis* **2014**, *46*, 175–185, DOI: doi:10.1002/sia.5406. (Cited on page 28)

[186] Ohta, N.; Takada, K.; Zhang, L.; Ma, R.; Osada, M.; Sasaki, T. *Advanced Materials* **2006**, *18*, 2226–2229, DOI: doi:10.1002/adma.200502604. (Cited on page 31)

[187] Ikezawa, A.; Fukunishi, G.; Okajima, T.; Kitamura, F.; Suzuki, K.; Hirayama, M.; Kanno, R.; Arai, H. *Electrochemistry Communications* **2020**, *116*, 106743, DOI: doi:10.1016/j.elecom.2020.106743. (Cited on page 33)

[188] Nam, Y. J.; Park, K. H.; Oh, D. Y.; An, W. H.; Jung, Y. S. *Journal of Materials Chemistry A* **2018**, *6*, 14867–14875, DOI: doi:10.1039/c8ta03450h. (Cited on page 33)

[189] Chang, G. H.; Choi, H. U.; Kang, S.; Park, J. Y.; Lim, H. T. *Ionics* **2020**, *26*, 1555–1561, DOI: doi:10.1007/s11581-019-03367-w. (Cited on page 33)

[190] Zaman, W.; Zhao, L.; Martin, T.; Zhang, X.; Wang, Z.; Wang, Q. J.; Harris, S.; Hatzell, K. B. *ACS Applied Materials & Interfaces Interfaces* **2023**, *15*, 37401–37409, DOI: doi:10.1021/acsami.3c05886. (Cited on page 33)

[191] Fukunishi, G.; Ikezawa, A.; Okajima, T.; Kitamura, F.; Suzuki, K.; Hirayama, M.; Kanno, R.; Arai, H. *ACS Applied Energy Materials* **2023**, *6*, 10908–10917, DOI: doi:10.1021/acsaem.3c01656. (Cited on page 33)

[192] Fukunishi, G.; Tabuchi, M.; Ikezawa, A.; Okajima, T.; Kitamura, F.; Suzuki, K.; Hirayama, M.; Kanno, R.; Arai, H. *Journal of Power Sources* **2023**, *564*, 232864, DOI: doi:10.1016/j.jpowsour.2023.232864. (Cited on page 33)

[193] Goodwin, L. E.; Till, P.; Bhardwaj, M.; Nazer, N.; Adelhelm, P.; Tietz, F.; Zeier, W. G.; Richter, F. H.; Janek, J. *ACS Applied Materials & Interfaces* **2023**, *15*, 50457–50468, DOI: doi:10.1021/acsami.3c09256. (Cited on page 33)

[194] Spencer, J. D.; Perera, J.; Pu, S. D.; Melvin, D. L.; Adamson, P.; Bruce, P. G. *Journal of Solid State Electrochemistry* **2022**, *26*, 1961–1968, DOI: doi:10.1007/s10008-022-05225-8. (Cited on page 33)

[195] Bruce, P. G.; Evans, J.; Vincent, C. A. *Solid State Ionics* **1987**, *25*, 255–262, DOI: doi:10.1016/0167-2738(87)90189. (Cited on page 33)

[196] Arai, H.; Kunisaki, T.; Shimzu, Y.; Seiyama, T. *Solid State Ionics* **1986**, *20*, 241, DOI: doi:10.1016/0167-2738. (Cited on page 33)

[197] Chiang, C. K.; Davis, G. T.; Harding, C. A.; Aarons, J. *Solid State Ionics* **1983**, *10*, 1121–1124. (Cited on page 33)

[198] Hertle, J.; Walther, F.; Lombardo, T.; Kern, C.; Pavlovic, B.; Mogwitz, B.; Wu, X.; Schneider, H.; Rohnke, M.; Janek, J. *ACS Applied Materials & Interfaces* **2024**, *16*, 9400–9413, DOI: doi:10.1021/acsami.3c15723. (Cited on page 43)

[199] Li, G.; Feng, Y.; Zhu, J.; Mo, C.; Cai, Q.; Liao, Y.; Li, W. *ACS Applied Materials & Interfaces* **2022**, *14*, 36656–36667, DOI: doi:10.1021/acsami.2c09103. (Cited on page 61)

[200] Li, X.; Jin, L.; Song, D.; Zhang, H.; Shi, X.; Wang, Z.; Zhang, L.; Zhu, L. *Journal of Energy Chemistry* **2020**, *40*, 39–45, DOI: doi:10.1016/j.jechem.2019.02.006. (Cited on page 61)

[201] Ma, T.; Wang, Z.; Wu, D.; Lu, P.; Zhu, X.; Yang, M.; Peng, J.; Chen, L.; Li, H.; Wu, F. *Energy and Environmental Science* **2023**, 2142–2152, DOI: doi:10.1039/d3ee00420a. (Cited on page 61)

[202] Chen, S.; Xie, D.; Liu, G.; Mwizerwa, J. P.; Zhang, Q.; Zhao, Y.; Xu, X.; Yao, X. *Energy Storage Materials* **2018**, *14*, 58–74, DOI: doi:10.1016/j.ensm.2018.02.020. (Cited on page 59)

6.2 Publication I – Supplementary Information

Supplementary Information

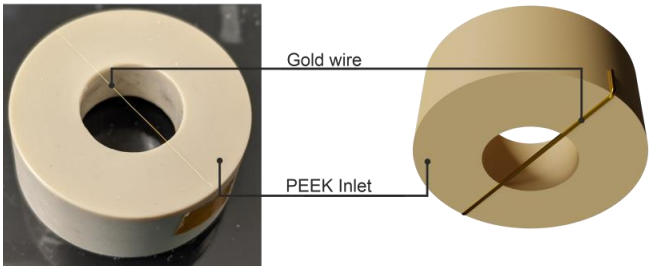

Figure S1: *Positioning of the μ-RE. The gold wire is attached to the PEEK inlet with KAPTON tape providing a linear RE spanning the whole diameter of the separator.*

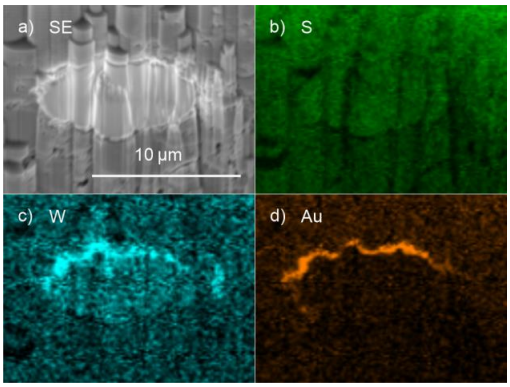

Figure S2*: EDS images of the lithiated gold-wire embedded in the solid electrolyte matrix. The gold wire is visible in the middle as a bright spot. a) Secondary-electron image. The morphology created by the FIB commonly referred to as curtaining is well visible. b) Sulphur EDS is showing a homogenous distribution. c) The tungsten EDS is only showing a significant signal at the top of the gold wire. d) The gold EDS only shows a significant signal on the top as well.*

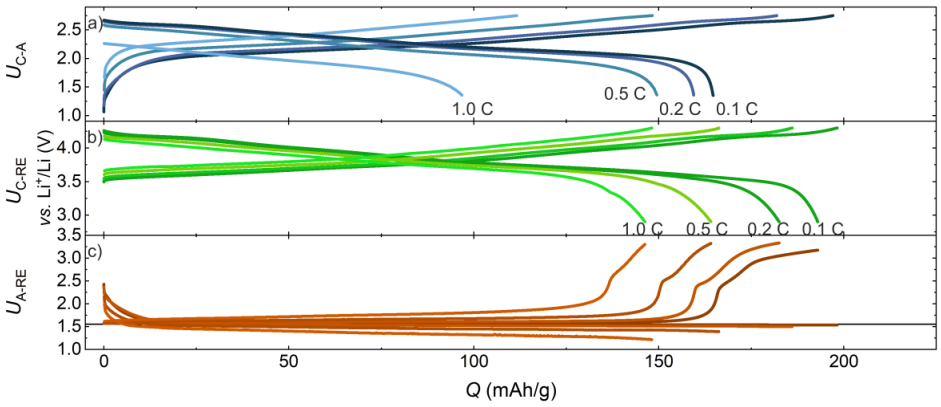

Figure S3: *Detailed rate rest as described in figure* ***Error! Reference source not found.*** *showing charge and discharge curves for 0.2 and 0.5 additionally. a) Charge/discharge curves for the 2E setup. b) Charge/discharge curves for the cathode in the 3E setup. c) Charge/discharge curves for the anode in the 3E setup.*

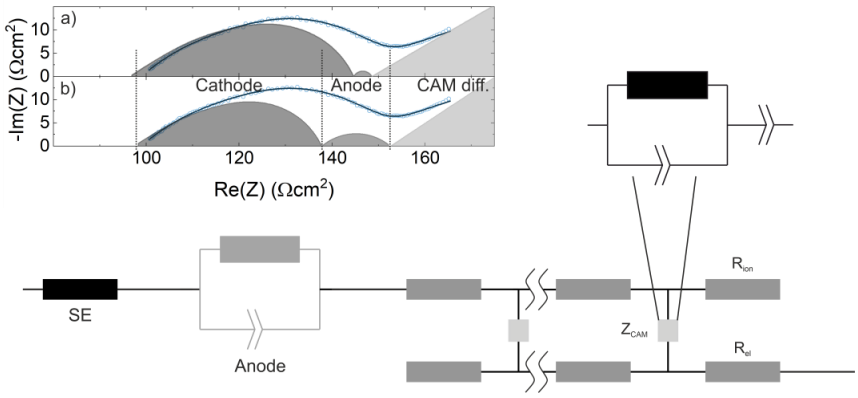

Figure S4: *Equivalent circuit used for fitting impedance data shown in figure* ***Error! Reference source not found.****. The solid separator is fitted with a resistor. The anode is fitted with an (R)(CPE) element. The cathode is fitted with a Z-type TLM where the ion conducting pathway and the electron conducting pathway are both fitted with resistors* R_{ion} *and* R_{el}*, respectively. The interface is modelled with an (R)(CPE)-CPE element modelling the charge-transfer and the diffusion in the active material.*

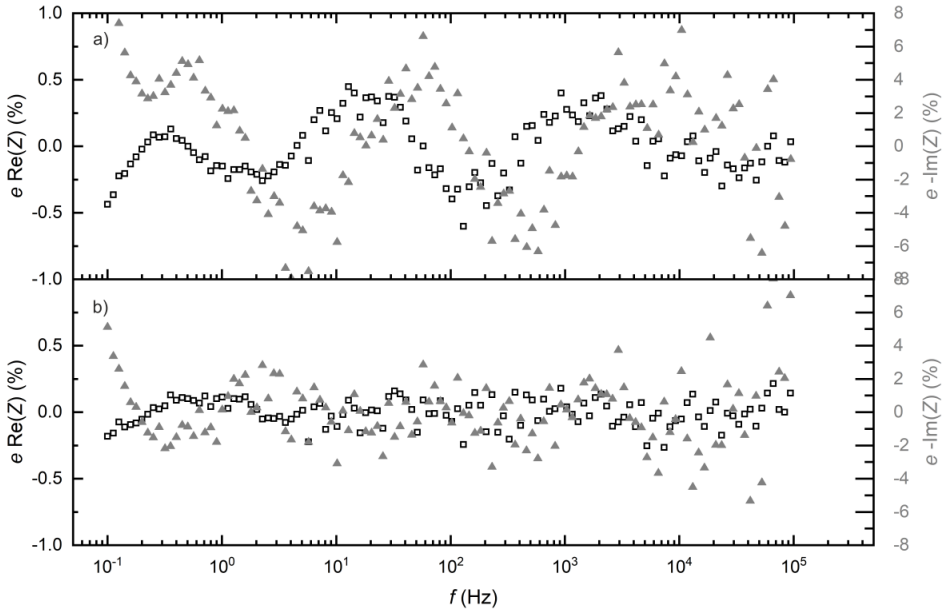

Figure S5: *Residuals* e *of the fits shown in figure* ***Error! Reference source not found.****. The residuals for both fits are below 1 % for Re(Z) and below 5 % for -Im(Z). a) Residuals corresponding to impedance data and fit in figure* ***Error! Reference source not found.****a). b) Residuals corresponding to impedance data and fit in figure* ***Error! Reference source not found.****b).*

Table S1: *Fit parameters for a 2E impedance measurement. The fit parameters are ambiguous due to the overlap of anode and cathode contributions. The element Z_{CAM} is comprised of the element (R)(CPE)-CPE.*

	Parameter	Fit 1	Fit 2
SE separator	R_{SE} (Ωcm^2)	98	97
Anode	R_{Anode} (Ωcm^2)	14	3.9
	Q_{Anode} (Ωs^{α})	$4.49*10^{-2}$	$3.3*10^{-2}$
	α_{Anode}	0.60	0.68
Cathode	R_{ion} (Ωcm^2)	$9.07*10^{3}$	$12.6*10^{3}$
	R_{CAM} (Ωcm^2)	0.24	0.27
	Q_{CAM} (Ωs^{α})	$3.87*10^{-2}$	$5.18*10^{-2}$
	α_{CAM} (Ωcm^2)	0.74	0.73
	Q_{diff} (Ωs^{α})	9.07	7.66
	α_{diff}	0.45	0.37

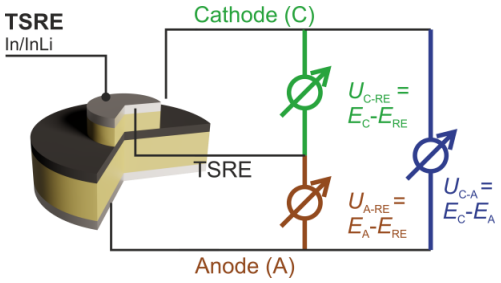

***Figure S6**: Cell connection for the TSRE setup. The TSRE is used as pseudo-reference electrode allowing separation of cathode ($U_{C\text{-}RE}$), anode ($U_{A\text{-}RE}$) and full cell voltages ($U_{C\text{-}A}$).*

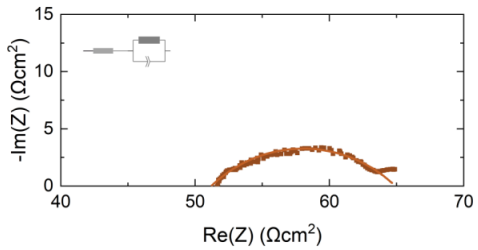

***Figure S7:** Fit of a separated anode with a R-(R)(CPE) circuit. The second contribution at low frequencies*

6.3 Publication II – Supplementary Information

Benchmarking of Coatings for Cathode Active Materials in Solid-State Batteries Using Surface Analysis and Reference Electrodes – Supplementary Information

Full list of SIMS fragments, additional PCA graphs, additional ToF-SIMS XPS and SEM images and graphs.

Jonas Hertle,[a,b] Felix Walther,[a,b] Teo Lombardo,[a,b] Christine Kern,[a,b] Boris Pavlovic,[a]

Boris Mogwitz,[a,b] Xiaohan Wu,[d] Holger Schneider,[d] Marcus Rohnke,[a,b] and Jürgen Janek [a,b,c,*]

[a]Institute of Physical Chemistry, Justus Liebig University Giessen,

Heinrich-Buff-Ring 17, D-35392 Giessen, Germany.

[b]Center for Materials Research (ZfM), Justus Liebig University Giessen,

Heinrich-Buff-Ring 16, D-35392 Giessen, Germany.

[c]Battery and Electrochemistry Laboratory, Institute of Nanotechnology,

Karlsruhe Institute of Technology (KIT), Hermann-von-Helmholtz-Platz 1,

D-76344 Eggenstein-Leopoldshafen, Germany.

[d]BASF SE, 67056 Ludwigshafen, Germany

*E-mail: juergen.janek@phys.chemie.uni-giessen.de

Table S1. List of the fragments used in the analysis of the data presented herein. The fragments were assigned with OrbiTrap SIMS. The lower and upper boundaries used for ToF-SIMS used are given as well. The description assign the fragments to polysulfide and formation of oxygenated products (POy and SOy) or the SE and CAM and more general peaks such as carbon (C) and lithium (Li).

Center Mass (u)	Lower Mass (u)	Upper Mass (u)	Assignment	Description	PC1 loading
7.017006	7.01196	7.020233	Li^-	Li	-0.00522
12.000292	11.996081	12.005384	C^-	C	0.01385
15.995245	15.991369	16.001452	O^-	CAM	-0.07016
17.003265	16.997031	17.008355	OH^-	CAM	-0.03622
23.01132	23.004475	23.016094	LiO^-	Li	-0.04682
23.999886	23.993993	24.00708	C_2^-	C	0.00884
24.019323	24.015058	24.025743	$LiOH^-$	Li	0.09804
30.972836	30.965234	30.9845	P^-	SE	-0.09362
31.971958	31.964211	31.982626	S^-	SE	-0.11543
33.966922	33.95909	33.976278	$^{34}S^-$	SE	-0.1102
34.969898	34.960632	34.980007	Cl-	SE	-0.09306
35.999476	35.992658	36.007436	C_3^-	C	0.01622
36.965723	36.956692	36.977405	$^{37}Cl^-$	SE	-0.0917
41.983943	41.976767	41.993065	$LiCl^-$	Cl	0.02018
46.964464	46.957212	46.980278	PO^-	PO_y	-0.0897
47.963639	47.957073	47.977911	SO^-	SO_y	-0.10076
47.99599	47.991647	48.009199	C_4^-	C	0.05044
51.005212	50.997121	51.013746	$LiCO_2^-$	Li	0.11959
57.93467	57.919999	57.948211	Ni^-	CAM	0.10135
59.984343	59.97883	59.991334	CO_3^-	Li	-0.03634
62.946407	62.934497	62.953584	PS^-	SE	0.00304
62.964067	62.954585	62.980482	PO_2^-	PO_y	-0.15013
63.945299	63.932029	63.953649	S_2^-	Polysulfide	-0.07618

63.961617	63.954505	63.97979	SO_2^-	SO_y	-0.11358
65.958358	65.95217	65.973512	$^{34}SO_2^-$	SO_y	-0.07619
73.929164	73.914317	73.943552	NiO^-	CAM	-0.0738
78.941445	78.930234	78.946054	POS^-	PSO_y	0.05911
78.959871	78.950848	78.982112	PO_3^-	PO_y	-0.19377
79.956608	79.946211	79.971897	SO_3^-	SO_y	-0.17177
80.96276	80.956449	80.968527	$^{18}OPO_2^-$	PO_y	-0.05891
81.952091	81.940584	81.964767	$^{34}SO_3^-$	SO_y	-0.14367
89.904888	89.889383	89.91308	NiS^-	CAM	0.02207
89.925	89.912195	89.94089	NiO_2^-	CAM	-0.13764
90.932	90.924681	90.94242	$NiHO_2^-$	CAM	-0.13201
91.922	91.909787	91.936939	$^{60}NiO^{2-}$	CAM	-0.10983
92.927631	92.916631	92.940325	$^{60}NiHO_2^-$	CAM	-0.06453
94.919576	94.906237	94.925615	PS_2^-	Polysulfide, mass interf	-0.04159
94.934213	94.926839	94.958075	PSO_2^-	SO_y	-0.15512
95.916818	95.900139	95.936316	S_3^-	Polysulfide	-0.11578
95.950623	95.937099	95.972729	SO_4^-	SO_y	-0.20307
97.912658	97.889266	97.934924	$^{34}SS_2^-$	Polysulfide	-0.12579
97.950121	97.936878	97.963408	$^{34}SO_4^-$	SO_y, mass interf	-0.1547
102.966	102.94695	102.992488	$LiSO_4^-$	SO_y	-0.10713
105.900728	105.888559	105.911614	$NiSO^-$	CAM	-0.04123
110.914745	110.892269	110.947879	PS_2O^-	PSO_y	-0.19589
112.910151	112.8838	112.935358	$^{34}SPSO^-$	PSO_y	-0.15194
121.879811	121.854128	121.903675	NiS_2^-	TMS	0.0595
126.892412	126.873525	126.913018	PS_3^-	Polysulfide	-0.15563
127.887436	127.852603	127.923293	S_4^-	Polysulfide	-0.14384

128.887042	128.855137	128.923183	$P^{34}SS_2^-$	Polysulfide	-0.14586
152.896836	152.875916	152.93076	$LiPS_2ClO^-$	Cl	-0.18745
154.894378	154.875678	154.925904	$^{37}ClLiPS_2O^-$	Cl	-0.14984
158.866099	158.817807	158.894269	PS_4^-	Polysulfide	-0.10593
159.858916	159.814648	159.889809	S_5^-	Polysulfide	-0.04219
164.922532	164.893024	164.96529	$LiP_2O_6^-$	PO_y	-0.14866
165.882717	165.860864	165.917609	$LiPS_4^-$	Polysulfide	-0.1098
180.896347	180.869149	180.942622	$LiP_2SO_5^-$	PSO_y	-0.14848
190.843943	190.776632	190.898988	PS_5^-	Polysulfide	-0.11863
191.828361	191.776626	191.865725	S_6^-	Polysulfide	-0.0587
196.874725	196.844735	196.932985	$LiP_2S_2O_4^-$	PSO_y, $LiP_2S_4^-$	-0.14106
197.853636	197.829516	197.910948	$LiPS_5^-$	Polysulfide	-0.13299
212.852781	212.815498	212.91405	$LiP_2S_3O_3^-$	PSO_y	-0.18013
212.944772	212.918215	212.997526	$Li_3S_2O_8^-$	SO_y	-0.09407
222.812183	222.7388	222.861611	PS_6^-	Polysulfide	-0.05905
223.7914	223.730438	223.842972	S_7^-	Polysulfide	-0.07333
228.831141	228.794486	228.894782	$LiP_2S_4O_2^-$	PSO_y, $LiP_2S_5^-$	-0.19742
229.820853	229.768685	229.894117	$LiPS_6^-$	Polysulfide	-0.15858
230.827283	230.776293	230.892272	$LiP_2{}^{34}SS_3O_2^-$	PSO_y	-0.14578
244.81514	244.780584	244.882555	$LiP_2S_5O^-$	PSO_y	-0.20761
246.81355	246.785185	246.875614	$LiP_2{}^{34}SS_4O^-$	PSO_y	-0.16185
255.766166	255.712182	255.813238	S_8^-	Polysulfide	-0.00723
260.795352	260.756072	260.870384	$LiP_2S_6^-$	Polysulfide	-0.17744

Table 2. Initial capacity QS_0 and capacity retention QS_{ret} scores for all samples.

Sample	QS_{ret}	QS_0		

Uncoated	0.19141	1	$SQ_0 = \frac{\frac{Q_{0.1C}}{Q_{2C}}}{\frac{Q_{0.1C,\,uncoated}}{Q_{2C,\,uncoated}}}$	$SQ_0 = \frac{Q_{ret}}{Q_{ret,\,uncoated}}$
$LiNbO_3$	0.27074	1.06007		
ZrO_2 thin	0.14806	0.84354		
ZrO_2 thick	0.15576	0.91882		
X thin	0.29402	1.12935		
X thick	0.19175	0.81235		

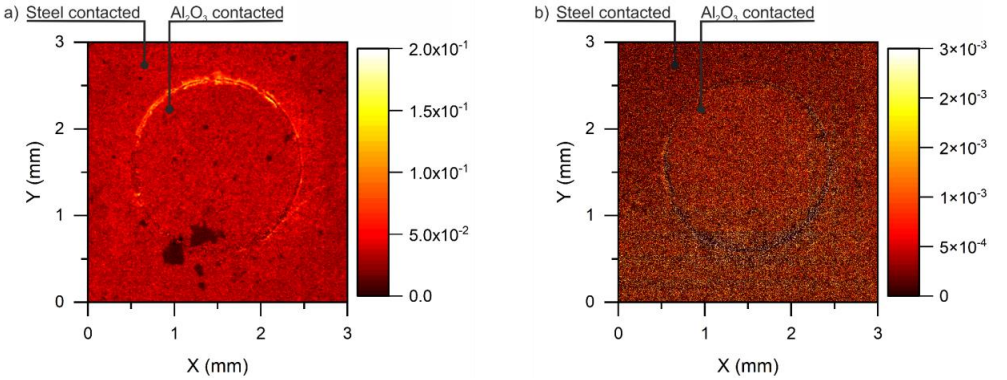

Figure S1. Large area scans of the same pellet shown in fig. 4. The SO_3^- signal shown in a) is attributed to the formation of sulphates that only form in contact to active material. The active material is distributed equally throughout the sample and so is the respective degradation product and signal in ToF-SIMS. The Li^- signal shown in b) is distributed throughout the whole sample as well indicating that the state-of-charge is distributed homogeneously as well.

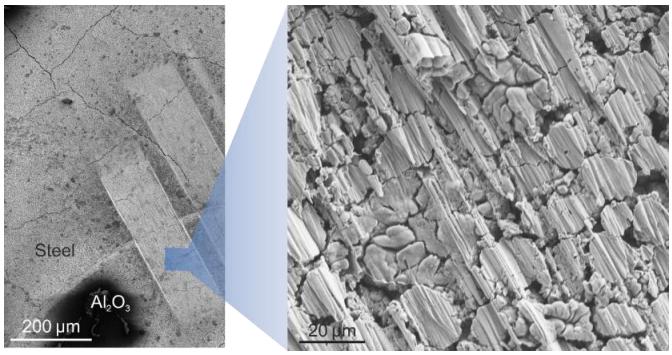

Figure S2. SEM images of a cathode composite pellet with a FIB cut in a shallow angle of 10°.

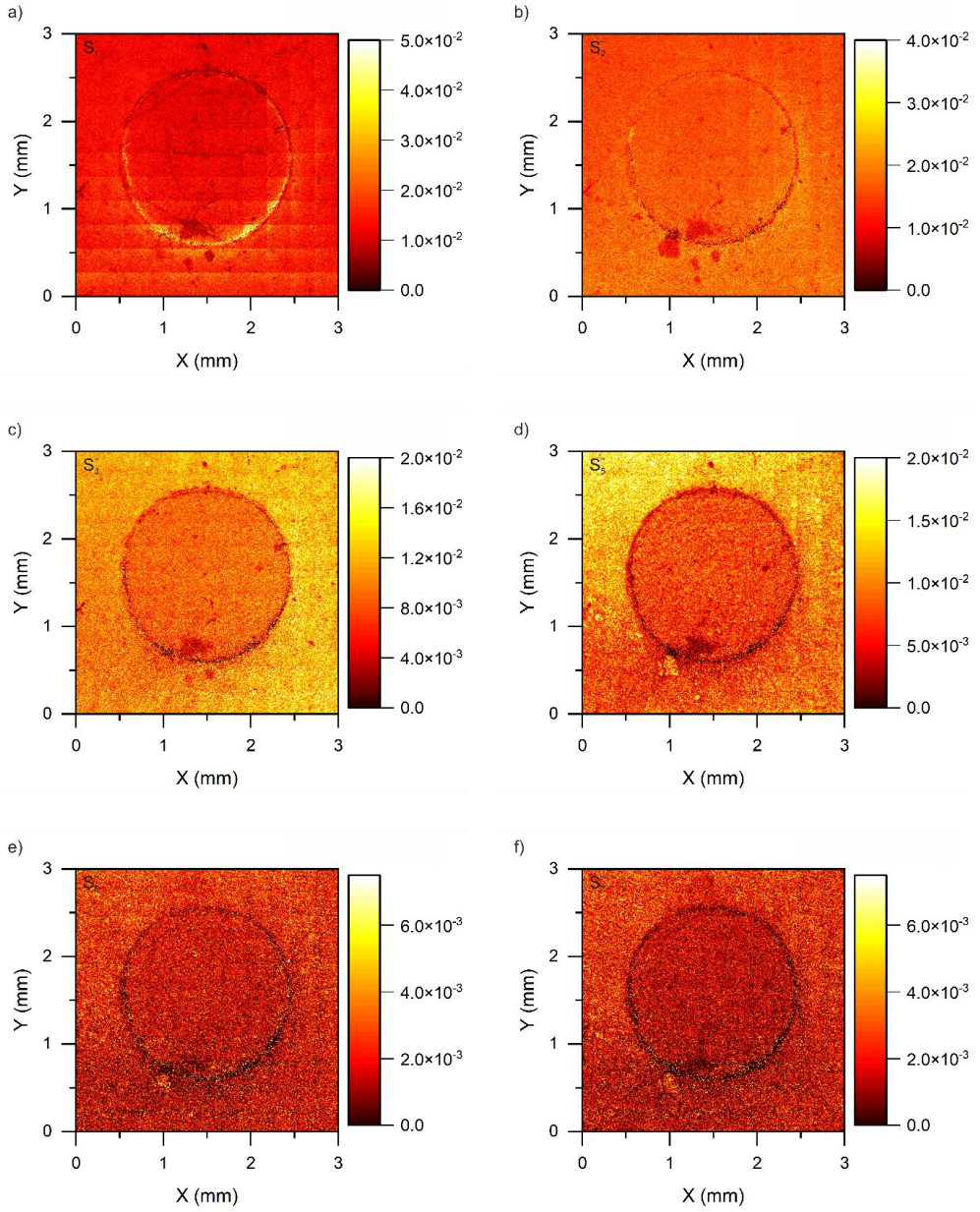

Figure S3. Comparison of S_x^- signals in the steel contacted (outside of circle) and Al_2O_3 (inside of circle) contacted area. S_1^- and S_2^- (a and b) show no significant difference. S_3^-- S_7^- (c-f) show significant differences in the differently contacted areas.

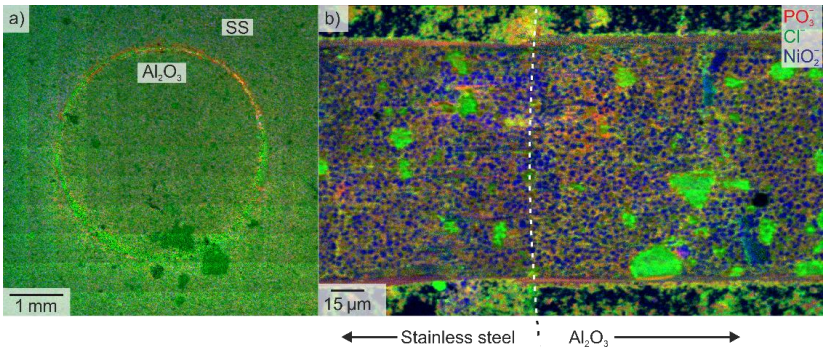

Figure S4. Large area cross-section of a cathode composite pellet as shown in Fig. 5. a) Overview of the whole Al_2O_3 contacted area and its surroundings. b) Large-area scan of the cross-section created with FIB. Here, however, PO_3^- is used as the degradation signal. The respective fragments are normalized to the total ion signal.

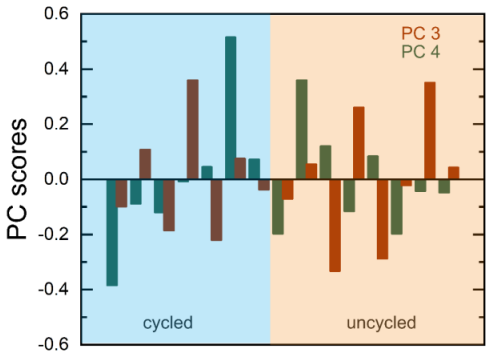

Figure S5. PC 3 and PC 4 scores for the cycled and uncycled sample. There is no correlation between cycled and uncycled samples for these principal components. See ToF-SIMS analysis results – PCA and Experimental – Principal component analysis for detailed explanation.

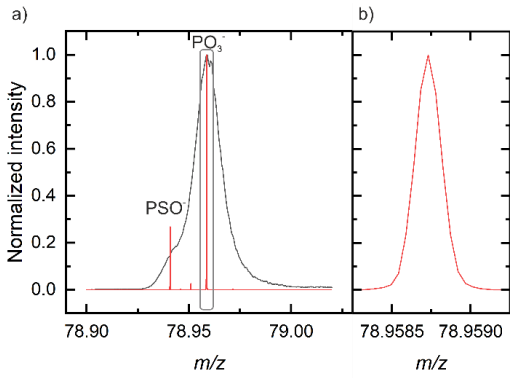

Figure S6. Comparison between ToF-SIMS (black) and OrbiTrap-SIMS (red) measurements. The mass resolution of OrbiTrap is much higher (~4.13×10^5) compared to ToF-SIMS (5.61×10^3). a) The two fragments PO_3^- and PSO^- overlap in the ToF signal whereas they are separated in the OrbiTrap measurement. b) zoomed in OrbiTrap signal for the PO_3^- fragment.

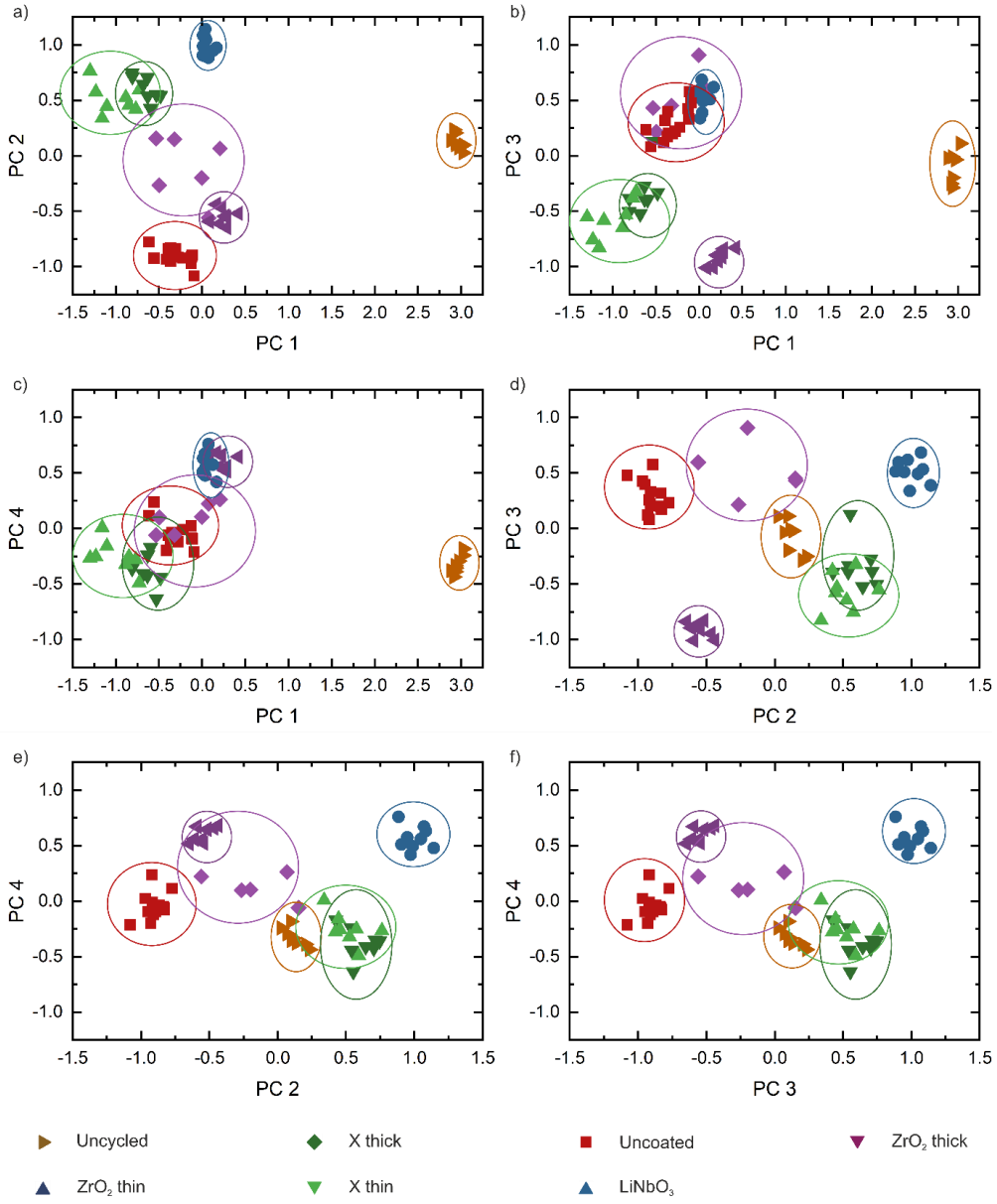

Figure S7. a-f) PC vs PC plots for other PCs than PC2 vs PC1. Clustering of the samples can still be observed, however, the effect is not as strong as with PC1 and PC2.

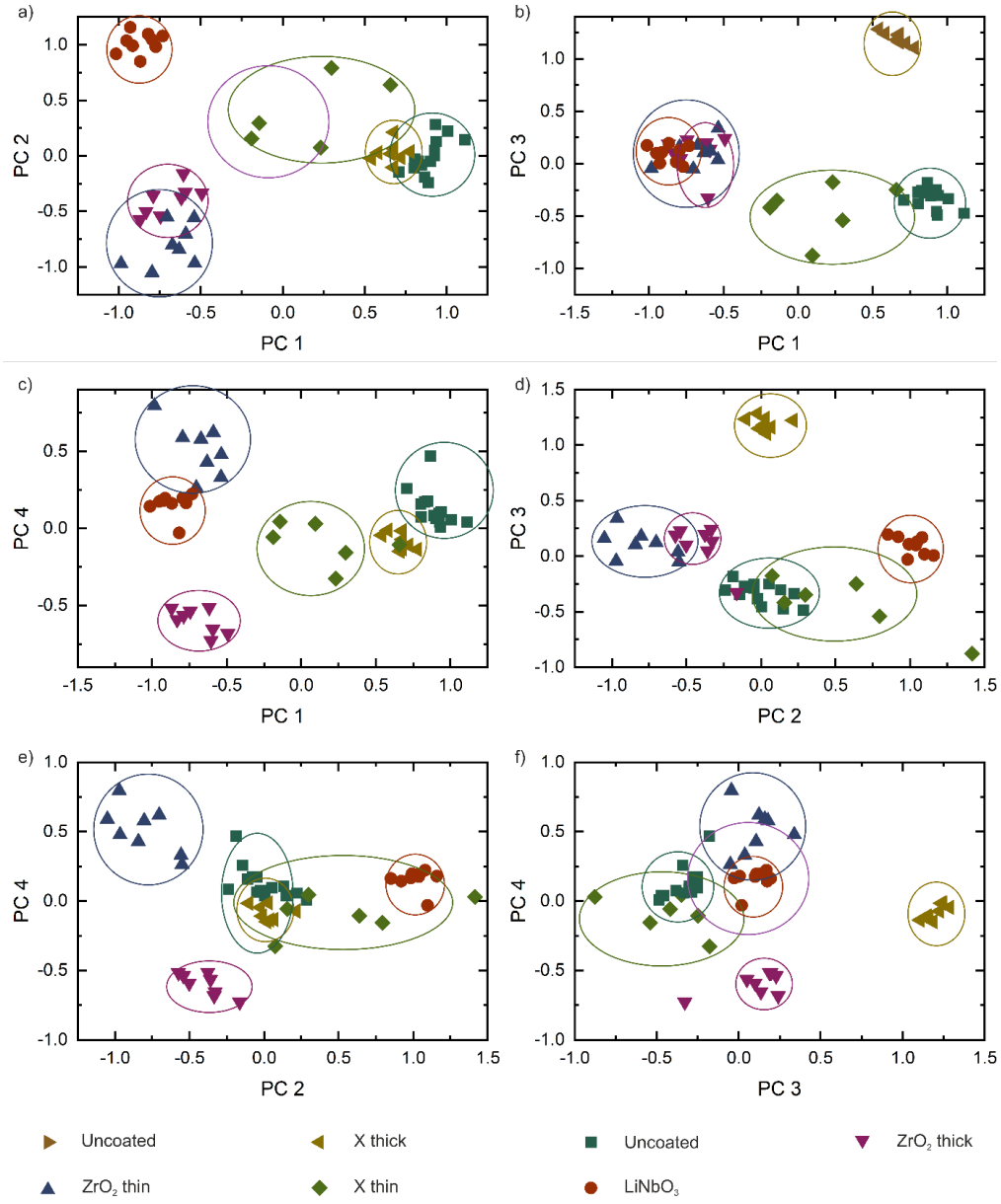

Figure S8. PCA of cycled coated and uncoated samples. The strongest separation is present between the uncycled and cycled samples in PC1 as shown in a), b) and c). The separations on the other PCs are not as strong, but clustering of the different coatings is still observed on PC2 and PC3(d-f).

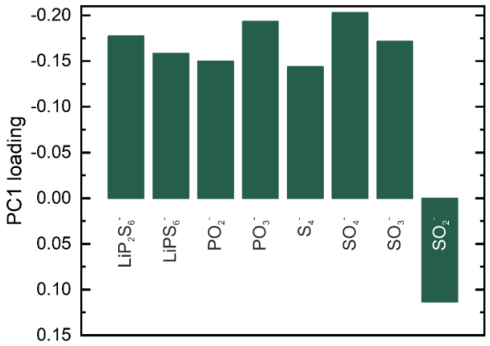

Figure S9. Loadings for the PCA performed with the uncycled and the cycled (coated and uncoated) samples. Note, that the loadings are very similar to the PCA performed with an cycled and uncycled sample only. Furthermore, note, that the y-axis is reversed.

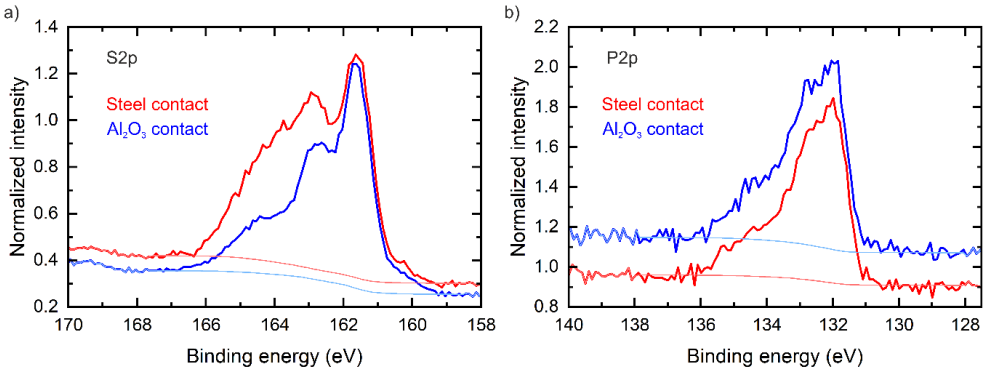

Figure S10. Analogous graph to Fig. 3 in the main part but without background correction with the S2p signal shown in a) and the P2p signal shown in b). The background that was subtracted for the main part is shown in lighter colors.

6.4 List of scientific publications

2019 *Rational design of quasi-zero-strain NCM cathode materials for minimizing volume change effects in all-solid-state batteries*
Florian Strauss, Lea de Biasi, A-Young Kim, Jonas Hertle, Simon Schweidler, Jürgen Janek, Pascal Hartmann, Torsten Brezesinski
ACS Materials Letters, 2 (1), **2019**, p. 84–88

2021 *The Working Principle of a $Li_2CO_3/LiNbO_3$ Coating on NCM for Thiophosphate-Based All-Solid-State Batteries*
Felix Walther, Florian Strauss, Xiaohan Wu, Boris Mogwitz, Jonas Hertle, Joachim Sann, Marcus Rohnke, Torsten Brezesinski, Jürgen Janek
Chemistry of Materials, 33 (6), **2021**, p. 2110–2125

2023 *Formation of an Artificial Cathode–Electrolyte Interphase to Suppress Interfacial Degradation of Ni-Rich Cathode Active Material with Sulfide Electrolytes for Solid-State Batteries*
Tong-Tong Zuo, Felix Walther, Shamail Ahmed, Raffael Rueß, Jonas Hertle, Boris Mogwitz, Kerstin Volz, Jürgen Janek
ACS Energy Letters, 8 (3), **2023**, p. 1322–1329

Miniaturization of Reference Electrodes for Solid-State Lithium-Ion Batteries
Jonas Hertle, Felix Walther, Boris Mogwitz, Steffen Schröder, Xiaohan Wu, Felix Hermann Richter, Jürgen Janek
Journal of The Electrochemical Society, 170 (4), **2023**, 040519

2024 *Benchmarking of Coatings for Cathode Active Materials in Solid-State Batteries Using Surface Analysis and Reference Electrodes*
Jonas Hertle, Felix Walther, Teo Lombardo, Christine Kern, Boris Pavlovic, Boris Mogwitz, Xiaohan Wu, Holger Schneider, Marcus Rohnke, Jürgen Janek
ACS Applied Materials & Interfaces, 16 (7), **2024**, p. 9400–9413

6.5 List of conference contributions

2019	"BASF International Scientific Network for Electrochemistry and Batteries – Meetings" in Bad Dürkheim, Germany – oral presentation
	"BASF International Scientific Network for Electrochemistry and Batteries – Meetings" in Bad Dürkheim, Germany – poster presentation
2020	"International Battery Association Conference" online – poster presentation
2022	"International Meeting for Lithium Batteries" in Sydney, Australia – poster presentation
2023	"International Bunsen Discussion Meeting: Solid-state Batteries V – From Fundamentals to Application (SSB V)" in Frankfurt am Main, Germany – poster presentation

7 Thank you!

Researching on my topic and working at our institute has been an incredible experience! I truly enjoyed the environment provided to me and I am very grateful for the amazing friends I made along the way.

First and foremost, I would like to express my sincere gratitude to my supervisor, Dr. Dr. h. c. Jürgen Janek. You created a top-tier environment for research and learning. Your expertise and patience have been greatly appreciated.

I would also like to thank Prof. Dr. Anja Henns for being my second reviewer, furthermore I would like to thank Prof. Dr. Bernd Smarsly and Prof. Dr. Maren Lepple for joining the examination committee of my doctoral defense.

I sincerely thank BASF SE for the financial support that made this research possible. This funding allowed me to pursue my research and enabled me gaining experience abroad. I am especially thankful for the support by Dr. Xiaohan Wu and Dr. Holger Schneider for their continuous discussions, questions and expertise in the field. I would also like to thank Dr. Yuichi Aihara for hosting me during my research in Osaka at Samsung SDI – it was an amazing experience!

I'd also like to thank my colleagues and fellow PhD students, especially Felix Walther, Maximilian Kissel, for their encouragement and helpful discussions throughout this process. Your support made this journey more enjoyable and productive.

A very special thanks goes out to Laura, Philip and Jules, you really made my time in Gießen amazing. Without you, it would not have been the same for me. I already miss hanging out with you and I hope we will continue to spend a lot of time together.

I really enjoyed my team with my colleagues, both profesionally as well as non-profesionally in the kitchen, at the bouldering gym and much more. So, thank you, among others to my colleagues and friends Christoph Alt, David Schäfer and Till Fuchs.

Lastly, I want to thank family, especially my mum and dad. Without you I wouldn't be where I am today. You've been there throughout my whole life and I can't thank you enough for your unconditional support. I'm so grateful for your love and encouragement!

Danke!